

Neutron and X-ray Diffraction Studies of Magnetic Order in U-based Heavy Fermion Superconductors

By

Jean-Guy Lussier, M.Sc.

A Thesis Submitted to the School of Graduate Studies
in Partial Fulfillment of the Requirements
for the Degree of
Doctor of Philosophy

McMaster University
Hamilton, Ontario, Canada

© Copyright by Jean-Guy Lussier, 1995

MAGNETIC ORDER IN U-BASED HEAVY FERMION SUPERCONDUCTORS

DOCTOR OF PHILOSOPHY (1995)
(Physics)

McMASTER UNIVERSITY
Hamilton, Ontario

TITLE: Neutron and X-ray Diffraction Studies of Magnetic Order in
U-based Heavy Fermion Superconductors

AUTHOR: Jean-Guy Lussier, B. Sc. (Université de Montréal)
M.Sc. (Université de Montréal)

SUPERVISOR: Professor B.D. Gaulin

NUMBER OF PAGES: x, 119

Abstract

UPt₃, URu₂Si₂, UNi₂Al₃ and UPd₂Al₃ form a special group among the uranium alloys because they exhibit heavy fermion character, magnetic order and superconductivity. This main interest in the study of this group of compounds resides in the simultaneous occurrence of magnetism and superconductivity at low temperature. Such a state could potentially involve an unconventional superconducting pairing mechanism, different from that contained in standard BCS theory.

In this thesis, the magnetic states of three of these materials (URu₂Si₂, UNi₂Al₃ and UPd₂Al₃) is investigated with neutron and the relatively new resonant magnetic X-ray scattering techniques. The work presented here on URu₂Si₂ follows an earlier effort that demonstrated the applicability of the resonant X-ray technique to this weak magnetic system. Access to reciprocal space was extended in order to confirm the multipolar form of the resonant X-ray cross-section and to explore the limits of the technique compared to neutron scattering. The situation with the newly discovered UNi₂Al₃ and UPd₂Al₃ was different since their magnetic structure and phases needed first to be established. This task was achieved using two magnetic probes (neutron and X-ray scattering). Several magnetic order parameters in the normal and in the superconducting phase were also measured. The incommensurate magnetic order found in UNi₂Al₃ by neutron scattering constitutes the first observation of long range order in this compound. Other measurements on this compound provided some clues about the evolution of the magnetic structure in high magnetic fields.

Acknowledgements

I would like to start by sincerely thank Dr. B.D. Gaulin for his supervision during my presence at McMaster. I enjoyed his the positive way to deal with people and his effort to pursue high profile research.

At Chalk River, I appreciated the patience, the generosity, and the "methodical working habits" of Dr. Z. Tun. His advice was of great help in the first stage of my study. I also benefited from many useful comments and the endless curiosity of Dr. W.J.L. Buyers. Special thanks to L. McEwan, R. Donnaberger, P. Moss, M. Gauthier and S. Rowlings for their technical assistance during my several visits at the laboratory.

At Brookhaven, my sincere thanks to Dr. E. Isaacs and Dr. Paul Zschack for teaching me essential concepts in X-ray scattering, synchrotron radiation, dilution refrigerators and for helpful comments during the writing of this thesis.

I thank also Dr. C. Vettier for having kindly commented on the manuscript.

At McMaster, I thank Dr. M.F. Collins and Dr. A. P. Hitchcock for their advice and useful discussions. Also, many thanks to J.D. Garrett for his help during the night we spent growing the "Nickel sample". I thank also Dr. R. B. Rogge for his help with early versions of the manuscript.

Last but not least I thank my precious collaborator Dr. Almut Schröder for her help during most of these experiments and especially the one involving the birth of our *very cute* son Laurent! Many thanks to C. Brunelle for his help with the MacIntosh!

*À mes parents
Guy et Denise*

Table of contents

Abstract	iii
Acknowledgements	iv
Table of contents	v
List of figures and tables	vii
Introduction	1
Chapter 1 Cross-Sections for Neutron and X-ray Diffraction	5
1.1) Master Formula for Particle Scattering	8
1.2) The Neutron Cross-Section	9
1.2.1) Nuclear Scattering	9
1.2.2) Magnetic Scattering	10
1.3) Elements of X-ray Scattering	12
1.4) Magnetic X-ray Scattering	18
1.4.1) Non-Resonant Magnetic X-ray Scattering	20
1.4.2) Resonant Magnetic X-ray Scattering	21
Chapter 2 Scattering Experiments at Neutron- and Light-Sources	28
2.1) The Spectrometer at a Neutron Facility	31
2.2) The Spectrometer at a Light Source	32
2.2.1) Bragg Scattering with Absorption	36
2.2.2) Fluorescence and Absorption Corrections	42
Chapter 3 Magnetic Structures and Phases of Uranium-based Heavy Fermion Superconductors	47
3.1) Resonant X-ray Cross-Section in URu_2Si_2	50
3.1.1) Experimental Setup and Results	51
3.1.2) Calculated Intensities	56
A) Magnetic Reflections	57
B) Charge Reflections	59
3.1.3) Ordered Moment Size	64

3.2) Magnetic Structure and Phases of UPd_2Al_3 and UNi_2Al_3	66
3.2.1) UPd_2Al_3	67
A) Spin Orientation in the Basal Plane	67
B) Magnetic Phases and Order Parameter.....	75
3.2.2) UNi_2Al_3	79
A) Magnetic Order in Zero Field	79
B) Magnetic Order in High Magnetic Field	88
3.3) Magnetic Order and Superconductivity in UPd_2Al_3 and UNi_2Al_3	97
3.3.1) UPd_2Al_3	97
3.3.2) UNi_2Al_3	99
3.3) Uranium Valence State in UNi_2Al_3	103
Conclusion	108
Appendix A: The physics at resonance	
A.1) The Quasi-elastic Fast Collision Approximation.....	111
A.2) The Templeton Effect	112
Bibliography	114
Published work	119

List of figures and tables

Figures

Chapter 1

Figure 1-1: Scattering event in real and in reciprocal space

Figure 1-2: Real and imaginary part of the anomalous dispersion corrections in the vicinity of a resonance for K-edges

Figure 1-3: The white-line in an absorption spectrum

Figure 1-4: Real and imaginary part of anomalous corrections of a white-line

Figure 1-5: First observation of magnetic scattering in NiO using X-rays

Figure 1-6: Resonant magnetic X-ray scattering at the L_{III}-edge of Ho

Figure 1-7: Classical mechanism of X-ray scattering from an unbound electron

Figure 1-8: Schematic view of a core-hole excitation at a resonance in Ho

Figure 1-9: Schematic difference between charge and magnetic resonance profiles for a simple antiferromagnet

Chapter 2

Figure 2-1: Triple-axis spectrometer

Figure 2-2: Typical photon flux vs. energy for a x-ray tube and at the NSLS X-17 beamport

Figure 2-3: Radiation emission pattern of electrons in circular motions

Figure 2-4: The X-ray and UV synchrotrons at NSLS

Figure 2-5: The optics of the Oak Ridge X-14 spectrometer at NSLS

Figure 2-6: Asymmetric reflection

Figure 2-7: Bragg intensity vs. η for different absorptions

Figure 2-8: Reduction of the higher-order by detuning the monochromator

Figure 2-9: Auger and fluorescence emission after the creation of a core-hole

Figure 2-10: Fluorescence from a thick slab

Figure 2-11: Resonance profiles at (001) charge reflection of UPd_2Al_3

Chapter 3

Figure 3-1: Magnetic structure and magnetic order parameter in UPt_3

Figure 3-2: Magnetic structure, finite correlation length and magnetic order parameter in URu_2Si_2

Figure 3-3: Scattering geometry of the X-ray experiments on URu_2Si_2 at X-22c

Figure 3-4: Magnetic and charge reflections in URu_2Si_2

Figure 3-5: Extinction effect

Figure 3-6: Crystal structure of UT_2Al_3 (T=Ni, Pd) materials

Figure 3-7: Magnetic order in the basal-plane of UPd_2Al_3 with the spins along the a-axis

Figure 3-8: Ψ -rotation in a four-circle spectrometer

Figure 3-9: Definition of the angles α and β describing the spin orientation (\hat{s}) during the Ψ -rotation

Figure 3-10: Asymmetric absorption correction vs. Ψ for (0 h l)-reflections

Figure 3-11: Ψ -rock at (002) charge reflection in UPd_2Al_3

Figure 3-12: Ψ -rock at (003/2) magnetic reflection in UPd_2Al_3

Figure 3-13: Ψ -rock at (0 1 3/2) magnetic reflection in UPd_2Al_3

Figure 3-14: Spin orientation in the hexagonal basal plane of UPd_2Al_3

Figure 3-15: Magnetic order parameters in UPd_2Al_3

Figure 3-16: 12K-anomaly found by neutron scattering in 0 Tesla in UPd_2Al_3

- Figure 3-17: Magnetization and phase diagram of UPd_2Al_3
- Figure 3-18: Powder pattern of UNi_2Al_3 obtained by neutron scattering
- Figure 3-19: Observed nuclear Bragg peak intensities from the UNi_2Al_3 single crystal
- Figure 3-20: Observation of magnetic order in UNi_2Al_3
- Figure 3-21: Zero field intensity pattern in the (h0l)-plane in UNi_2Al_3
- Figure 3-22: Two possible spin structures in the hexagonal basal plane of UNi_2Al_3
- Figure 3-23: Part of a long h-scan between (001) and (101) in UNi_2Al_3
- Figure 3-24: a^* -scan for different magnetic fields in UNi_2Al_3
- Figure 3-25: Magnetic field dependence of a magnetic satellite of UNi_2Al_3
- Figure 3-26: Magnetic phase diagram of UNi_2Al_3 polycrystal
- Figure 3-27: Nuclear peak intensity of UNi_2Al_3 in an external magnetic field
- Figure 3-28: High field (8 Tesla) intensity pattern in the (h0l)-plane in UNi_2Al_3
- Figure 3-29: Order parameters in a field of UNi_2Al_3
- Figure 3-30: Incommensurate wave-vector position for a series of magnetic fields in UNi_2Al_3
- Figure 3-31: Magnetic order parameter near the superconducting transition in UPd_2Al_3
- Figure 3-32: Magnetic order parameter at the superconducting phase transition in UPd_2Al_3 (neutron scattering)
- Figure 3-33: Mounting procedure of the UNi_2Al_3 sample for the dilution fridge experiment
- Figure 3-34: Magnetic order parameter of UNi_2Al_3 in the superconducting region
- Figure 3-35: Scans along a^* -direction vs. temperature in UNi_2Al_3
- Figure 3-36: Uncorrected resonance profiles in UNi_2Al_3
- Figure 3-37: Energy dependence of the Be and Kapton absorption coefficients
- Figure 3-38: Fluorescence curves in UNi_2Al_3
- Figure 3-39: Corrected resonance profiles in UNi_2Al_3

Tables

Chapter 2

Table 2-1: Absorption coefficients obtained from fluorescence curves for the U-based HFS

Chapter 3

Table 3-1: Integrated intensities and FWHM of charge peaks in URu_2Si_2

Table 3-2: Integrated intensity and FWHM of magnetic peaks in URu_2Si_2

Table 3-3: Charge intensities corrected for Al attenuation

Table 3-4: Calculated magnetic intensities of URu_2Si_2 at the M_{IV} -edge

Table 3-5: Evaluation of $\Delta f'_U$ at the M_{IV} -edge from the total absorption curve

Table 3-6: Anomalous dispersion corrections Δf and $\Delta f'$ for U, Ru, and Si at the M_{IV} -edge

Table 3-7: Calculated charge intensities of URu_2Si_2 using $\Delta f'_U$ from the fluorescence measurement

Table 3-8: Calculated charge intensities of URu_2Si_2 when $\Delta f'_U$ is left as a fitting parameter

Table 3-9: Some of the accessible magnetic reflections of UNi_2Al_3 for the X-ray experiment in the superconducting phase

Introduction

Discovered nearly 20 years ago, heavy fermion (HF) materials have low temperature properties which place them in a class of their own. The properties of ordinary metals can usually be well understood by considering non-interacting or weakly-interacting conduction electrons. In HF materials, this picture is not adequate because large electron-electron correlations develop at low temperature [Fisk (1986)]. The observation of magnetic order and even superconductivity in these "strongly correlated metals" stimulated a strong interest in the study of this unusual state.

The mechanism leading to the creation of the HF state is rather complex, but some basic concepts can help identify its roots. In general, HF alloys are obtained by mixing an *f*-electron atom (Ce, Yb, or U) with a metal [Grewe *et al.* (1991)]. In actinides (of which U-alloys are members), the soft bonding of the *f*-electron, caused by relativistic effects in the inner electronic shells, leads to valence configurations nearly degenerate in energy and to wave functions with greater spatial extent than those in the non-relativistic case [Lam *et al.* (1974), Chan *et al.* (1974) and Desclaux *et al.* (1984)]. These effects are important in the creation of the HF state since the incorporation of this in a metal amplifies the delocalization of the *f*-electron wave function and eventually leads to hybridization with the conduction bands. This contrasts with rare earth metals where the valence *f*-electron wave function is *localized* or with transition metals where the *d*-electron wave function extends approximately over the whole crystal and is *itinerant*. In HF materials, the *f*-electron wave function falls in the wide region between these 2 extremes.

There are three criteria to help identify the creation of the HF state [Fulde *et al.* (1988)]: (i) a large linear term (γ) in the specific heat when compared to ordinary metals, (ii) a large Pauli-like spin susceptibility, and (iii) a Sommerfeld-Wilson ratio (χ/γ) ≈ 1 . These three conditions reflect a large increase of the density of states at the Fermi level associated with the correlations. HF get their name from Fermi liquid theory where the renormalized mass of the quasiparticles is proportional to the density of states at the Fermi level: $m^* \approx \gamma = g(E_F)$.

The mixed behavior of the f -electron wave function (localized vs. itinerant) and the presence of fluctuations at the Fermi level lead to peculiar magnetic properties. At high temperatures HF materials have a large Curie-Weiss susceptibility which suggests that the paramagnetic moments are localized and of conventional size. At low temperatures the saturated moment in the ordered phase is often much lower in value than the paramagnetic one (typically an order of magnitude). This screening of the magnetic moment, due to the interactions with the conduction band, has some similarities with the Kondo effect. In the HF case, however, the magnetic impurities are not dilute, like in a normal Kondo system, but form a lattice leading to coherence effects at low temperature [Fulde *et al.* (1988)].

Among all the HF materials known to date, UPt₃, URu₂Si₂, UPd₂Al₃, UNi₂Al₃ together with UBe₁₃ and CeCu₂Si₂ constitute the 6 known heavy fermion superconductors (HFS) [Loewenhaupt *et al.* (1993), Grewe *et al.* (1991)]. Besides superconductivity, all of them develop magnetism at a temperature above the superconducting state, a phenomenon which usually interferes with superconductivity [Steglich *et al.* (1979)]. As the ordering in UBe₁₃ is controversial [Kleiman *et al.* (1990)], the present thesis is mostly related to

the magnetic state of the first 4 compounds of this series known as the *uranium-based HFS*.

The magnetic state of the HFS is of particular interest because it can help address fundamental questions related to the formation of superconductivity. The fluctuations at the Fermi level associated with the HF character may produce a Cooper pairing mechanism different from the standard electron-phonon interaction (BCS-type) [Hayden *et al.* (1992)] The *decrease* of the magnetic order parameter as it enters the superconducting phase [Aeppli *et al.* (1989)] and the presence of two superconducting transitions which merge when the magnetic moment vanishes upon external pressure both suggest the creation of an unconventional superconducting state in UPt₃ [Hayden *et al.* (1992)]. In contrast, both the antiferromagnetic ($T_N=17.5\text{K}$) and the superconducting ($T_c=1.2\text{K}$) phases seem to coexist apparently unaffected by each other down to the lowest temperature in URu₂Si₂ [Mason *et al.* (1990)], and this is also interesting.

The magnetic state of both UPt₃ and URu₂Si₂ has been intensively studied over the last few years [Aeppli *et al.* (1994)]. However, the weakness of the ordered moment found in these materials ($\approx 10^{-2} \mu_B$) is an important experimental limitation for a detailed investigation of the coexisting phases between superconductivity and magnetism. The interest in the U-based HFS increased recently with the discovery of the two new isostructural UT₂Al₃ (T=Pd, Ni) HFS compounds¹ with magnetic moments an order of magnitude larger. The existence of magnetic moments of *conventional size* within the superconducting phase constitutes a remarkable property associated with the new HFS.

¹It is interesting to note that nickel, palladium, and platinum all belong to the same family in the periodic table.

In this thesis, we are motivated to study of the magnetic order of the U-based HFS using diffraction techniques. First, we applied a recently developed X-ray diffraction technique to detect magnetism. Direct photon-electron scattering leads to very small magnetic cross-sections, but when the incident X-ray energy is tuned to match an absorption edge of the magnetic atom, enhancements of many orders of magnitude are possible. This technique, called *Resonant Magnetic X-ray scattering*, constitutes a new, interesting probe for magnetic systems. We performed a detailed analysis of charge and magnetic Bragg peak intensities of URu_2Si_2 to demonstrate the properties of the *Resonant Magnetic X-ray* cross-section and to show whether or not quantitative information (like the moment size) can be obtained.

Second, we used both *Resonant Magnetic X-ray scattering* and standard neutron diffraction techniques to study the magnetic order and the magnetic phases of the new UT_2Al_3 ($\text{T}=\text{Pd}, \text{Ni}$) HFS compounds. In order to make some comparisons with UPt_3 and URu_2Si_2 , magnetic order parameters were measured in the normal and in the superconducting phase. The results presented here on UNi_2Al_3 constitute the first observation of long range order in this compound and the first incommensurate ordering among the HFS.

This thesis is divided in three chapters. Chapter 1 describes the general physics associated with the scattering cross-sections for both neutrons and X-rays. Emphasis is put on the mechanism leading to magnetic scattering for each probe. Chapter 2 gives a more detailed account of the experimental conditions associated with experiments performed at nuclear reactors and at synchrotron radiation facilities. Finally, the experimental results related to the magnetic state of the uranium-based HFS are presented in Chapter 3.

Chapter 1

Cross-Sections for Neutron and X-ray Diffraction

Since the early days of Brockhouse and Shull², neutron scattering has been acknowledged as an important tool in the study of condensed matter. It can be used to find the atomic spacings in a crystal lattice and to study the lattice vibrations (phonons). Also, because the neutron has a magnetic moment, neutron scattering can be used to study magnetic structures (arrangements of the moments in a material) and magnetic excitations (spin waves, magnetic fluctuations).

X-ray scattering is also known as a very important technique in crystal structure characterization. Until recently, X-rays were not appreciated as a magnetic probe³. During the last 10 years, however, as large scale synchrotron sources became available, it was found that X-ray diffraction could be used as a new tool to study magnetism in condensed matter. In the following, we will describe the different physical processes leading to magnetic neutron and X-ray diffraction.

Neutrons and X-rays are diffracted from matter because of their wave-like character. Following basic concepts in quantum mechanics, the wavelength (λ) of the radiation is related to its momentum (p) by: $\vec{p} = \hbar \vec{k}$, where $|\vec{k}| = 2\pi/\lambda$ is the associated wave-vector.

²1994 Nobel Prize Laureates

³ except for magneto-optic effects [Vettier (1993)].

In the scattering event shown in Fig. 1-1 a), the incident radiation, identified by its wave-vector \vec{k}_i , scatters off the sample after some of its momentum, $\vec{Q} = \vec{k}_i - \vec{k}_f$, has been transferred to the sample. The momentum transfer \vec{Q} , the incident wave-vector \vec{k}_i , and the scattered wave-vector \vec{k}_f define the scattering plane of the event.

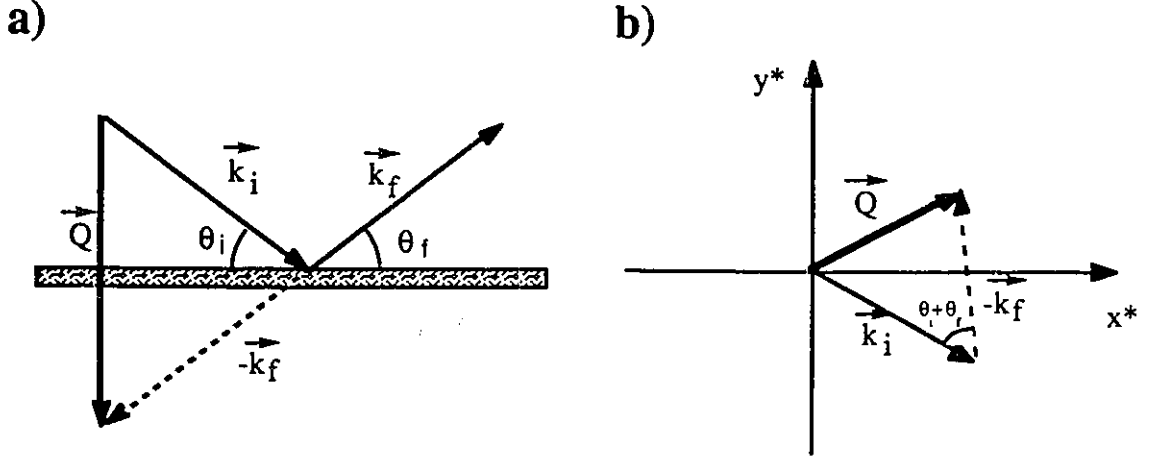


Figure 1-1: Scattering event in (a) real and in (b) reciprocal space.

In addition to momentum, energy can also be transferred in the event. The energy transfer, $\Delta\omega = E_i - E_f$, can be either positive or negative depending on the capacity of the sample to give or take energy from the scattering probe. The scattering is said to be elastic when the scattered particle has the same energy as the incident one ($\Delta\omega=0$) and inelastic otherwise ($\Delta\omega \neq 0$). The conservation of energy for neutrons and X-rays are:

$$\text{neutron: } \Delta\omega = E_i - E_f = \frac{\hbar^2}{2m} (k_i^2 - k_f^2) \quad (1.1)$$

$$\text{X-ray: } \Delta\omega = E_i - E_f = \hbar c (k_i - k_f)$$

For elastic events ($\Delta\omega=0$), when the momentum transfer \vec{Q} matches the repeat distance d of the periodic structure $|\vec{Q}| = \frac{2\pi}{d} = \sqrt{(hx^*)^2 + (ly^*)^2}$ [see Fig. 1-1 b)], coherence effects

give rise to a high intensity count rate known as the Bragg peak. Bragg scattering occurs at well defined angles when the condition, $\lambda = 2d \sin(\theta)$, is satisfied [see Fig. 1-1 a), for elastic scattering $\theta = \theta_i = \theta_f$]. In general, Bragg intensities from a particular lattice are obtained by⁴:

$$I = C L(2\theta) f_D |S(Q)|^2 \quad (1.2)$$

where C is an arbitrary constant and $L(2\theta)$ is the Lorentz factor which for linear scans in reciprocal space can be written as $L(2\theta) = \frac{1}{2 \sin \theta |\sin(\theta - \alpha)|}$ where α is the angle between the wave vector \vec{Q} and the scan direction [Lebech *et al.* (1975)]. Although not essential at low temperatures, we added for completeness the Debye-Waller factor $f_D = e^{-2W(Q)}$ which accounts for thermal effects [Price *et al.* (1986)]. $S(Q)$ is the structure factor defined as:

$$S(Q) = \sum_i^{\text{unit cell}} A_i e^{iQ \cdot R_i} \quad (1.3)$$

The sum over the unit cell accounts for the whole crystalline lattice. The factors A_i and R_i are the scattering amplitude and position of the atom "i" in the unit cell. The expression for $S(Q)$ [Eq. (1.3)] shows that diffraction intensities are related to the Fourier transform of the crystal in the direction defined by the scattering vector \vec{Q} .

⁴Other factors are needed to account for absorption in the intensity formula. These factors will be introduced later when needed.

1.1) Master formula for particle scattering

The scattering amplitudes, defined as A_i in Eq. (1.3), depend on the scattering potential, \hat{V} , existing between the scattering probe and the atomic targets in the sample. The intensity collected in a solid angle $d\Omega$ (at the detector) is proportional to the transition probability $W_{i \rightarrow f}$ between the initial state i and the final state f of the scatterer by⁵:

$$\frac{d^2\sigma}{d\Omega dE} = \frac{W_{i \rightarrow f}}{I_0} \rho(E_f) \delta(\Delta\omega + E_i - E_f) \quad (1.4)$$

where to 2nd order, the transition probability (known as Fermi's Golden rule) is:

$$W_{i \rightarrow f} = \frac{2\pi}{\hbar} \left| \langle \psi_f | \hat{V}(q) | \psi_i \rangle + \sum_n \frac{\langle \psi_f | \hat{V}(q) | \psi_n \rangle \langle \psi_n | \hat{V}(q) | \psi_i \rangle}{E_i - E_n} \right|^2$$

where

$\rho(E_f)$ is the final density of states of the scatterer,

ψ_m is the wave function of the scatterer in the initial and in the final state,

$\hat{V}(q)$ is the Fourier transform of scattering potential and I_0 the incident flux.

The expansion of Fermi's Golden Rule to second order is necessary for magnetic X-ray scattering, while neutron scattering requires a first order expansion only. The δ -function in Eq. (1.4) is added to account for energy conservation in the process; in this thesis we are only dealing with elastic events and $\Delta\omega=0$. In the next sections of this chapter, we will describe the scattering potentials, \hat{V} , responsible for neutron and X-ray scattering.

⁵Lovesey (1987) Chap. 1

1.2) The Neutron cross-section

1.2.1) Nuclear scattering

Neutrons interact with the atomic nuclei in matter through the action of strong or nuclear forces. These interactions take place over a much smaller volume than typical condensed matter length scales and the atoms can be approximated by point-like entities. The interacting potential which describes this interaction is known as the Fermi pseudo-potential, where the lattice is approximated by a series of Dirac-delta functions at the nuclear sites:

$$\hat{V}(\mathbf{r}) = \frac{2\pi\hbar^2}{m} b \delta(\mathbf{r} - \mathbf{R}) \quad (1.5)$$

The scattering length, b , has typical units in the range of the Fermi (fm). In practice, the scattering length can be very different from one nucleus to the next and since common alloys are prepared with "natural" elements, the random distribution of isotopes in the lattice leads to the following cross-sections [Price *et al.* (1986)]:

$$\begin{aligned} \text{the coherent cross-section is proportional to } |\bar{b}|^2 \\ \text{the incoherent cross-section is proportional to } |\bar{b^2}| - |\bar{b}|^2 \end{aligned} \quad (1.6)$$

The coherent cross-section, which gives the intensity of the nuclear Bragg peaks, is proportional to the average of the scattering length at each lattice site of the unit cell. The incoherent cross-section, proportional to the *variance* of the scattering lengths at the lattice sites of the unit cell, is *diffuse* and contributes to the

background level of an experiment. Besides isotopic incoherence, nuclear magnetism can also contribute to incoherent scattering because some nuclei offer different scattering amplitudes depending on the relative spin orientation between the incident neutron and the nuclei spin (in absence of nuclear ordering, nuclear spins are random and the scattering due to them is diffuse) [Collins (1989)].

As will be discussed in chapter 3, incoherent scattering is important with the nickel compound, UNi_2Al_3 , since ^{58}Ni (68%) and ^{60}Ni (26%) have very different scattering lengths and also ^{61}Ni (1%) has a large nuclear spin incoherence [Sears (1986)]. These facts explain the large background level observed in neutron powder experiments with this element.

1.2.2) Magnetic scattering

Magnetic neutron scattering occurs when the neutron magnetic moment interacts with the unpaired electrons of an atom via a dipole-dipole interaction. This interaction is described by the general result from EM theory [Price *et al.* (1986)]:

$$\hat{V}(\mathbf{R}) = -\gamma\mu_N\hat{\sigma} \cdot \vec{H} = -\gamma\mu_N\hat{\sigma} \cdot \left[\nabla \times \left\{ \frac{\mu_e \times \mathbf{R}}{|\mathbf{R}|^3} \right\} + \frac{(-e)\hbar}{c} \frac{\mathbf{v}_e \times \mathbf{R}}{|\mathbf{R}|^3} \right] \quad (1.7)$$

The scattering amplitude from Eq. (1.7) is proportional to: $(\gamma r_0) = (\gamma e^2/m_e c^2) = 5.4 \text{ fm}$, with r_0 the classical electron size and γ the neutron gyromagnetic ratio⁶. Scatterings from magnetic and nuclear origin [Eq. (1.5)] appear therefore with the same order of

⁶ Lovesey (1987) Chap.7

magnitude. It can be shown that the elastic magnetic cross-section for magnetic scattering is proportional to:

$$\frac{d^2\sigma}{d\Omega dE} \approx (\gamma r_0)^2 |\hat{\mathbf{Q}}_{\perp}^{\dagger} \cdot \hat{\mathbf{Q}}_{\perp}| f^2(Q) \delta(E_i - E_f) \quad (1.8)$$

with the perpendicular component of the moment to \mathbf{Q} being:

$$\hat{\mathbf{Q}}_{\perp} = \sum_i e^{i\mathbf{K} \cdot \mathbf{r}_i} \left\{ \tilde{\mathbf{Q}} \times (\hat{\mathbf{s}}_i \times \tilde{\mathbf{Q}}) - \frac{i}{\hbar |\tilde{\mathbf{Q}}|} \tilde{\mathbf{Q}} \times \hat{\mathbf{p}}_i \right\}.$$

The role of this perpendicular component indicates that magnetic neutron scattering is maximum when the scattering wave-vector $\tilde{\mathbf{Q}}$ is *perpendicular* to the magnetic moment direction. The magnetic neutron form factor, $f(Q)$ in Eq. (1.8), physically describes the spatial extent of the atomic orbitals giving rise to the magnetic moment. In uranium, the form factor of the 5f-orbital can be expanded:

$$f(Q) = \langle j_0(Q) \rangle + C_2 \langle j_2(Q) \rangle + \dots \quad (1.9)$$

with

$$\langle j_m(Q) \rangle = \int_0^{\infty} U_{5f}^2(r) j_m(Qr) dr$$

where $j_m(Qr)$ is the spherical Bessel function and $U_{5f}(r)$ is the uranium 5f electron density [Lander *et al.* (1991)]. Free ion calculations can be found in Freeman *et al.* (1976), but to a good approximation: $f(Q) = e^{-(Q/Q_0)^2}$ with Q_0 a constant $\approx 5.2 \text{ \AA}^{-1}$ for the 5f² or 5f³ uranium valence configurations.

Neutrons are therefore well suited for solving crystalline and magnetic structures. Inelastic scattering will not be described here as it goes beyond the scope of this thesis. Cross-sections due to phonons and magnons can be found in numerous textbooks [Price *et al.* (1986), Lovesey (1989), Collins (1989)].

1.3) Elements of X-ray scattering

In their interaction with matter, photons (or X-rays for wavelengths in the keV range) interact strongly with electrons. The cross-section describing the scattering of a X-ray photon on an atom is usually written in the form [James (1962), Warren (1990) and Jackson (1975)]:

$$\left(\frac{d^2\sigma}{d\Omega' dE'} \right)_{i \rightarrow f} = \left(\frac{e^2}{mc^2} \right)^2 \left| \sum_l^{\text{all atoms}} e^{i\mathbf{Q} \cdot \mathbf{R}_l} f_l(\bar{\mathbf{k}}_i, \bar{\mathbf{k}}_f; \hbar\omega) \right|^2 \delta(E_i - E_f + \Delta\omega) \quad (1.10)$$

where $f_l(\bar{\mathbf{k}}_i, \bar{\mathbf{k}}_f; \hbar\omega)$ is the scattering amplitude per atom⁷. The factor $(e^2/mc^2)^2 = r_0^2$ is the classical electron radius squared and corresponds to the "classical" cross-section of a single electron. Literally, the atomic scattering amplitude is therefore f times the single electron scattering.

In the forward direction ($Q=0$), the scattering amplitude by an atom is proportional to Z , the number of electrons per atom. When the scattering is not in the forward direction, the scattering amplitude becomes sensitive to the spatial extent of the charge distribution and the scattering amplitude becomes $f_l^0(Q) = \rho_l(Q) \bar{\mathbf{e}}_i \cdot \bar{\mathbf{e}}_f$ where $\rho_l(Q)$ is the Fourier

⁷This f -factor should not be confused with the $f(Q)$ introduced as the magnetic neutron form factor even if physically, both are related to the spatial extent of the scattering object.

transform of the charge distribution and $\bar{\epsilon}_i \cdot \bar{\epsilon}_f$, the Bragg-Thomson factor describing the polarization dependence of the scattering amplitude (introduced here for completeness).

Because an atom can behave as an oscillator at well-defined frequencies, anomalous dispersion corrections are needed to account for the energy dependence of the scattering. Taking the incident X-ray as the driving force for the oscillators, anomalous corrections can be separated into a real part $\Delta f'_l$ (in phase with the driving force) and an imaginary part $\Delta f''_l$ (90° out of phase) both related by a Kramers-Kronig transformation [James (1962)]. The total scattering amplitude, including the anomalous corrections, is written as:

$$f_l(\bar{k}_i, \bar{k}_f; E) = f_l^0(Q) + \Delta f'_l(E) + i \Delta f''_l(E) \quad (1.11)$$

These anomalous corrections will become important in the following discussion and it is necessary to make some comments at this point. The anomalous response at one frequency needs to include contributions from all the other resonances ω_i (also called absorption edges). The resulting sum forms a "continuum" described by :

$$\begin{aligned} \Delta f'_c(\omega) &= \sum_i \int_{\omega_i}^{\infty} \frac{\omega_i^2 (dg/d\omega)_i d\omega_i}{\omega^2 - \omega_i^2} \\ \Delta f''_c(\omega) &= \frac{1}{2} \pi \omega \sum_i (dg/d\omega)_i \end{aligned} \quad (1.12)$$

where $E = \hbar\omega$ is the incident photon energy and the oscillator density is defined as $(dg/d\omega)_i = \frac{mc}{2\pi^2 e^2} \mu(\omega)_i$. As an example, James (1962) calculated the K-edge response assuming a power law behavior for the oscillator density not too different from what is

observed experimentally: $(dg_K / d\omega)_i = A_i / \omega^3$ if $\omega > \omega_i$ and $(dg_K / d\omega)_i = 0$ if $\omega < \omega_i$.

For a K-edge, the anomalous corrections therefore become ($x = \omega / \omega_i$):

$$\Delta f'_c(x) = \frac{g_K}{x^2} \ln|x^2 - 1|$$

$$\begin{aligned} \Delta f''_c(x) &= \pi g_K / x^2 \text{ if } x > 1 \\ &= 0 \text{ if } x < 1 \end{aligned} \quad (1.13)$$

The characteristic lineshapes for this case are shown in Fig. 1-2. Qualitatively, the "continuum" response is a superposition of these curves centered at each of the different resonant frequencies.

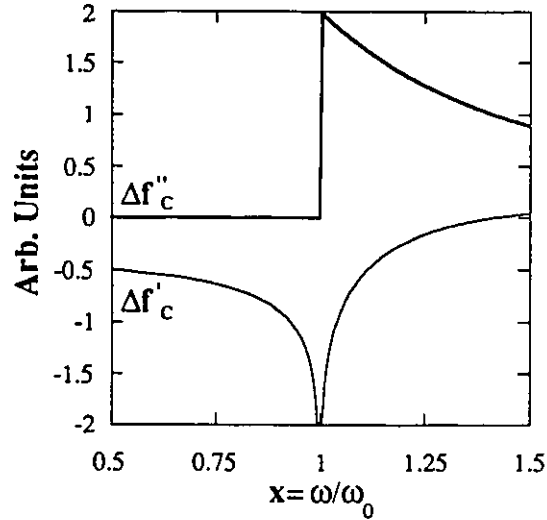


Figure 1-2: Real and imaginary part of the anomalous dispersion corrections in the vicinity of a resonance for K-edges [James (1962)].

In a more modern approach, the calculation of anomalous corrections requires the use of relativistic wave functions in order to compute the oscillator strengths [Cromer-

Lieberman *et al.* (1970)]. These calculations, found in GSAS⁸, are quite satisfactory far from an absorption edge. *At edge* however, the calculations lack some additional features that could be present, like white-lines or excitons [Philips *et al.* (1980)].

In certain materials, like Ge (K-edge) or Ta (L_{III}-edge) [Brown (1980)], a pronounced maximum appears in the absorption spectrum directly at the edge energy ($x=1$), similar to the one depicted in Fig. 1-3. As described by Cauchois *et al.* (1949), the maximum ("white line" or "ligne blanche") can originate either from the high density of final unoccupied states involved in the transition as is likely to occur in metals or HF systems or from the presence of many-body bound states or excitons as is likely to occur in insulators.

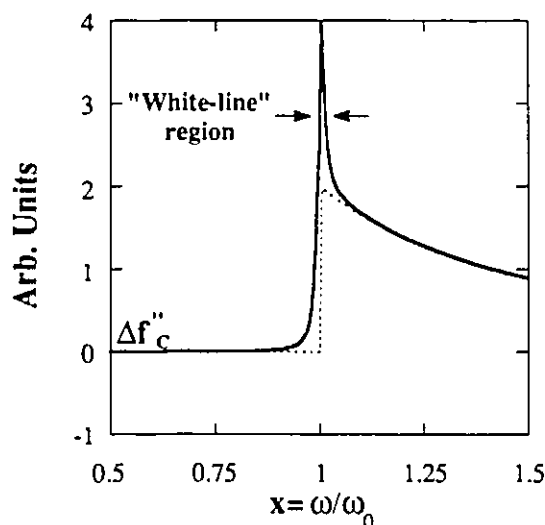


Figure 1-3: White-line in an absorption spectrum (continuous line) compared to the imaginary part from Fig. 1-2 (dotted line).

⁸GSAS stands for General Structure Analysis System, LANSCE, MS-H805, Los Alamos National Laboratory, Allen C. Larson and R.B. Von Dreele.

The large maximum present in the absorption spectrum (or in $\Delta f''$), like in Fig. 1-3, reveals a pronounced dipolar oscillator response at the resonant frequency [Brown (1980)]. Based on analysis of white-lines in edge spectra [Röhler (1985)], we write that the correction is additive to the "continuum" and that the total anomalous corrections can be written as:

$$\Delta f' = \Delta f'_c + \Delta f'_{WL} \quad (1.14)$$

$$\Delta f'' = \Delta f''_c + \Delta f''_{WL}$$

For the white-line, we can assume that the resonant spectrum is relatively sharp compared to the resonant frequency in such a way that the Lorentzian approximation (Breit-Wigner type) will hold near $\omega/\omega_0=1$ [see Fig. 1-4]:

$$\Delta f'_{WL}(\omega) = \frac{(\omega - \omega_0) \left(\frac{\Gamma}{2}\right)}{(\omega - \omega_0)^2 + \left(\frac{\Gamma}{2}\right)^2} \text{ and } \Delta f''_{WL}(\omega) = \frac{\left(\frac{\Gamma}{2}\right)^2}{(\omega - \omega_0)^2 + \left(\frac{\Gamma}{2}\right)^2} \quad (1.15)$$

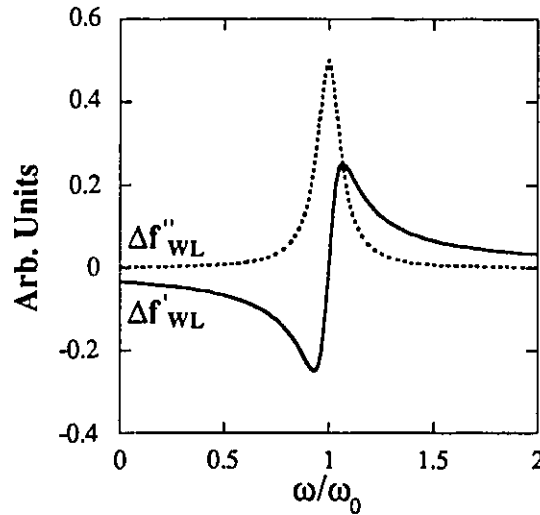


Figure 1-4: Real and imaginary part of anomalous corrections describing a white-line (Lorentzian).

Fig. 1-4 shows that at $\omega/\omega_0=1$, directly at the resonant frequency, the value of $\Delta f'_{WL} \approx 0$ while $\Delta f''_{WL}$ reaches its maximum. At resonance, the white-line correction will therefore affect only the imaginary part of the response function and not the real part. This set of arguments will be important in section 3.1.

At this point, only charge scattering has been considered and magnetic scattering has still not yet been taken into account. In the next section, non-resonant and resonant magnetic X-ray scattering cross-sections are introduced as corrections to the real and imaginary parts of the atomic scattering amplitude $f_i(\vec{k}_i, \vec{k}_f; \hbar\omega)$.

1.4) Magnetic X-ray scattering

The discovery of magnetic X-ray scattering dates back to the early 70s when DeBergevin *et al.* (1972) observed for the first time in a diffraction experiment on NiO, using the $\text{CuK}\alpha$ radiation from an X-ray tube, that photons can be sensitive to magnetism [Fig. 1-5]. This observation confirmed a theoretical prediction by Platzman *et al.* (1970). However, due to the prohibitive counting time, this method could not be used on a regular basis to study magnetic materials. Magnetic X-ray scattering requires more intense photon sources like synchrotrons.

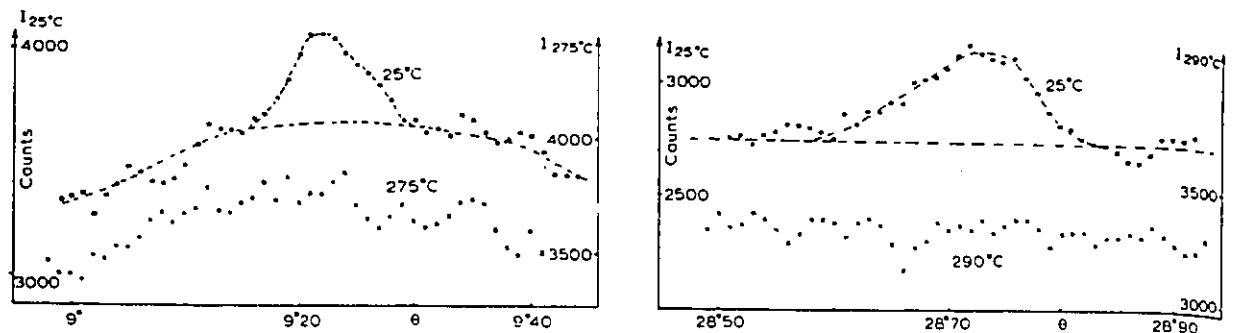


Figure 1-5: First observation of magnetic scattering in NiO using X-rays [from DeBergevin *et al.* (1972)].

The magnetic X-ray scattering cross-section is calculated using the Hamiltonian of an electron in a quantized electromagnetic field where the transition probability $W_{i \rightarrow f}$ [Eq. (1.4)] is expanded to second order. Elastic scattering events are described by terms in the expansion where the incident photon is annihilated and an outgoing photon is created with the same energy as the incident one. Such events are proportional to \vec{A}^2 , the photon

vector potential squared: $\bar{A}(\vec{r}) = \sqrt{\left(\frac{2\pi\hbar c^2}{V\omega}\right)}(\bar{\epsilon} c e^{i\vec{k}\cdot\vec{r}} + \bar{\epsilon}^* c^\dagger e^{-i\vec{k}\cdot\vec{r}})$. After grouping the terms, Blume (1985) found the single electron cross-section as:

$$\begin{aligned} \left(\frac{d^2\sigma}{d\Omega' dE'}\right)_{i \rightarrow f} &= \left(\frac{e^2}{mc^2}\right)^2 \left| \langle f | \sum_l e^{i\vec{k}'\cdot\vec{r}_l} | i \rangle \bar{\epsilon}' \cdot \bar{\epsilon} - i \frac{\hbar\omega}{mc^2} \langle f | \sum_l e^{i\vec{k}'\cdot\vec{r}_l} s_l | i \rangle \bar{\epsilon}' \times \bar{\epsilon} + \dots \right. \\ &\dots + \frac{\hbar^2}{m} \sum_n \sum_m \left(\frac{\langle f | \left(\frac{\bar{\epsilon}' \cdot \vec{P}_l}{\hbar} - i(\bar{k}' \times \bar{\epsilon}') \cdot s_l \right) e^{-i\vec{k}'\cdot\vec{r}_l} | n \rangle \langle n | \left(\frac{\bar{\epsilon} \cdot \vec{P}_m}{\hbar} + i(\bar{k} \times \bar{\epsilon}) \cdot s_m \right) e^{i\vec{k}\cdot\vec{r}_m} | i \rangle}{E_i - E_n + \hbar\omega_k - i\Gamma_n/2} + \dots \right. \\ &\left. \dots + \frac{\langle f | \left(\frac{\bar{\epsilon} \cdot \vec{P}_m}{\hbar} + i(\bar{k} \times \bar{\epsilon}) \cdot s_m \right) e^{+i\vec{k}\cdot\vec{r}_m} | n \rangle \langle n | \left(\frac{\bar{\epsilon}' \cdot \vec{P}_l}{\hbar} + i(\bar{k}' \times \bar{\epsilon}') \cdot s_l \right) e^{-i\vec{k}'\cdot\vec{r}_l} | i \rangle}{E_i - E_n - \hbar\omega_k - i\Gamma_n/2} \right)^2 \delta(E_i - E_f + \hbar\omega_k - \hbar\omega_{k'}) \end{aligned} \quad (1.16)$$

To extend the single electron picture to a many-electron atom in Eq. (1.16), the Fourier transform of the charge distribution ($\rho(Q)$) and the "continuum" anomalous corrections ($\Delta f'_c + i\Delta f''_c$), shown in Eq. (1.13), need to be added. The first term in Eq. (1.16) corresponds to the charge scattering amplitude already introduced in Eq. (1.11), $f_l^0(Q) = \rho_l(Q) \bar{\epsilon}_i \cdot \bar{\epsilon}_f$. By analogy with Eq. (1.10), the total scattering amplitude in Eq. (1.16) can be rewritten as $f = f^0 + f^{\text{mag}} + (\Delta f'_c + i\Delta f''_c)$. The magnetic part, f^{mag} , appears therefore as a correction to the anomalous corrections and is a function of, Γ , the width of the atomic resonance, s , the electron spin, P , its momentum, ϵ , the polarization of the photon and its energy, ω . As non-resonant and resonant scatterings belong to different scattering regimes, each case will be presented separately.

1.4.1) Non-Resonant Magnetic X-ray Scattering

In the *non-resonant* case, when the photon energy is far from any atomic resonant frequency ($E_i - E_a \ll \hbar\omega_k$ or far from all the absorption edges in the compound), the photon cross-section can be reduced to [Blume (1985)]:

$$\begin{aligned}
 \left(\frac{d^2\sigma}{d\Omega' dE'} \right)_{i \rightarrow f} &= \dots \tag{1.17} \\
 &= \left(\frac{e^2}{mc^2} \right)^2 \left| \left\langle f \left| \sum_i e^{i\mathbf{k}' \cdot \mathbf{r}_i} \right| i \right\rangle \bar{\mathbf{e}}' \cdot \bar{\mathbf{e}} - i \frac{\hbar\omega}{mc^2} \left\langle f \left| \sum_i e^{i\mathbf{k}' \cdot \mathbf{r}_i} \left(\frac{\vec{K} \times \vec{P}_i}{\hbar k^2} \cdot \bar{\mathbf{A}} + \bar{S}_i \cdot \bar{\mathbf{B}} \right) \right| i \right\rangle \right|^2 \delta(E_i - E_f + \hbar\omega_k - \hbar\omega_{k'}) \\
 &= \left(\frac{e^2}{mc^2} \right)^2 \left| \sum_i \left\{ \underbrace{\rho_i(Q) \bar{\mathbf{e}}' \cdot \bar{\mathbf{e}}}_{\text{Charge}} - i \frac{\hbar\omega}{mc^2} \underbrace{\left(\frac{1}{2} \bar{L}_i(Q) \cdot \bar{\mathbf{A}} + \bar{S}_i(Q) \cdot \bar{\mathbf{B}} \right)}_{\text{Magnetic}} \right\} \right|^2 \delta(E_i - E_f + \hbar\omega_k - \hbar\omega_{k'})
 \end{aligned}$$

with,

$$\bar{\mathbf{A}} = \bar{\mathbf{e}}' \times \bar{\mathbf{e}} \quad \text{and} \quad \bar{\mathbf{B}} = \bar{\mathbf{e}}' \times \bar{\mathbf{e}} + (\hat{\mathbf{k}}' \times \bar{\mathbf{e}})(\hat{\mathbf{k}} \cdot \bar{\mathbf{e}}) - (\hat{\mathbf{k}} \times \bar{\mathbf{e}})(\hat{\mathbf{k}}' \cdot \bar{\mathbf{e}}) - (\hat{\mathbf{k}}' \times \bar{\mathbf{e}}) \times (\hat{\mathbf{k}} \times \bar{\mathbf{e}}).$$

In the final step of Eq. (1.17), like before, the charge density has been introduced to account for the spatial extent of the atomic charge distribution. As in Eq. (1.16), the first term in Eq. (1.17) is the charge scattering. The non-resonant magnetic part, $f^{\text{mag}} = f^{\text{non-res}}$, appears as a correction of the order of $\hbar\omega/mc^2$ to the "continuum" anomalous corrections: $f = f^0 + f^{\text{non-res}} + (\Delta f'_c + i\Delta f''_c)$. At 3keV, $f^{\text{non-res}}$ is typically: $\left(\frac{\hbar\omega}{mc^2} \right)^2 / Z^2 \approx 10^{-7} \langle s \rangle^2$ smaller than charge scattering [from Blume (1985)].

The rather elaborate geometrical dependence of the non-resonant cross-section, contained in the vectors \vec{A} and \vec{B} in Eq. (1.17), is a remarkable property that can be used to separate the orbital and spin part of the overall magnetic moment [Blume *et al.* (1988)]. Also, because the scattering amplitude is a complex number, it is possible to use the interference between the magnetic and charge parts of the cross-section to enhance the magnetic intensity. This is particularly effective in a ferromagnet. The situation, however, does not apply to most antiferromagnets because charge and magnetic scattering do not occur at the same wave-vector.

1.4.2) Resonant Magnetic X-ray Scattering

Gibbs, Harshman *et al.* (1988) showed that when the incident energy of the synchrotron X-ray beam is tuned to an absorption edge of a magnetic atom, magnetic scattering could be dramatically enhanced. In Ho, this enhancement reached a factor 50 [Gibbs, Harshman *et al.* (1988), Gibbs *et al.* (1991)], but enhancements as large as 6 orders of magnitude, compared to non-resonant scattering, have been observed in UAs [Isaacs *et al.* (1989)].

In their experiment, Gibbs, Harshman *et al.* (1988) showed that when the X-ray energy is tuned to the Ho-L_{III} absorption edge, the helical magnetic structure of Ho gives rise to several magnetic harmonics all occurring at multiples of τ (the helix periodicity) [Fig. 1-6].

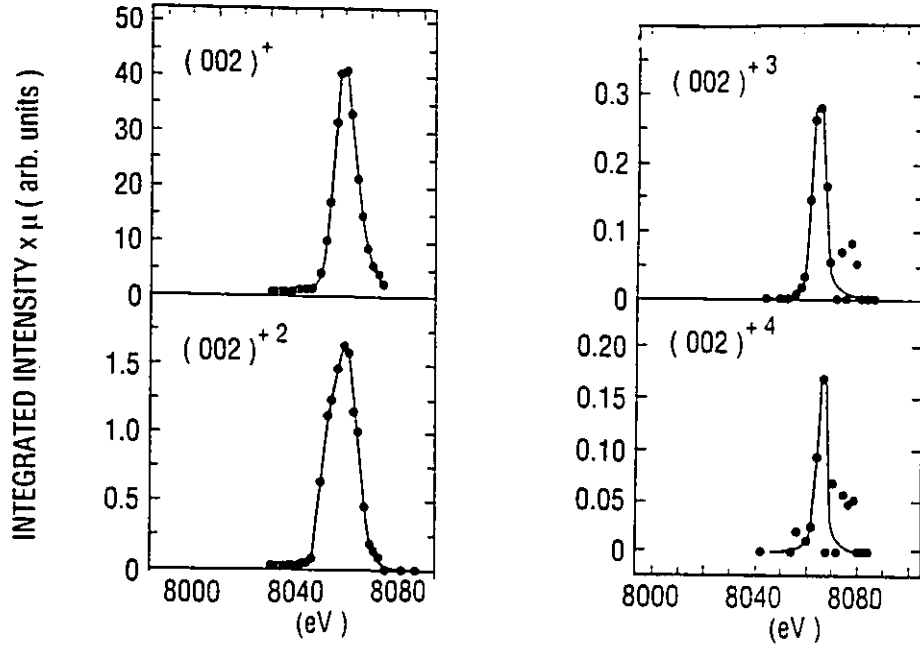


Figure 1-6: Resonant magnetic X-ray scattering at the L_{III} -edge of Ho [from Gibbs *et al.* (1991)]. The + indicates the magnetic harmonic in τ -units.

The presence of several harmonics at the Ho L_{III} -edge was interpreted as being due to a multipolar field expansion in the cross-section. In Ho, the L_{III} -edge is a mixture of an electric quadrupole transition and an electric dipole transition. For electric 2^L -pole transitions, the multipolar expansion of the $(\vec{A} \cdot \vec{P}_j)$ photon-electron interaction terms in $f_{\text{mag}}=f_{\text{res}}$ [Eq. (1.16)] can be written as [Hannon *et al.* (1988)]:

$$f_{\ell}(\vec{k}_i, \vec{k}_f; \hbar\omega) = f_{\ell}^0(Q) + f_{\ell}^{\text{res}}(\omega) + (\Delta f'_{\ell}(\omega) + i\Delta f''_{\ell}(\omega)), \quad (1.18)$$

where,

$$f^0(Q) \equiv \rho_{\ell}(Q) \vec{E}_f^* \cdot \vec{E}_i \text{ (the charge scattering)}$$

$\Delta f'_{\ell}(\omega)$ and $\Delta f''_{\ell}(\omega)$, the "continuum" anomalous corrections

and,

$$f^{\text{res}}(\omega) = 4\pi\lambda \sum_{M=-L}^L \left[\vec{E}_f^* \cdot \vec{Y}_{LM}(\hat{k}') \vec{Y}_{LM}^*(\hat{k}) \cdot \vec{E}_i \right] F_{LM}(\omega)$$

with the oscillator response function⁹,

$$F_{LM}(\omega) = \sum_{a,b} \frac{P_a P_b \Gamma_x(aNb; EL)}{2(E_a - E_b - \hbar\omega) - i\Gamma}$$

The physical process leading to the detection of magnetism in the resonant case ($E_i - E_n \cong \hbar\omega_k$ and $\Gamma_c \neq 0$) is quite different compared to the non-resonant case. Instead of being due to direct photon-electron scattering [Fig. 1-7], the magnetism in the resonant case is revealed through the creation of an excited state in the magnetic atom.

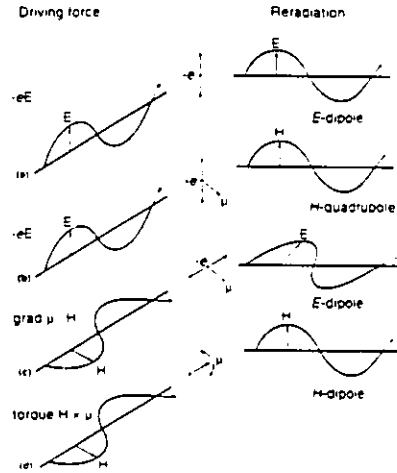


Figure 1-7: Classical mechanism of X-ray scattering from an unbound electron [from DeBergevin *et al.* (1981)].

The absorption of the incident photon by the magnetic atom promotes one of the core level electrons to an unoccupied valence level where the unpaired electrons responsible for the magnetism are lying. Due to the Pauli exclusion principle, the magnetic state imposes some constraints on the allowed transitions. Information regarding the magnetic state of the atom is eventually transferred to the polarization state of the outgoing photon after the decay of the excitation [Fig. 1-8]. The strength of the scattering is proportional

⁹The full description of the different parameters in $F_{LM}(\omega)$ is found in Hannon *et al.* (1988).

to the (virtual) oscillator response of the magnetic atom contained in the $F_{LM}(\omega)$ ¹⁰. Enhancements of many orders of magnitude compared to non-resonant scattering are possible for transitions involving an unfilled atomic shell or an atomic-like narrow band as the final state [Hannon *et al.* (1988)].

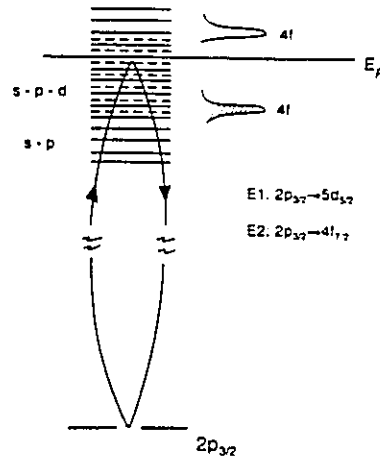


Figure 1-8: Schematic view of a core-hole excitation at a resonance in Ho [Gibbs (1992)].

As only the first few terms are expected to be large in a multipolar expansion¹¹, electric dipole (E1 or $L=1$) and electric quadrupole (E2 or $L=2$) are the most useful transitions used in resonant scattering. In uranium, the M_{IV} (transition from a filled $3d_{3/2}$ core electron to an unoccupied $5f_{5/2}$ valence state) and the M_V edge (transition from a filled $3d_{5/2}$ core electron to an unoccupied $5f_{7/2}$ valence state), are both *electric dipole* transitions ($L=1$) and in this case the corresponding scattering amplitude, including the $(2L+1)$ -harmonics, is given by [Hannon *et al.* (1988)]:

¹⁰In classical terms, this corresponds to the degree of polarizability of the charge distribution because a dipolar oscillator response is related to the dielectric constant of the charge distribution. For further details, see Jackson (1975), p.285.

¹¹Jackson (1975) chap 9.

$$f_{E\text{-dipole}}^{\text{res}}(\omega) = \frac{3}{4}\lambda \left\{ \bar{\mathbf{e}}_f^* \cdot \bar{\mathbf{e}}_i \left[F_{11}(\omega) + F_{1-1}(\omega) \right] - i(\bar{\mathbf{e}}_f^* \times \bar{\mathbf{e}}_i) \cdot \hat{\mathbf{z}} \left[F_{11}(\omega) - F_{1-1}(\omega) \right] + \dots \right. \\ \left. \dots + (\bar{\mathbf{e}}_f^* \cdot \hat{\mathbf{z}})(\bar{\mathbf{e}}_i \cdot \hat{\mathbf{z}}) \left[2F_{10}(\omega) - F_{11}(\omega) - F_{1-1}(\omega) \right] \right\} \quad (1.19)$$

Rewritten as $f_{E\text{-dipole}}^{\text{res}} = \alpha F_0 + i\beta F_1 + \gamma F_2$, each harmonic can be identified by the polarization dependence, in relation to the spin direction $\hat{\mathbf{z}}$, it contains.

In absence of magnetism, Eq. (1.18) and Eq. (1.19) must map onto the "regular" X-ray scattering near an absorption edge. The 0th harmonic, αF_0 with $F_0 = F_{11}(\omega) + F_{1-1}(\omega)$, does not contain any z-dependence and has some similarities with the *white-line* anomalous correction, $\Delta f'_{\text{WL}}$ and $\Delta f''_{\text{WL}}$, already introduced in Eq. (1.14). Although strictly speaking a *white-line* is not essential in the observation of resonant magnetic X-ray scattering, the formalism introduced here can be used to describe the energy dependence of the anomalous corrections directly at the edge [see DeBergevin (1992)]. The other two harmonics, the 1st (linear in $\hat{\mathbf{z}}$) and the 2nd (quadratic in $\hat{\mathbf{z}}$) are associated with magnetic scattering. The scattering amplitudes $F_1 = F_{11}(\omega) - F_{1-1}(\omega)$ and $F_2 = 2F_{10}(\omega) - F_{11}(\omega) - F_{1-1}(\omega)$ are difficult to obtain experimentally and need to be calculated by modeling the density of states and the atomic wave functions involved in the transition [Vettier (1994)].

If we now consider the case of total linear polarization for the incident radiation, we can express $f_{E\text{-dipole}}^{\text{res}}$ for two simple examples: a ferromagnet and an antiferromagnet. Using Eq. (1.18) and Eq. (1.19):

ferromagnet

$$\begin{aligned}
 f_{\text{Charge} + \text{Magnetic}} &= f^0(Q) + f_{E\text{-dipole}}^{\text{res}}(\omega) + (\Delta f'_C(\omega) + i\Delta f''_C(\omega)) \\
 &= \alpha\rho(Q) + \alpha F_0 + \beta F_1 + \gamma F_2 + (\Delta f'_C(\omega) + i\Delta f''_C(\omega)) \quad (1.20) \\
 &= \alpha\rho(Q) + \alpha\Delta f' + i\alpha\Delta f'' + \beta F_1 + \gamma F_2
 \end{aligned}$$

In the last step of Eq. (1.20), $F_0 = \Delta f'_{WL} + i\Delta f''_{WL}$ is included in $\Delta f' + i\Delta f'' = (\Delta f'_C + \Delta f'_{WL}) + i(\Delta f''_C + \Delta f''_{WL})$ according to Eq. (1.14). In ferromagnets, charge and magnetic scattering occur at the same wave-vector. Because all the terms in Eq. (1.20) are potentially c-numbers, an interference will exist between the magnetic terms (F_1 and F_2) and the charge terms. For a particular choice of geometry ($\gamma=0$), the scattered intensity is sensitive to a spin reversal operation.

simple antiferromagnet

$$\begin{aligned}
 f_{\text{Charge}} &= f^0(Q) + f_{E\text{-dipole}}^{\text{res}}(\omega) + (\Delta f'_C(\omega) + i\Delta f''_C(\omega)) \\
 &= \alpha\rho(Q) + \alpha F_0 + \gamma F_2 + (\Delta f'_C(\omega) + i\Delta f''_C(\omega)) \\
 &= \alpha\rho(Q) + \alpha\Delta f' + i\alpha\Delta f'' + \gamma F_2 \quad (1.21)
 \end{aligned}$$

$$f_{\text{Magnetic}} = i\beta F_1$$

In simple antiferromagnets, charge and magnetic scattering can occur at different wave-vector when the magnetic unit cell differ from the chemical unit cell. After making the correspondence $F_0 = \Delta f'_{WL} + i\Delta f''_{WL}$ and $\Delta f' + i\Delta f'' = (\Delta f'_C + \Delta f'_{WL}) + i(\Delta f''_C + \Delta f''_{WL})$ as before, we find that the antiferromagnetic Bragg peaks are proportional to the 1st harmonic only. For a special choice of geometry, $\gamma=0$, F_2 does not appear in the cross-section.

To end this section, it is interesting to compare the resonant energy profiles obtained by charge and magnetic scattering for the case of a simple antiferromagnet. Assuming a lorentzian lineshape¹² for both F_0 and F_1 and total linear polarization in the incident beam, the only difference between the charge and the magnetic resonance profiles comes from the presence of $f^0 = \alpha p(Q)$ in the real part of the charge scattering amplitude which has no energy dependence [see Eq. (1.21)]. The total response, $|f|^2$, is plotted for each case in Fig. 1-9. This comparison can offer a "test" to identify the origin of the scattering although the presence of absorption can lead to a very different charge resonance profile.

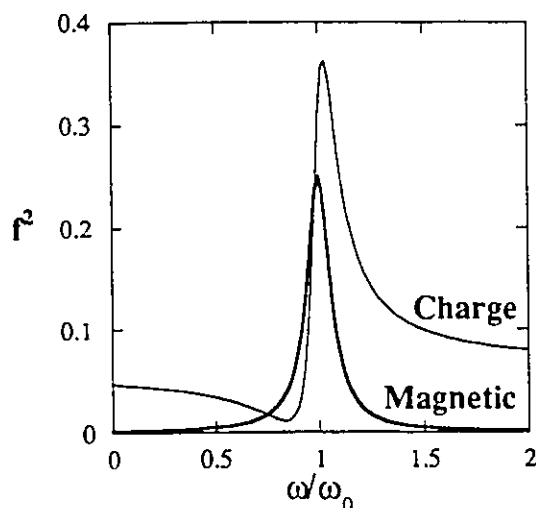


Figure 1-9: Schematic difference between charge and magnetic resonance profiles for a simple antiferromagnet. Scales are arbitrary.

¹² In many compounds, like in Ho and in UAs, the resonance profiles do not have a simple lineshape because of the superposition of electric-dipole and -quadrupole edges.

Chapter 2

Scattering Experiments at Neutron- and Light-Sources

Neutrons and X-rays are different scattering probes. The absence of charge (or electric field) enables the neutron to penetrate deeply into a sample. Typical neutron diffraction experiments usually deal with samples representing only a small fraction of the penetration depth and the neutron signal is averaged over the whole sample volume. The situation is different with photons. With penetration depths reaching $\approx 10^{-6}$ m in metals, photons are limited in their ability to probe the bulk of materials.

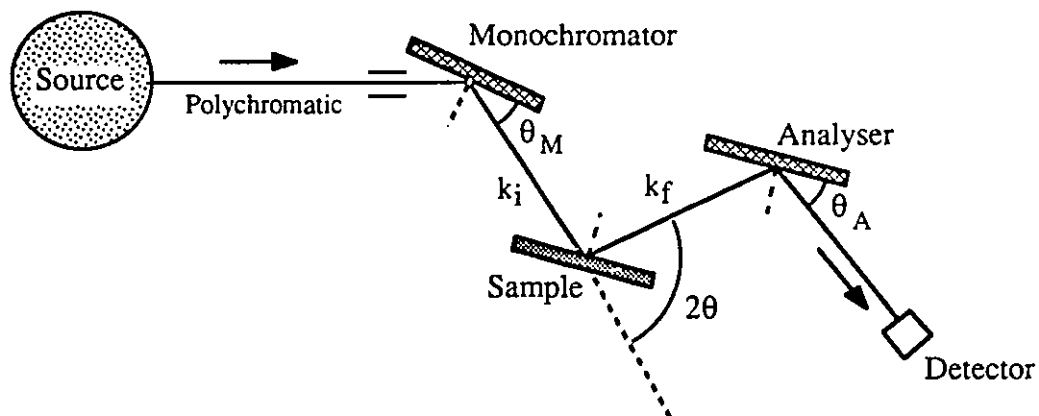


Figure 2-1: Triple-axis spectrometer.

The spectrometer needed to perform neutron or X-ray diffraction, schematically shown in Fig. 2-1, is fairly similar in principle. After its production by a source, the polychromatic beam (white beam) is first directed on a monochromator which has the purpose of

selecting a single wavelength using Bragg's law, $\lambda = 2d_M \sin(\theta_M)$ where d_M is the monochromator lattice spacing. A beam monitor, inserted between the monochromator and the sample, estimates the particle flux to normalize the counting time. The beam then scatters off the sample and may or may not lose energy during the process. In diffraction mode (no energy transfer), the detector arm is moved to close the scattering triangle by imposing $k_i = k_f$ [Fig. 1-1].

One of the main concerns in diffraction experiments, especially in the evaluation of Bragg intensities, is contamination by higher order radiation (λ/N -contamination). Experimentally, Bragg's law allows higher order wavelengths to scatter at the same Bragg angle if $\lambda/N = 2(d_M/N)\sin(\theta_M)$ is satisfied (both at the monochromator and at the sample). Some crystal structures, like Si(111) (diamond structure), can remove some of these contributions by selection rules. A filter can also be inserted in the beam to remove the unwanted wavelengths.¹³

Along the whole beam path, collimating devices can be inserted to modify the divergence of the beam and the resolution of the spectrometer. Collimation out of the scattering plane is usually not restrained to help gain intensity. In the gaussian approximation, the resolution function at the wave vector transfer \vec{Q}_0 is given by [Cooper *et al.* (1967) and Chesser *et al.* (1973)]:

$$R(\vec{Q}_0 + \Delta\vec{Q}) = R_0 \exp\left[-\frac{1}{2}(M_{11}\Delta Q_x^2 + 2M_{12}\Delta Q_x\Delta Q_y + M_{22}\Delta Q_y^2 + M_{33}\Delta Q_z^2)\right]$$

¹³ There are nevertheless some advantages in keeping a certain level of λ/N -contamination in the beam [See section 3.2.1 A)].

where R_0 and M_{ij} describe the resolution of the spectrometer and depend on its particular configuration. The resolution in the scattering plane is approximately an ellipse oriented with its longer axis along the direction of the scattering wave vector. Typical resolutions can be as good as $\Delta Q \approx 10^{-4} \text{ \AA}^{-1}$ and $\Delta E \approx 10 \text{ eV}$ for X-rays at synchrotron sources, and $\Delta Q \approx 0.002 \text{ \AA}^{-1}$ and $\Delta E \approx 0.5 \text{ meV}$ for thermal neutrons.

2.1) The spectrometer at a neutron facility

After being produced by fission reactions in a nuclear reactor (like the 110MW NRU reactor at Chalk River), thermal neutrons are moderated to energies typically of the meV range or to speeds of the order of km/s. The thermal neutron gas (Maxwell-Boltzmann distribution) has a kinetic energy peak at $3/2 k_B 300K \approx 1.8\text{\AA}$, which corresponds to interatomic distances in matter. Thermal neutron wavelengths are therefore well suited for diffraction from solids and liquids. This energy scale is also interesting because of its correspondence with elementary excitations in solids, such as lattice vibrations (phonons) and magnetic excitations.

The optics of a typical neutron triple-axis spectrometer usually deals with flat monochromators and analysers. To collimate the beam, an arrangement of Cd-coated blades (Soller slits) can be inserted before and after the sample. The plates separated by a given distance can lead to typical divergences in the range of $\approx 0.3^\circ$. Jaws (or beam shapers) can also be inserted in the beam path, but have little effect on the divergence of the beam, their main purpose being to reduce background.

To reduce higher order contamination in neutron scattering experiments the wavelength can be set at a smaller value than the peak of the Maxwell-Boltzmann distribution ($< 1.8\text{\AA}$). The reduction of the higher orders comes from the fact that: $E_{\lambda/N} = N^2 E_\lambda$ and the intensity associated with higher energy neutrons becomes small at large N (thermal distribution of the neutron gas). Higher order contamination can also be greatly reduced by the use of Pyrolytic Graphite (PG) filters used in transmission. This type of filter requires that the experiment be carried out at some well defined wavelengths where a

transmission window is found, such as 14.6 meV (first graphite window) and 34.1 meV (second graphite window). PG-filters can help remove 2nd and 3rd order neutrons.

All the neutron diffraction experiments presented in chapter 3 were performed using ⁴He cryostats that could cool the sample down to ≈ 2 K. As neutron scattering experiments are mostly conducted in the horizontal plane, heavy cryostats can be moved to satisfy the experimental conditions without severe problems¹⁴.

2.2) The spectrometer at a light source

Long being considered an undesired phenomenon with high energy accelerator rings, the radiative emission by charged particles transformed the synchrotron into a remarkable multipurpose machine in modern science. Compared to conventional X-ray tubes or rotating anodes, synchrotron radiation offers remarkable beam characteristics in intensity and spectral range for single crystal diffraction [Fig. 2-2].

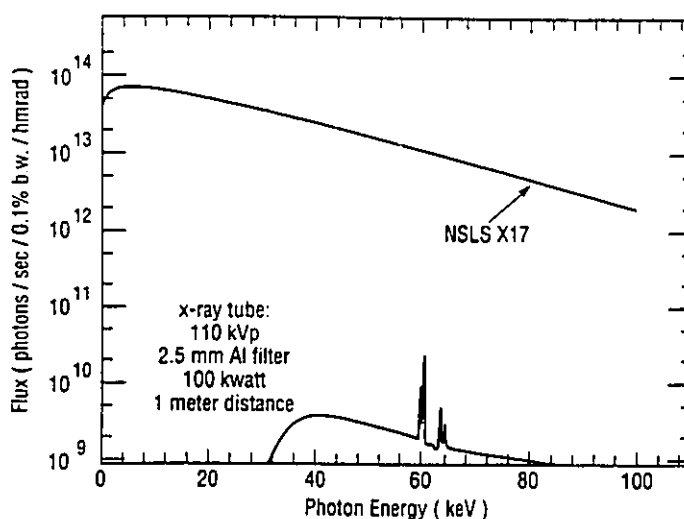


Figure 2-2: Typical photon flux vs. energy for a x-ray tube and at the NSLS X-17 beamport [from NSLS (1991)]

¹⁴Further experimental details about neutron scattering are found in Windsor (1987).

In synchrotrons, X-rays are produced by the radiative loss experienced by the electrons under acceleration [Jackson (1975), Winick (1980)]. In a synchrotron ring, bending magnets provide the necessary centripetal acceleration for creating the emission. However, because the electrons in the ring are relativistic (2.5 GeV at the National Synchrotron Light Source (NSLS)), the emission characteristics are quite different from the "classical" (non-relativistic) case. As shown in Fig. 2-3, the relativistic emission is well collimated, tangential to the ring [see the beamline orientations in Fig. 2-4] and linearly polarized in the plane of the ring¹⁵.

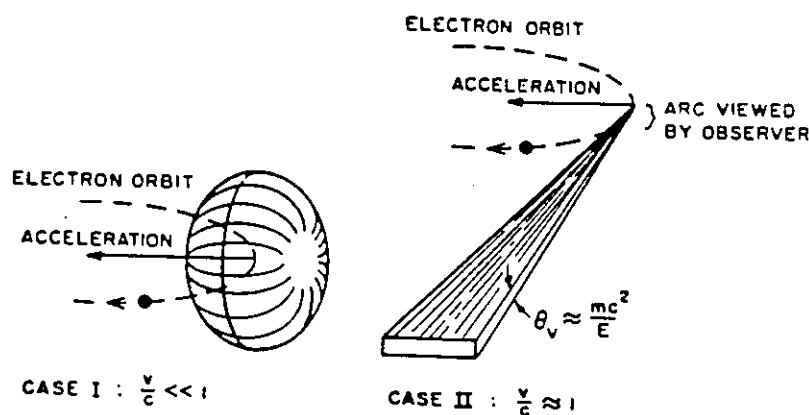


Figure 2-3: Radiation emission pattern of electrons in circular motions. Case I non-relativistic electrons. Case II, relativistic electrons [from Winick (1980)].

In recently built synchrotrons, like the 6 GeV accelerator at the European Synchrotron Radiation Facility (ESRF), not only has the energy of the circulating electrons been increased but insertion devices are used to further improve the intensity and the spectral range of the photon emission. Insertion devices, such as wigglers or undulators, reshape the emission characteristics using a spatially varying periodic magnetic field [Attwood *et al.* (1986)].

¹⁵The linear polarization of the incident photon beam is typically $\approx 90\%$ [McWhan (1990)].

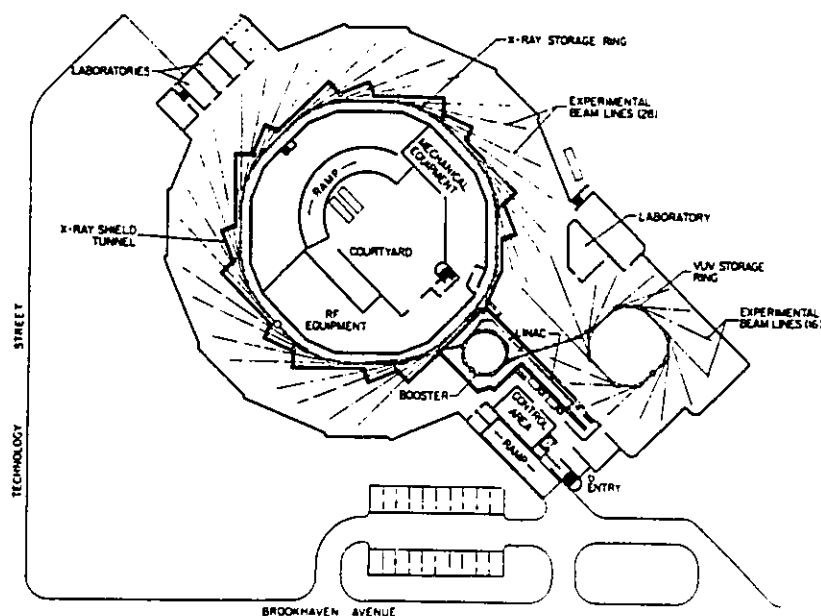


Figure 2-4: The X-ray and UV synchrotrons at NSLS [Winick (1980)].

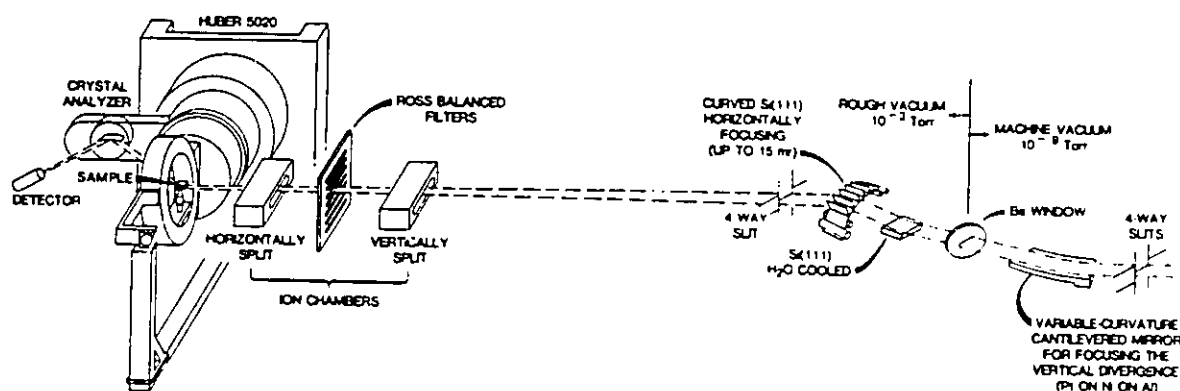


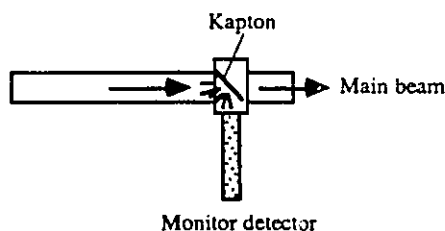
Figure 2-5: The optics of the Oak Ridge X-14 spectrometer at NSLS [Habenschuss *et al.* (1988)].

As seen in Fig. 2-5, X-ray spectrometers are usually operated in a vertical geometry (perpendicular to neutron scattering case). This configuration offers the best resolution in relation to the beam shape [Fig. 2-3] but represents a challenge when liquid-cryostats, such as a dilution fridge, need to be moved. The X-ray experiments presented in chapter 3 were made at two different spectrometers, X-14 (operated by Oak Ridge) and X-22c

(operated by BNL). Both spectrometers share some common characteristics like the use of a Ge(111) double focusing monochromator, but the X-14 spectrometer incorporates more elaborate optics [Fig. 2-6].

Absorption of photons in matter typically goes like $\approx Z^3/E^3$ where Z is the atomic number and E the photon energy [Luger (1980)]. Experiments at the uranium M-edges are considered *low* compared to typical synchrotron experiments (≈ 8 keV) and special care is needed to reduce absorption to a minimum. As 3keV-photons are easily absorbed in air (N_2), flight path elements are required to be held under vacuum separated by thin Be-windows or Kapton-windows. Flightpath elements need also to be brought as close to the sample as possible (limited by the constraints of the scattering angles) to reduce any air gap. Maintenance of a helium atmosphere via placing gas bags around the spectrometer is also a good way to remove air absorption. At 3.7keV, the linear absorption coefficient in air is typically 0.01cm^{-1} , while in Helium it is 0.0002cm^{-1} .

Absorption is also a concern in the construction of the beam monitor. In synchrotron experiments, at 8keV for example, ion-chambers can be used to estimate the incident photon flux and to control the piezo-alignment of the monochromator. These chambers cannot be used at 3keV because of the gas which acts as the detecting element. A construction similar to standard rotating anode experiments, using the rescattered radiation from a Kapton sheet, was necessary for all the X-ray experiments presented in chapter 3:



After being scattered by the sample, the radiation was detected by gas proportional counters (Ne, Xe). None of the experiments presented in chapter 3 required the use of an analyser. Elastic events were selected by setting the discriminator windows over a small energy range at the desired photon energy $E_i \approx E_f$. The energy window accepted by the proportional counters helped control the background level and reduce higher order contamination. However, because of their large stopping power, Xe detectors are more susceptible to higher order saturation than Ne detectors. Thin Ne detectors (mixed with CO_2) are nearly transparent to high energy X-rays and were used to improve the λ -signal at the uranium M-edges.

As we have seen, neutron and X-ray diffraction differ by the level of absorption each probe experiences in matter. Since X-ray diffraction is more affected by such effects, an understanding of absorption effects in the sample is required. Before presenting the results obtained on the U-based HFS in chapter 3, the next two sub-sections give an account of how absorption effects can be treated in X-ray scattering.

2.2.1) Bragg scattering with absorption

It is well known that when a beam passes through a sample, the intensity is depleted by an exponential decay law $I = I_0 e^{-\mu t}$, where μ is the absorption coefficient and t the thickness of material. In diffraction experiments, some other considerations are necessary because the scattering event is in reflection geometry. When the diffracting planes are not parallel to the surface of the crystal, a correction is needed for the asymmetry. In the thick slab approximation, when the crystal is thick enough so that no

beam is transmitted, this asymmetric absorption can be calculated using the angles defined in Fig. 2-6.

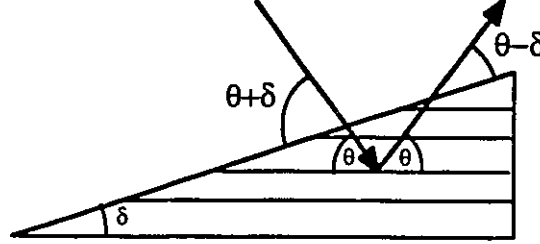


Figure 2-6: Asymmetric reflection [James (1962)].

If we define the entry angle as $\theta + \delta \equiv \theta_1$ and the exit angle as $\theta - \delta \equiv \theta_2$, the sums of the beam paths inside the crystal can be written as:

$$P_{\text{obs}} = P_0 \int_0^{\infty} e^{-\mu \left(\frac{x}{\sin(\theta_1)} + \frac{x}{\sin(\theta_2)} \right)} dx / \sin(\theta_2) \quad (2.1)$$

which gives after integration:

$$P_{\text{obs}} = \frac{P_0}{\mu \left(1 + \frac{\sin(\theta_1)}{\sin(\theta_2)} \right)} \quad (2.2)$$

This is written for convenience as:

$$P_{\text{obs}} = P_0 \frac{1}{2\mu} \cdot \frac{1}{\frac{1}{2} \left(1 + \frac{\sin(\theta + \delta)}{\sin(\theta - \delta)} \right)} = P_0 B(\mu) A(\delta) \quad (2.3)$$

Clearly $A(0)=1$ is θ -independent when the reflection is symmetric ($\delta=0^\circ$) [James (1962)].

Real crystals are not monolithic but are made of mosaic blocks. The asymmetric absorption correction, shown in Fig. 2-6, is valid for powders and mosaic crystals when the absorption inside each mosaic block is small [James (1962)]. However, when the reflected power is large, as for Bragg peaks at resonance [see section 3.1.2 B)], the reflectivity of each mosaic block can be modified by *primary extinction*. Zachariasen (1945) established a criterion to help determine the *absorption regime* of the mosaic blocks:

$$W = \frac{r_0 \lambda |f| t_0}{V} \quad (2.4)$$

where $r_0=2.82\text{fm}$, λ the wavelength, f the scattering amplitude of the reflection, t_0 the effective thickness of the block (being at most the penetration depth if the block is larger), and V the volume of the unit cell. In perfect crystal theory, there are two absorption regimes depending of the balance between the intensity of the Bragg reflection and the thickness of the mosaic blocks; when $W \gg 1$ the blocks are said to be in the *strong reflected power limit* ("*thick crystals*") while for $W \ll 1$ the blocks are said to be in the *small reflected power limit* ("*thin crystals*") [Zachariasen (1945) and Warren (1990)].

When the reflected power is *small* ($W \ll 1$), or when the mosaic blocks are thin, absorption within the mosaic blocks can be neglected and the observed intensity from a crystal is given by the Darwin function:

$$I_{\text{obs}} = I_0 \left(\frac{1 + \sigma^2}{4 (g^2 + \eta^2)} \right) \quad (2.5)$$

where the parameters, defined in Warren (1990), are:

$$\eta = \frac{\pi \sin(2\theta) (\theta - \theta_0)}{D\lambda (f_0 + \Delta f)}, \quad \sigma = \frac{\Delta f'}{(f_0 + \Delta f)}, \quad \text{and} \quad g = \frac{\mu}{2D(f_0 + \Delta f)}$$

and $D = r_0 \lambda N P$ (here N is the atom density and P a polarization factor associated with the radiation). The parameter η has some connections with the angle θ (sample rotation) and θ_0 is the "refracted" Bragg peak position.

It can be shown that in this limit, after integration over η , the reflected power in the symmetric case is only modified by a constant μ , the absorption coefficient:

$$\frac{P}{P_0} \propto \int \frac{I}{I_0} d\eta \propto \frac{|f|^2}{2\mu} \equiv B(\mu) |f|^2 \quad (2.6)$$

which is the same result found with $\delta=0^\circ$ in Eq. (2.3).

When the absorption within the blocks cannot be neglected ($W \gg 1$), whether the intensity of the Bragg reflection is large (like when the incident energy is set to an absorption edge) or that the mosaic blocks are thick, the observed intensity from a crystal becomes more complicated because of optical effects. In this case, the full expression takes the form:

$$I_{\text{obs}} = I_0 \frac{1 + \sigma^2}{g^2 + \eta^2 + Z \pm 2Z^{1/2} \left(g \cos \frac{\Phi}{2} + \eta \sin \frac{\Phi}{2} \right)} \quad (2.7)$$

with $Ze^{i\varphi} = (1 + i\sigma)^2 + (g + i\eta)^2$. The integration of Eq. (2.7) over η would give the reflected power of the Bragg reflection but the final analytical form of $B(\mu)$ is complicated. To get some insight about this effect, Fig. 2-7 shows the intensity lineshape of a "θ-rock" (variable η) for several values of μ . Zachariasen (1945) estimated from Eq. (2.9) that weak reflections are more likely to be reduced in intensity by primary extinction compared to strong reflections.

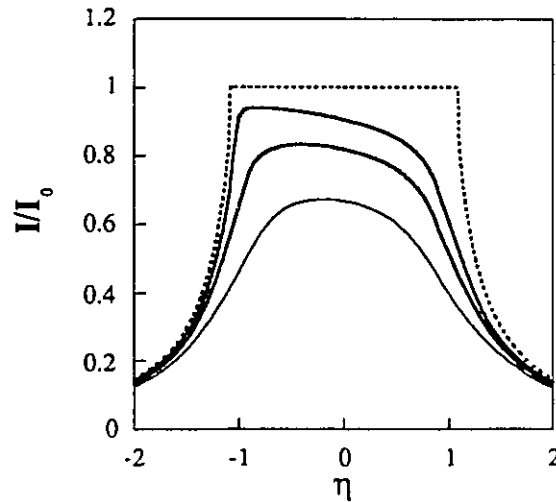


Figure 2-7: Bragg intensity vs. η for different absorptions. The dotted line is the Darwin solution [Eq. (2.2)] without absorption [Adapted from Warren (1990)].

In addition to primary extinction, *power loss due to diffraction* can be important (*secondary* extinction). In a mosaic crystal, the radiation already scattered by the blocks at the surface can remove an important part of the incident beam and reduce the flux available for the blocks deeper in the crystal. Corrections in the *strong reflected power limit* ($W \gg 1$) are complicated but in the *small reflected power limit* ($W \ll 1$) [Eq. (2.6) and (2.3)]:

$$\frac{P}{P_0} \equiv \frac{|f|^2}{2\mu'} \quad (2.8)$$

where the modified absorption coefficient, $\mu' \approx \mu + g |f|^2$, contains a term proportional to the strength of the reflection. Therefore, secondary extinction preferably reduces the intensity of strong reflections compared to weak reflections. As both effects (*primary* and *secondary* extinction) modify the intensities in different directions, the *absorption regime at resonance* (when the reflecting power is large) is not trivial to estimate.

To end this section, it is worth mentioning that perfect crystal theory has another interesting use in monochromator design. Often in the literature monochromators are said to be "detuned" [Materlik *et al.* (1980)]. This procedure is quite useful to filter higher order contamination and is essential when working at the uranium M-edges. Double monochromators are usually set in the symmetric-symmetric geometry i.e. the angle between the entry and exit rays make the same angle with the face of the crystal [see Fig. 2-6 with $\delta=0^\circ$]. But when one of the two monochromators is slightly rotated such that the reflection is just asymmetric ($\delta \neq 0^\circ$), the intensities are maximized at exit angles depending on the incident wavelengths. By maximizing on λ , all the other wavelengths in the beam are greatly reduced as shown in Fig. 2-8.

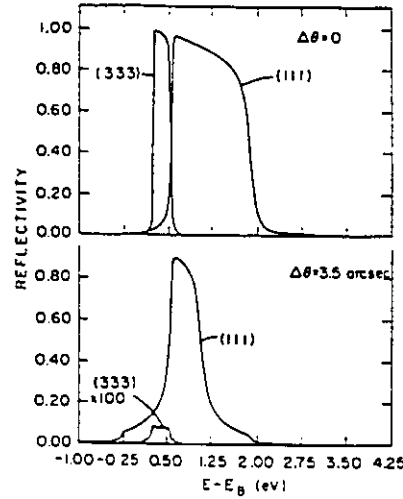


Figure 2-8: Reduction of the higher-order reflection by detuning the Si(111) reflection [Heald (1988)].

2.2.2) Fluorescence and absorption corrections

When thin foils of a material are not available (as is the case with the HFS considered in this thesis), indirect methods are needed to estimate the absorption coefficient μ . The optical theorem¹⁶ states that "the total cross section of a scatterer is equal to the imaginary part of the forward scattering amplitude" [McWhan *et al.* (1990)]:

$$\mu = 2\lambda N \Im(f(\theta = 0), \epsilon_f = \epsilon_i) = 2\lambda N(\Delta f'') \quad (2.9)$$

This correspondence comes from the fact that optically, $\Delta f'$ and $\Delta f''$ are both related to the index of refraction, $n=1-\nu$, where $\nu = \frac{\lambda^2 r_0}{2\pi} N f(0)$ is the optical phase shift. In Prins' formulation, the imaginary part of n (and so of f) is the absorption coefficient [James (1962)].

¹⁶Jackson (1975), p.453.

Therefore, if the main absorption channel in a material comes from the absorption of the atomic oscillators, the re-emitted photons (over the 4π solid angle) can give an account of the absorption. The incoherently re-emitted radiation is the fluorescence.

After a core-hole has been created by the absorption of the incident photon, non-radiative Auger emission and fluorescence emission are competing phenomena [Fig. 2-9]. Auger emission is favored in low Z materials and decreases at higher Z . Fluorescence is therefore more probable in high Z materials and constitutes a good decay channel with uranium atoms.

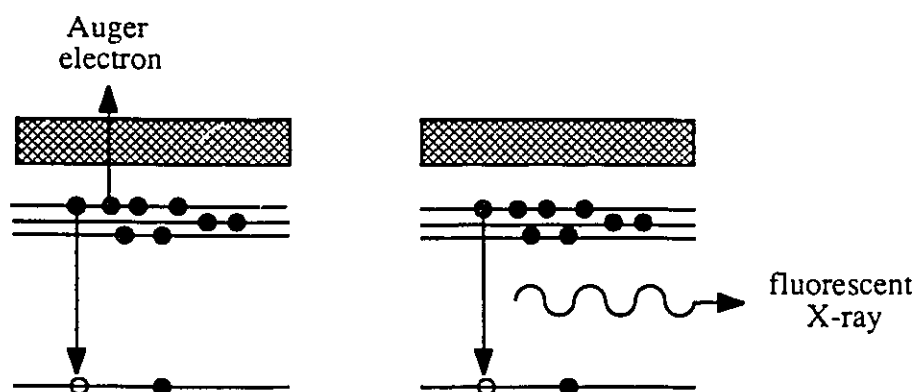


Figure 2-9: Auger and fluorescence emission after the creation of a core-hole [Adapted from Heald (1988)].

In thick crystals, the fluorescent spectrum is altered by auto-absorption effects which depend on the take-off angle of the emitted photon and the depth of the emission [see Fig. 2-10]. Tröger *et al.* (1992) pointed out that measurements that try to minimize the take-off angle are very sensitive to surface effects, and therefore less precise.

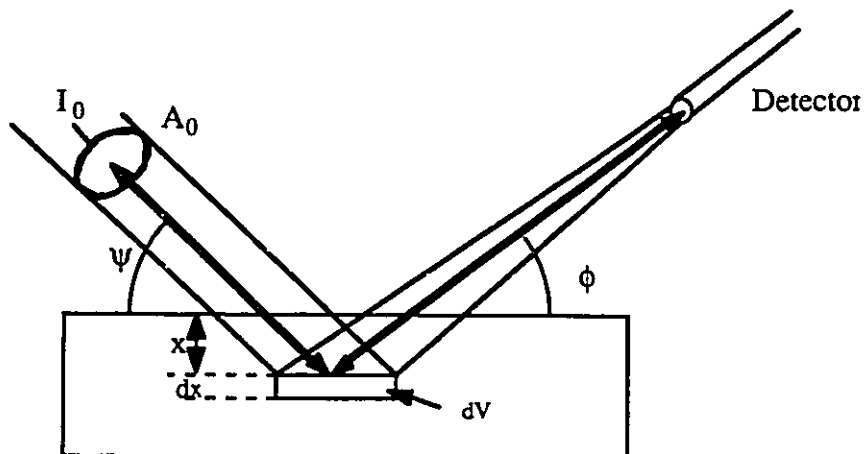


Figure 2-10: Fluorescence from a thick slab [from Sparks (1980)].

Using the angles defined in Fig. 2-10, accurate geometrical corrections are possible and for a thick slab [Heald (1988)]:

$$\mu'(E) = \frac{I_f}{I_0} \propto \frac{\mu(E)}{(\mu_T(E) + \mu_T(E_f) \frac{\sin \psi}{\sin \phi})} \quad (2.10)$$

This geometrical correction [Eq. (2.10)] shows that a "raw" fluorescence spectrum is not a direct measurement of absorption. In this equation, $\mu(E)$ is the absorption of the fluorescing atom and $\mu_T(E)$ is the total absorption coefficient of all the atoms in the unit cell (including the fluorescing atom). The other term in the denominator, $\mu_T(E_f)$, is the auto-absorption factor. Near an absorption edge, only the absorption of the fluorescing atom changes while the absorption of the other elements in the unit cell remain relatively constant over the same energy range. When Eq. (2.10) is modified to describe the U-based HFS it approximately becomes:

$$I_f(E) = C \frac{\mu_U(E)}{\mu_U(E) + \mu_{\text{mat}} + \mu_U(E_f) + \mu_{\text{mat}}} \quad (2.11)$$

where μ_U is the uranium absorption coefficient and μ_{mat} refers to the other atoms in the unit cell (other than uranium). E_f is the fluorescing energy and can be considered the edge energy ($E_f=3728\text{eV}$ at the M_{IV} -edge). The angular correction was set to 1 since our measurements were performed with $\psi=\phi$.

Using the calculated values for μ_T above and below the edge from Cromer-Lieberman's algorithm, $\mu_U(E_f)$, was found by imposing a consistent overall scaling factor C over the whole energy range in Eq. (2.11). Table 2-1 gives the total absorption coefficient near the M_{IV} absorption edge for the U-based HFS studied in this thesis.

M_{IV} -edge $E_f=3728\text{ eV}$	$\mu_T(3700\text{ eV})$ (cm^{-1})	$\mu_T(3728\text{ eV})$ (cm^{-1})	$\mu_T(3750\text{ eV})$ (cm^{-1})	$1/\mu_T(3728\text{ eV})$ (\AA)	$\mu_U(3728\text{ eV})$ (cm^{-1})
URu ₂ Si ₂	11372.2	21500	13095.3	4700	15500
UPd ₂ Al ₃	10715.6	18400	12175.6	5500	12400
UNi ₂ Al ₃	6021.9	29300	7636.6	3500	27900
					<i>≈ 18500</i>

Table 2-1: Absorption coefficients obtained from fluorescence curves for the U-based HFS. $1/\mu_T(3728\text{ eV})$ is the penetration depth and $\mu_U(3728\text{ eV})$ is the estimated uranium white-line. The value in italic is the value reported by Langridge *et al.* (1994) from UAs.

Some concerns can be found in the literature about the accuracy of the fluorescence method to evaluate the absorption for U-alloys. As mentioned by Tang *et al.* (1992), there is some evidence that fluorescence methods are inconsistent with the total-electron-yield in other U-based compounds (like UO₂, USb, etc.). One possible explanation for discrepancy may come from the strong concentration of the fluorescing element (here uranium) which could increase multiple auto-absorption effects. For the U-based HFS

compounds, this effect may have been important since the uranium mass concentration represents: 48% in URu_2Si_2 , 54% in UNi_2Al_3 and 44% UPd_2Al_3 . Fluorescence techniques are known to work best when the fluorescing element is in small concentration [Heald (1988)]. Nevertheless, the $\mu_{\text{U}}(3728 \text{ eV})$ given by Langridge *et al.* (1994) seems very similar to our measurement.

To conclude this chapter, the resonance profile at the (001) charge reflection of UPd_2Al_3 can help visualize the importance of absorption corrections (near the M_{IV} absorption edge). The observed intensity ($I \times \mu$) in Fig. 2-11 shows that the corrected lineshape is similar to the resonance profile already calculated for charge reflections in an antiferromagnet [see Fig. 1-9].

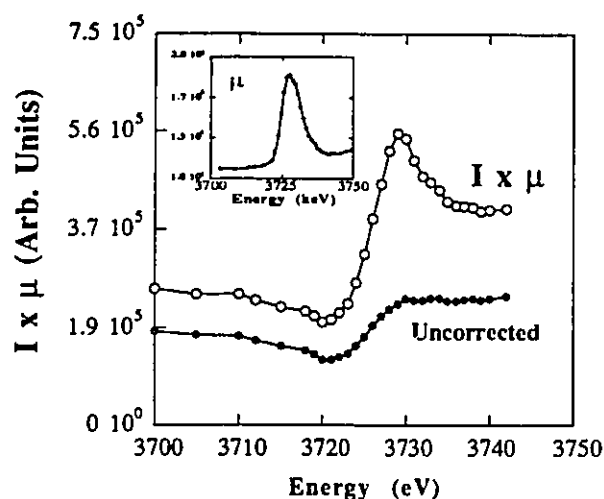


Figure 2-11: Uncorrected and corrected ($I \times \mu$) resonance profiles at (001) charge reflection of UPd_2Al_3 . The inset shows the energy dependence of the absorption coefficient (μ) extracted from a fluorescence measurement.

Chapter 3

Magnetic Structures and Phases of Uranium-based Heavy Fermion Superconductors

In previous chapters, we have seen how neutrons and photons can be used to study magnetism in condensed matter. We particularly emphasized the conditions leading to resonant magnetic X-ray scattering and how the cross-section differs from conventional neutron scattering. In this chapter, both techniques are used to study the magnetic structures and phases of URu_2Si_2 , UPd_2Al_3 , and UNi_2Al_3 .

Our measurements on the magnetic state of URu_2Si_2 follow earlier work by Isaacs *et al.* (1990) who have shown, using resonant magnetic X-ray scattering, that even with a small ordered magnetic moment ($\approx 10^{-2}\mu_B$), a measurable signal can be obtained. Using the uranium M_{IV} -edge as the incident radiation energy, the (003) magnetic Bragg peak appeared at a count rate of 8 cts/sec. This measurement was performed at only one magnetic reflection. Using a two stage dispersive cryostat, we extended access into reciprocal space and measured several charge and magnetic Bragg peak intensities. Our measurement constitutes a good verification of the selection rules of the resonant X-ray cross-section.

We also wanted to establish the magnetic structures and phases of the new HFS UPd_2Al_3 and UNi_2Al_3 . To achieve this task we used both neutron and resonant X-ray scattering techniques.

The UPd_2Al_3 sample available for the present thesis work was polycrystalline. It was believed that the very small synchrotron X-ray beams ($\approx 1\text{mm}^2$) could be used to isolate the single-crystallites at the surface to obtain single crystal properties. Using this important feature and the special selection rules of the resonant X-ray cross-section, experiments were performed on this compound which sought to determine the spin orientation in the basal plane and address some important questions related to its magnetic phases.

An extensive study of the magnetic state of UNi_2Al_3 could be done following the successful growth of a single crystal at McMaster University. This material was known to have a magnetic phase [Geibel *et al.* (1991)] but neutron experiments on powders were not sensitive enough to reveal the magnetic order. The incommensurate magnetic Bragg peaks, found after an extensive search in reciprocal space on the single crystal, is the first direct observation of long range magnetic order in this compound. It is also the first incommensurate structure among the HFS compounds. Some additional measurements about the evolution of the incommensurate order in high magnetic fields and an estimate of the uranium valence in this compound are also presented.

Because we eventually want to compare the magnetic state of the new UT_2Al_3 ($\text{T}=\text{Ni}, \text{Pd}$) compounds with the "classical" HFS (UPt_3 and URu_2Si_2), it is worthwhile to summarize here some of the remarkable magnetic properties shared by both compounds. In addition to the very small ordered moment ($\approx 10^{-2} \mu_B$), UPt_3 and URu_2Si_2 both have a

characteristic linear magnetic order parameter which displays a change of slope at low temperature. In addition the magnetic order they display at low temperature is characterized by a finite correlation length which extends over hundreds of Angstroms only in the ordered phase (250Å in UPt_3 and 450Å in URu_2Si_2). The magnetic structures and some features of interest from both compounds are shown in Fig. 3-1 and Fig. 3-2.

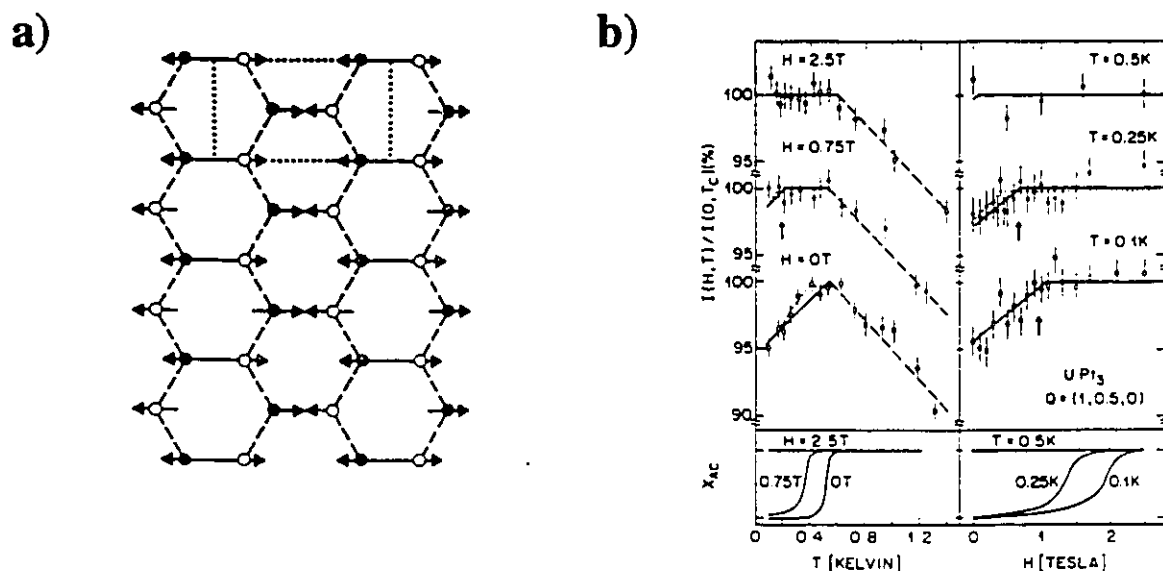
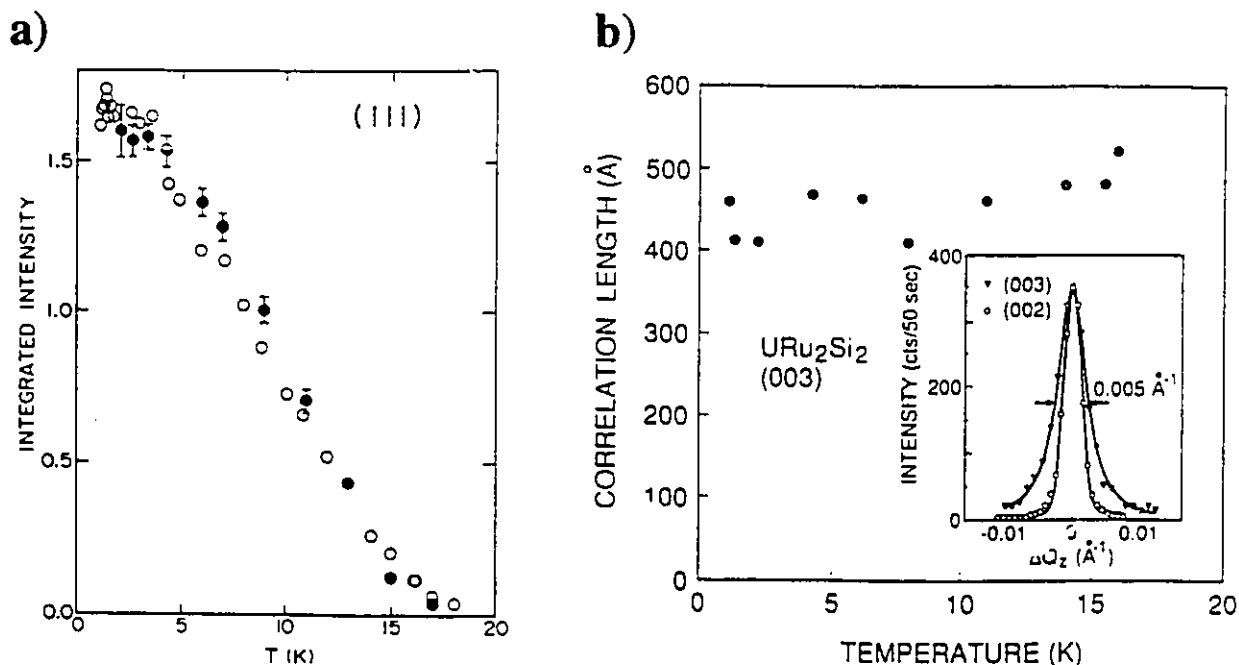


Figure 3-1: a) Magnetic structure associated with the long range magnetic order in UPt_3 [Goldman *et al.* (1986)]. b) Magnetic order parameter in the superconducting phase in UPt_3 [Aeppli *et al.* (1989)].



c)

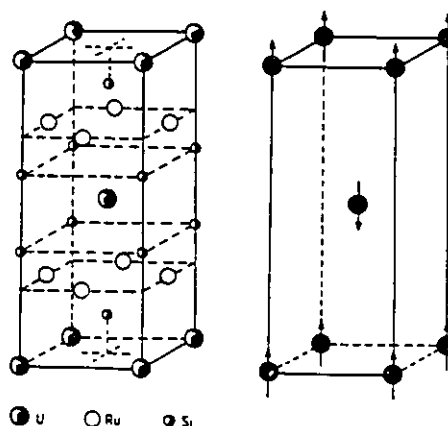


Figure 3-2: a) Magnetic order parameter below 17K [Isaacs *et al.* (1990)]. b) Finite magnetic correlation length in URu_2Si_2 [Isaacs *et al.* (1990)]. c) Crystal and magnetic structures of URu_2Si_2 [Broholm *et al.* (1991)].

3.1) Resonant X-ray cross-section in URu_2Si_2

In an earlier study of UAs at the uranium M_{IV} -edge, Isaacs *et al.* (1989) have shown that the magnetic intensities obtained by resonant magnetic X-ray scattering were well reproduced by the 1st harmonic of the electric-dipole cross-section [Eq. (1.19)]. To reach this conclusion, these authors made measurements over 6 different magnetic reflections at approximately the *same* Q -value. Thus, the measurement was not sensitive to a possible Q -dependence in the X-ray cross-section. The question of whether a Q -dependence (similar to a form factor) is present in the resonant X-ray cross-section is not an irrelevant one. As mentioned by Wasedo (1984), this Q -dependence is intimately related to the dipolar approximation invoked to describe the scattering process which may fail with M- and N-edges. To investigate if the electric-dipole selection rule still holds for *different* Q -values and in an attempt to extract meaningful physical properties using the resonant

technique (such as the moment size) a series of "polarized"¹⁷ resonant X-ray experiments were performed on URu₂Si₂ at the uranium M_{IV}-edge.

3.1.1) Experimental setup and results

The crystal and magnetic structure of URu₂Si₂ have been well established by neutron scattering [Broholm *et al.* (1991)]. As shown in Fig. 3-2 a), URu₂Si₂ has a body-centered tetragonal ThCr₂Si₂ structure with lattice parameters $a=4.124\text{\AA}$ and $c=9.582\text{\AA}$ at 4.2K. Below 17K, it undergoes a phase transition to an antiferromagnetic phase where the magnetic moments, localized at the uranium atoms, point along the c-axis [see Fig. 3-2 c)]. It is superconducting below $T_c=1.2\text{K}$.

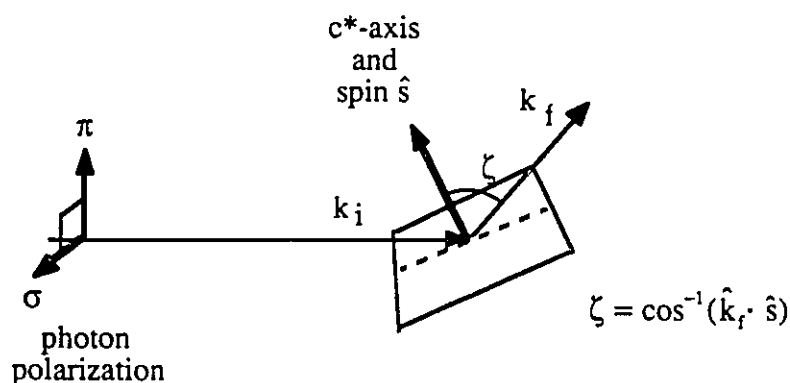


Figure 3-3: Scattering geometry of the X-ray experiments on URu₂Si₂ at X-22c. The vectors k_i and k_f indicate the direction of the radiation in relation to the sample. The σ and π -polarization vectors refer to the photon polarization of the incident radiation in relation to the scattering plane.

In the experiments performed at the NSLS X-22c beamline, the cleaved sample (which was a few millimeters thick) was mounted on a Cu-block such that its c-axis was perpendicular to the surface of the crystal [see Fig. 3-3]. The sample could be cooled

¹⁷With no polarizing analyser. This experiment was σ -polarized due to the inherent polarization of synchrotron radiation.

down to $\approx 4\text{K}$ (below $T_N=17\text{K}$ but above $T_C=1.2\text{K}$) using a two stage closed cycle displacer refrigerator. Thermal conduction was improved by putting the sample in He exchange gas inside a Be-hat. A mylar reflector shield was also necessary to reduce radiative heating. The whole sample area was enclosed by an outer Be-can and held under vacuum.

The set of accessible reflections, due to the limits imposed by the incident wavelength ($M_{IV}\text{-edge} = 3.33\text{\AA}$) and by geometrical limitations, included the magnetic (001), (003), (005), (104) and the charge (002), (004), (103) Bragg reflections. The radial scans at the $M_{IV}\text{-edge}$ [Fig. 3-4] were collected in two different experiments referred to as 1991 (Nov. 1991) and 1992 (Aug. 1992) respectively. The measurements were made with a Xe detector. Similar scans performed at the uranium $M_V\text{-edge}$ did not reveal any magnetic scattering.

After correction for a constant background, the 1991-(005) magnetic Bragg peak was observed at a peak count rate of 28 counts/sec while the 1991-(003) reflection was observed at 9 counts/sec [Fig. 3-4 b)]. The latter value is in the range obtained by Isaacs *et al.* (1990) on the same sample but at another spectrometer (X-14).

At the (001) magnetic Bragg reflection, the sensitivity of both 1991 and 1992 experiments were limited by the presence of a large temperature independent background estimated at 7 counts/sec. This background, due to a rod of charge scattering along the (00L)-direction, could not be separated from the magnetic signal since no polarization analyser was used. From the scatter of the points, the (001)/(005) ratio is less than 0.1 (or (001)/(003) < 0.3).

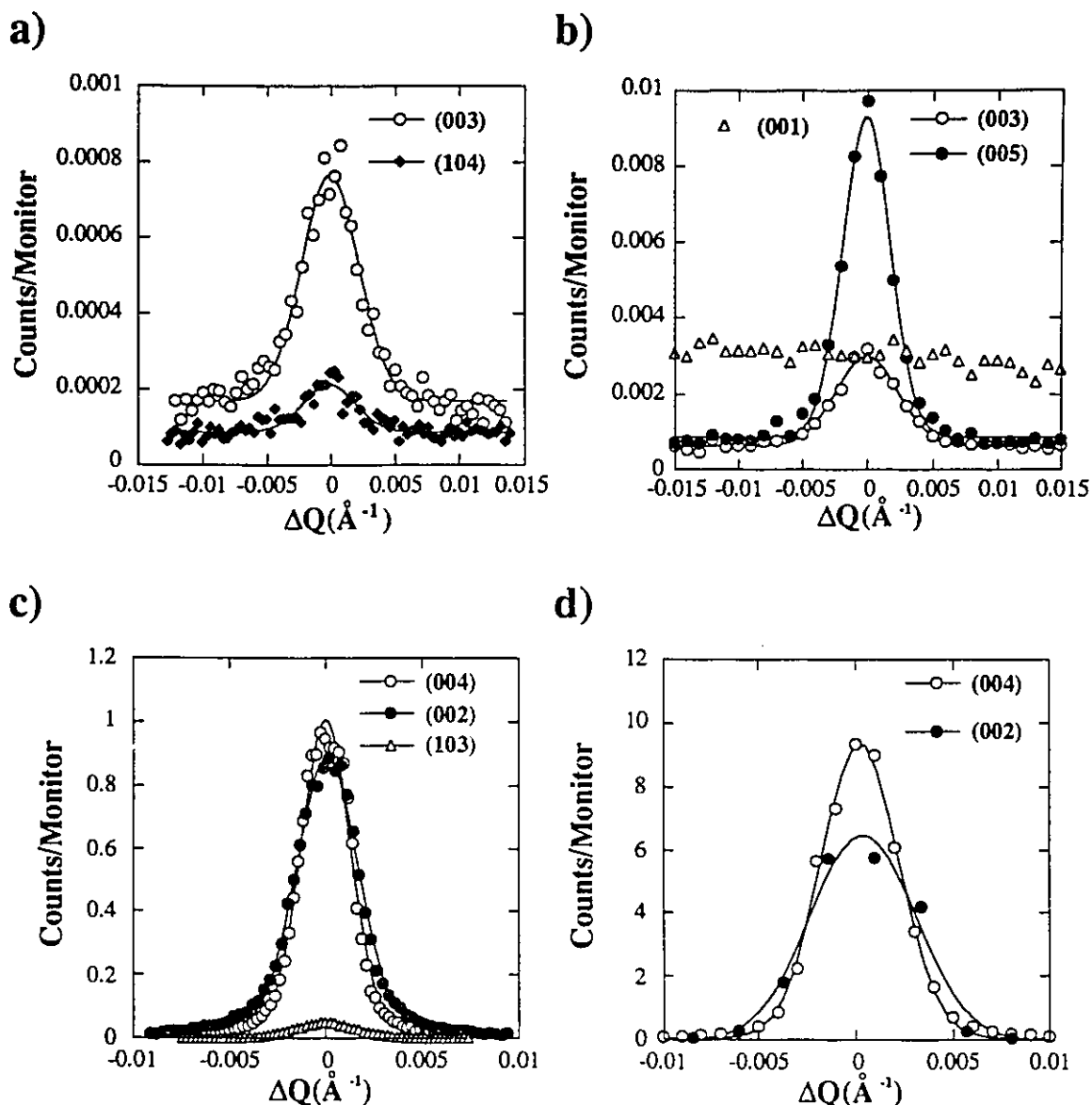


Figure 3-4: Raw radial scans through: a), b) the magnetic reflections and c), d) the charge reflections of URu_2Si_2 . Data a) and c) were taken in Aug. 92 while b) and d) were collected in Nov. 91[See Text]. Solid lines are the results of a gaussian fit. The charge reflections in c) and d) are uncorrected for attenuation due to Al-foils in the incident beam.

To estimate the integrated intensity at each reflection of Fig. 3-4, a normalized gaussian lineshape was fitted to the data points. This lineshape accounts for the change in width as function of the scattering wave-vector:

$$G(x) = A + \left(\frac{B}{D \cdot \sqrt{2\pi}} \right) \exp \left\{ -\frac{(x - C)^2}{2(D/2.354)^2} \right\} \quad (3.1)$$

where A is a constant background, B the integrated intensity, C the center and D the FWHM¹⁸. The fit results for the charge peaks and for the magnetic peaks are shown in Table 3-1 and Table 3-2 respectively.

(hkl) Charge 1992	$\int dI \times 10^{-3}$ Cts/Mon	$\int dI$ Ratio	FWHM (\AA^{-1})	(hkl) Charge 1991	$\int dI \times 10^{-3}$ Cts/Mon	$\int dI$ Ratio	FWHM (\AA^{-1})
(002)	8.08	1.1	0.00303	(002)	103.69	0.95	0.00634
(004)	7.47	1	0.00374	(004)	109.04	1	0.00466
(103)	0.45	0.06	0.00383				

Table 3-1: Integrated intensities and FWHM from a normalized gaussian lineshape of the 1991 and 1992 URu₂Si₂ charge peaks of Fig. 3-4. The intensity ratios have been normalized to (004).

(hkl) Magnetic 1992	$\int dI \times 10^{-6}$ Cts/Mon	$\int dI$ Ratio	FWHM (\AA^{-1})	(hkl) Magnetic 1991	$\int dI \times 10^{-5}$ Cts/Mon	$\int dI$ Ratio	FWHM (\AA^{-1})
(003)	7.85	1	0.00527	(001)	N.A.	< 0.3	N.A.
(104)	1.53	0.19	0.00480	(003)	3.36	1	0.00567
				(005)	9.03	2.7	0.00427

Table 3-2: Integrated intensity and FWHM from a normalized gaussian lineshape of the URu₂Si₂ magnetic Bragg peaks for the 1991 and 1992 dataset of Fig. 3-4. The (001) ratio was estimated from the scatter of the points [see text]. All the intensity ratios have been normalized to (003).

The charge peak intensities in Table 3-1 are still uncorrected for the attenuation used to prevent saturation of the detector. In 1992, two Al-foils were used while in 1991, only one was used. As no direct measurement of the effective attenuator thicknesses were performed, the standard "1-mil" per sheet is assumed:

¹⁸Bevington (1962).

$$\mu_{\text{Al}}/\rho_{\text{Al}} = 429.1 \text{ cm}^2/\text{g} \quad \rho_{\text{Al}} = 2.6941 \text{ g/cm}^3 \quad 1 \text{ mil} \equiv 2.54 \times 10^{-3} \text{ cm}$$

$$\mu_{\text{Al}} t = (\mu_{\text{Al}}/\rho_{\text{Al}}) \rho_{\text{Al}} t = 5.87 \text{ for 2-mils attenuation}$$

To correct for the Al attenuation, the Table 3-1 intensities need to be rescaled by: $I_0/I = e^{\mu_{\text{Al}} t} \cong 355.2$ for the 1992 experiment, and $I_0/I \cong 18.84$ for the 1991 experiment.

The result of this correction is shown in Table 3-3.

(hkl) Charge Corrected for Al-foils	1992 x 2 Al foils $\int dI \times 10^{-3}$ Cts/Mon	1991 x 1 Al foil $\int dI \times 10^{-3}$ Cts/Mon
(002)	2870	1953
(004)	2653	2054
(103)	160	-

Table 3-3: Integrated intensities of the 1991 and 1992 charge peaks (from Table 3-1) corrected for Al attenuation.

The charge peak intensities in Table 3-3 are found to agree within 40% ($I_{1992}^{(002)} = 1.38 \times I_{1991}^{(002)}$). This scaling factor could account for slight differences in the experimental set-up between the two experiments (such as variable air gaps, slits opening, etc.). However, when the same scaling factor is applied to the (003) magnetic reflection, $I_{1992}^{(003)} \times 5.91 = I_{1991}^{(003)}$ is found instead. Clearly the magnetic intensities do not scale with the same factor. The discrepancy may be due in part to the lack of precise knowledge of the Al-foil thickness of the attenuator used in each experiment at the charge reflections. In the following, we will normalize the intensities of the two experiments using the intensity at (003) as the reference.

It is worthwhile mentioning that our experiment also confirmed that the width of the magnetic peaks is not resolution limited, in agreement with previous reports on this compound [Isaacs *et al.* (1990) and Fig. 3-2 b)]. The correlation length along the c-axis, ξ_c , defined for a gaussian convolved with a gaussian gives:

$$\xi_c \propto \frac{1}{\sqrt{\Gamma_{Mag}^2 - \Gamma_{Res}^2}} \approx 530 \text{ \AA} \quad (3.2)$$

when the width of 1991-(005) and 1991-(004) (acting here as the resolution) are compared. This value is similar to the one reported by Isaacs *et al.* (1990): $\xi_c = 450 \text{ \AA}$.

3.1.2) Calculated intensities

The calculated charge and magnetic intensities were modelled from Eq. (1.1) by:

$$I_{obs} = C L(2\theta) A(\delta) B(\mu) |S(Q)|^2 \quad (3.3)$$

where the several correction factors already introduced in chapter 1 and 2 are:

$L(2\theta)$, the Lorentz factor [see Eq. (1.2)]

$A(\delta)$ the asymmetric absorption correction with $\delta = \arctan(ha^*/lc^*)$. a^* and c^* are the lattice reciprocal wave-vectors for (h0l) reflections [see Fig. 2-7].

$B(\mu) \approx \frac{1}{2\mu}$ the absorption in the small absorption limit [see Eq. (2.6)].

$S(Q) = \sum_{\text{atoms}} e^{iQ \cdot r_i} f_i$ the structure factor with f_i already defined by Eq. (1.18).

and, C an arbitrary scaling factor that depends on the experimental conditions.

Taking now account of the geometry of the experiment shown in Fig. 2-3, we write the selection rules for each harmonics in $f_{E-dipole}^{res}$ [Eq. (1.19)] as (if we assume total linear polarization for the incident photon):

$$\begin{aligned} \alpha &= (\vec{\epsilon}_i \cdot \vec{\epsilon}_f) \xrightarrow{100\% \sigma-pol} 1 \\ \beta &= (\vec{\epsilon}_i \times \vec{\epsilon}_f) \cdot \hat{s} \xrightarrow{100\% \sigma-pol} \hat{k}_f \cdot \hat{s} = \cos(\zeta) \\ \gamma &= (\vec{\epsilon}_f \cdot \hat{z})(\vec{\epsilon}_i \cdot \hat{z}) \xrightarrow{100\% \sigma-pol} 0 \end{aligned} \quad (3.4)$$

In the latter part of Eq. (3.4), the angle ζ is the same as that already introduced in Fig. 3-3.

A) Magnetic reflections

The magnetic structure factor $S(Q) = 2i\beta F_1$ depends on two parameters: the oscillator strength F_1 and the geometrical factor β [see Eq. (1.19)]. The factor of 2 comes from the presence of two uranium atoms adding in phase within the magnetic unit cell. As shown in Appendix A, when the resonant state has a very short lifetime, the X-ray cross-section is sensitive to spin and orbital moments such that we can write $F_1 = s \tilde{F}$, with, s , a constant which we relate to the "moment size" and, \tilde{F} , the overlap integral [see Eq. (A.1)]. Using Eq. (3.3), the calculation for each magnetic reflection is presented in Table 3-4.

The level of agreement between the relative intensities observed experimentally [Table 3-2] and the calculated ones [Table 3-4] is remarkable considering that the analysis only contains the 1st harmonic of the electric-dipole X-ray cross-section, the Lorentz factor and the asymmetric absorption correction.

Calculated Magnetic Intensities	(001)	(003)	(005)	(104)
$Q/4\pi$	0.052	0.157	0.261	0.241
θ	10.01	31.42	60.32	53.49
$\beta = \hat{k}_r \cdot \hat{z}$	0.174	0.521	0.869	0.396
Magnetic $S(Q)$	0.35 (\tilde{F}_s)	1.04 (\tilde{F}_s)	1.74 (\tilde{F}_s)	0.79 (\tilde{F}_s)
$A(\delta)$	1	1	1	0.436
$B(\mu)$	$1/2\mu$	$1/2\mu$	$1/2\mu$	$1/2\mu$
$L(2\theta)$	2.9219	1.1239	1.1623	1.0456
Calculated Intensity	0.35 (\tilde{F}_s) ²	1.22 (\tilde{F}_s) ²	3.51 (\tilde{F}_s) ²	0.28 (\tilde{F}_s) ²
Calculated ratios	0.28	1	2.9	0.24
<i>Observed ratios</i>	<i><0.3</i>	<i>1</i>	<i>2.7</i>	<i>0.19</i>

Table 3-4: Calculated magnetic intensities of URu₂Si₂ at M_{IV}-edge using the 1st harmonic of the electric dipole cross-section. The observed ratios were taken from Table 3-2.

These measurements seem to confirm that the cross-section is not sensitive to a Q-dependent factor (like a magnetic form factor in neutron scattering) even at the M-edge. In fact, this physical property is expected for the dipolar term in the multipolar expansion and is verified when the spatial distribution of the inner shells is considered much smaller than the X-ray wavelength [Wasedo (1984)]. This leads to anomalous corrections with a very small Q-dependence [Warren (1990)]. Nevertheless, one can argue that if the neutron-like magnetic form factor is introduced in the Table 3-4 analysis, the relative intensity of (001), compared to say (003) or (005), would be enhanced to a level well above the sensitivity of the present measurement.

To conclude this section, it is worth mentioning that the study of magnetic reflections along the (00L)-direction is impossible by neutron scattering in URu₂Si₂. The magnetic neutron cross-section gives no intensity when the spin is along the Q-direction. The electric dipole X-ray cross-section allows a study of magnetic reflections along this line in reciprocal space. This shows the complementarity one can get using both scattering probes.

B) Charge reflections

We calculated the magnetic Bragg peak intensities in the *small reflected power limit*. This hypothesis was justified because of the small intensities at the magnetic reflections of URu₂Si₂ ($10^{-2} \mu_B$). With the charge peaks, the situation is different because the anomalous corrections become very large when diffraction is performed directly at resonance [see section 2.2.1]. The difference can be understood using the criterion established by Zachariasen (1945) [Eq. (2.10)] to identify the *reflected power limit*. This criterion depends on the effective size of the crystallites t_0 . Using the Scherrer equation, $\Gamma(2\theta) = 2\lambda \frac{[\ln 2 / \pi]^{1/2}}{t_0 \cos(\theta)}$ [Warren (1990)] as the particle broadening width of the Bragg peak, and using the value of $\Gamma \approx 0.004 \text{ \AA}^{-1}$ from Table 3-1, we get $t_0 \approx 2500 \text{ \AA}$ as the lower limit on the particle size of the mosaic.

Taking now $\lambda = 3.33 \text{ \AA}$ (M_{IV} -edge), $V = 163 \text{ \AA}^3$ (the volume of the unit cell of URu₂Si₂), and assuming $f = 0.1$ for the magnetic reflections we get $W = 10^{-3}$ which confirms, to a good approximation, that absorption effects were accurately considered in the *weak reflected power limit*. However, for charge reflections at resonance, f is large and $W \approx 1$ which correspond to an *intermediate reflected power condition*. For this case,

Zachariasen (1945) has shown that the reflected power is $P/P_0 = \tanh(W)$, and that some particle size effects could be observable for strong reflections. Because of the difficulty in applying accurate corrections in this case (see section 2.2.1), we begin the calculation in the *weak reflected power limit*.

The total scattering amplitude in URu_2Si_2 from the U, Ru and Si atoms is given by: $f^{\text{U}} = \rho_{\text{U}}(Q) + \Delta f'_{\text{U}} + i\Delta f''_{\text{U}}$, $f^{\text{Ru}} = \rho_{\text{Ru}}(Q) + \Delta f'_{\text{Ru}} + i\Delta f''_{\text{Ru}}$ and $f^{\text{Si}} = \rho_{\text{Si}}(Q) + \Delta f'_{\text{Si}} + i\Delta f''_{\text{Si}}$, where $\rho(Q)$ is the form factor, $\Delta f'$ and $\Delta f''$ are the dispersion correction evaluated at the M_{IV} -edge wavelength for each atoms. Most of the scattering amplitude parameters can be found in standard tables¹⁹ and by using Cromer-Lieberman's program²⁰ (for the anomalous corrections). The only unknown contribution is the uranium white line *at resonance*, $\Delta f''_{\text{U}}$ [see Fig. 1-3 and related discussion in text].

McWhan *et al.* (1990) proposed an analysis for charge peaks at resonance where the fluorescence is used to evaluate the absorption of the sample, and hence $\Delta f''_{\text{U}}$. This correspondence is based on the optical theorem which relates the total absorption coefficient, μ , to the imaginary part of the scattering amplitude $\Delta f''$ by:

$$\mu_{\text{Tot}} = (2r_0\lambda N) (\Delta f''_{\text{U}} + 2\Delta f''_{\text{Ru}} + 2\Delta f''_{\text{Si}}) \times 2$$

with $\lambda = 3.33\text{\AA}$, $r_0 = 2.82\text{fm}$, and N is the atom density in URu_2Si_2 : $N = 1/(162.96\text{\AA}^3) = 1.23 \times 10^{28}\text{m}^{-3}$.

¹⁹International Tables for X-ray Crystallography, Vol. III and in Warren (1990) p.369

²⁰see Chapter 1 for reference.

(μ/ρ)	Below edge 3700 eV	At edge 3728 eV	Above edge 3750 eV
U (cm ² /g)	1097	3200	1494.4
Ru (cm ² /g)	1316.4	1291.5	1272.4
Si (cm ² /g)	552.2	541	532.3
μ_{Tot} (cm ⁻¹)	11374.67	≈ 21500	13098.10
$\Delta f''_U$	22.954	69.19	31.691

Table 3-5: Evaluation of $\Delta f''_U$ at MIV-edge from the total absorption curve (μ_{Tot}) published by Isaacs *et al.* (1990) (obtained from a fluorescence measurement).

Table 3-5 describes in detail how $\Delta f''_U$ is extracted from the published fluorescence curve [Isaacs *et al.* (1990)]. The total absorption at each energy is calculated by:

$$\mu_{T\alpha} = \sum_{\substack{\text{Unit} \\ \text{Cell}}} \rho_i \left(\frac{\mu}{\rho} \right)_i$$

where ρ_i is the atomic density in the unit cell and $(\mu/\rho)_i$ the atomic absorption obtained by Cromer-Lieberman's program.

At edge, the total absorption coefficient is found when the uranium contribution is set to $(\mu/\rho)_U = 3200$ cm²/g. The corresponding $\Delta f''_U$ value at 3728 eV is found by scaling the $(\mu/\rho)_U$ curve by a constant factor. The result of this procedure gives $\Delta f''_U = 69.19$, a value similar to $\Delta f''_U = 67$ found in UAs by McWhan *et al.* (1990). The similarity between the two compounds could indicate that the neighbouring atoms weakly affect the polarizability of the uranium atoms in both materials.

The anomalous dispersion corrections for all of the atoms needed in the structure factor calculation are summarized in Table 3-6. Using these values and Eq. (3.3), the calculation of the charge peak intensity is presented in Table 3-7.

	U	Ru	Si
$\Delta f'$	-47	-3.371	0.357
$\Delta f''$	69.2	11.56	1.346

Table 3-6: Anomalous dispersion corrections $\Delta f'$ and $\Delta f''$ for U, Ru, and Si at the uranium M_{IV} -edge. The value for $\Delta f''_U$ was obtained from a fluorescence measurement.

Charge scattering Analysis $\Delta f''_U$ from fluorescence	(002)			(004)			(103)		
$Q/4\pi$	0.104			0.209			0.198		
θ	20.34			44.03			41.25		
Form factors	U	Ru	Si	U	Ru	Si	U	Ru	Si
$\rho(Q)$	89.90	40.76	12.16	76.50	34.98	10.17	76.90	35.40	9.67
Scattering amplitudes									
$\sum(f_0 + \Delta f')$	-63.8			143.4			88.2		
$\sum(\Delta f'')$	92.2			179			142		
$S(Q)$	112.1			229.4			167.2		
$A(\delta)$	1			1			0.085		
$B(\mu)$	$1/2\mu$			$1/2\mu$			$1/2\mu$		
$L(2\theta)$	1.534			1.001			1.009		
Calculated Intensity	19263.6			52698.4			2390.8		
Calculated ratios	0.366			1			0.045		
Observed Ratios	≈ 1			≈ 1			0.660		

Table 3-7: Calculated charge intensities of URu_2Si_2 using $\Delta f''_U$ from the fluorescence measurement. The observed ratios were taken from Table 3-1.

This analysis [Table 3-7] does not lead to the observed (002)/(004) ratio. If we first assume that the fluorescence measurement is the only parameter used so far, one possible explanation can come from the crystallography of URu_2Si_2 . The scattering from the four Ru atoms ($4 \times 44 r_0$) nearly equals the scattering of the two U atoms ($2 \times 92 r_0$) in the unit cell. At (002), the Ru layers and the U layers along the c-axis are *out of phase*, while at (004) the Ru layers are *in phase* with the U layers. Assuming the contribution from charge scattering only (without anomalous corrections), the intensity at (002) should be much smaller than the intensity at (004). The fact that the observed intensities at (002) and (004) are nearly equal could suggest that the scattering per unit cell is effectively dominated by U-atoms alone. The anomalous corrections for the uranium atom ($\Delta f''_{\text{U}}$) should then be much larger than previously found. In Table 3-8, instead of the value for $\Delta f''_{\text{U}}$ extracted from the fluorescence curve (as in Table 3-7), $\Delta f''_{\text{U}}$ was left as a parameter to fit the observed intensities. This procedure leads to a value of $\Delta f''_{\text{U}} \approx 230$, which is three times the previous one. The corresponding absorption coefficient would then become 60000 cm^{-1} for a penetration depth of $\approx 2000 \text{ \AA}$.

Charge Scattering Analysis $\Delta f''$ left as a parameter	(002)	(004)	(103)
Scattering amplitudes			
$\sum(\Delta f'')$	413.8	500.9	463.8
$S(Q)$	418.9	520.6	471.9
Calculated Intensity	134590.7	135587.3	9509.2
Calculated ratios	0.993	1	0.070
<i>Observed Ratios</i>	<i>≈ 1</i>	<i>≈ 1</i>	<i>0.060</i>

Table 3-8: Calculated charge intensities of URu_2Si_2 when $\Delta f''_{\text{U}}$ is left as a fitting parameter. The observed ratios were taken from Table 3-1.

The $\Delta f''_U$ value found in Table 3-8 is probably too large to explain alone the discrepancy found in Table 3-7. Extinction effects could therefore be important. In an attempt to evaluate the importance of such effects, we can return to the analysis presented in Table 3-7. At (0 0 4), using the thickness t_0 already introduced at the beginning of this section, $W_{(004)} > 2$, which may indicate that this reflection is already in the saturated regime [See Fig. 3-5]. At (0 0 2), $S(Q)=f \approx 100$ and a similar calculation leads to $W_{(002)} > 1$. It is not clear from Fig. 3-5 whether (0 0 2) is still in the "linear regime". Without a precise knowledge of the block size mosaic at the surface of the sample, corrections for extinctions and its importance are not trivial to estimate.

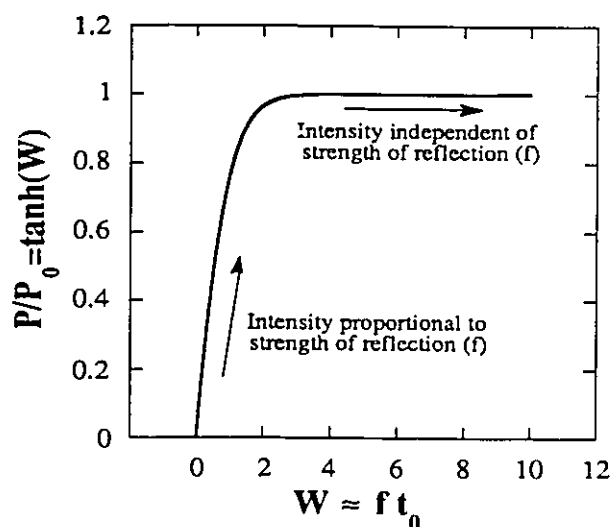


Figure 3-5: Integrated reflecting power as function of W [Adapted from Zachariasen (1945)].

3.1.3) Ordered moment size

The moment size is found, in principle, upon normalization of the charge intensities with the magnetic intensities. As we said in section 3.1.2 A), the magnetic intensities are proportional to \tilde{F} [see Eq. (A.1)] which can be evaluated using an atomic model.

McWhan *et al.* (1990) reported a value of $\tilde{F}=18.6r_0$ at the M_{IV} -edge and $8.3r_0$ at the M_V -edge in UAs.

For the charge peaks, two analyses were presented in section 3.1.3. With $\Delta f''_U=69.19$ (analysis based on a fluorescence curve), the average moment obtained from all the reflections (charge and magnetic) leads to $\tilde{s} \approx 0.02\mu_B$, and with $\Delta f''_U=230$, we obtain $\tilde{s} \approx 0.05\mu_B$. These results are in the range of the neutron scattering estimate ($0.04 \pm 0.01\mu_B$) from Broholm *et al.* (1991). There is however one question remaining: Can we really get a realistic estimate of the magnetic moment size by resonant X-ray scattering? The answer is not as straightforward as it may seem. There are many uncertainties linked to the procedure presented in sections 3.1.2 B) and C); the intensities of the charge reflections are affected by the Al-attenuator correction and possibly by extinction effects. Also, we used an atomic model value (F_1) to estimate the size of the magnetic scattering. On the other hand, we isolated the magnetic moment by writing $F_1 = s \tilde{F}$. This separation may be too crude to be realistic. Altogether, these factors clearly demonstrate that the evaluation of the moment size by resonant magnetic X-ray scattering is unreliable. It is interesting however to notice that the relative agreement between the neutron and the X-ray evaluation (within a factor 2) is similar to what has been found by Isaacs *et al.* (1990).

3.2) Magnetic Structure and Phases of UPd_2Al_3 and UNi_2Al_3

The two UT_2Al_3 ($T=\text{Ni, Pd}$) compounds discovered by Geibel, Thies *et al.* (1991) and Geibel, Schank *et al.* (1991) display the same crystal structure and belong to the same $P6/mmm$ space group [Fig. 3-6]. The lattice constants for the Ni-compound are $a=b=4.018\text{\AA}$ and $c=5.207\text{\AA}$ and for the Pd-compound $a=b=4.186\text{\AA}$ and $c=5.365\text{\AA}$. Early studies by the same authors found that both materials exhibit antiferromagnetic order and superconductivity at low temperature ($T_N=4.6\text{K}$ and $T_c=1.2\text{K}$ for the Ni-compound and $T_N=14\text{K}$ and $T_c=2\text{K}$ for the Pd-compound). The magnetic moments are presumably localized on the uranium atoms which form a simple hexagonal lattice.

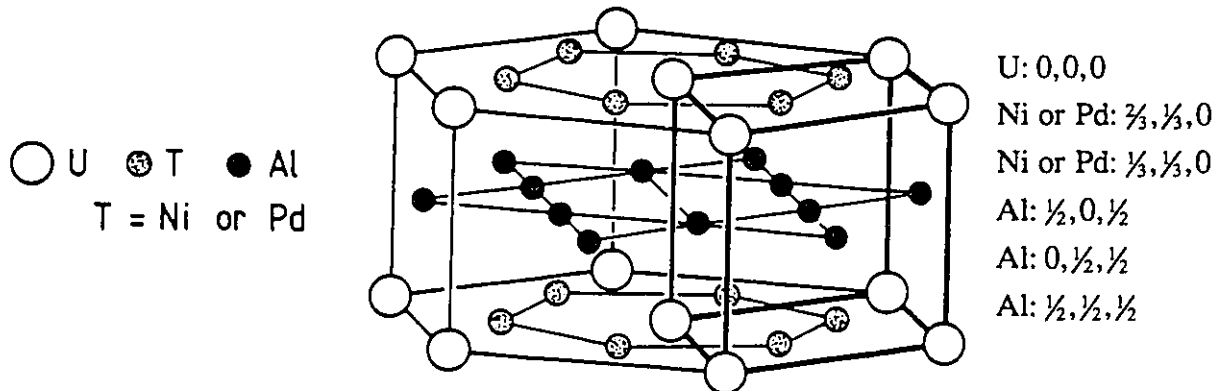


Figure 3-6: Crystal structure of UT_2Al_3 ($T=\text{Ni, Pd}$) materials [Sticht *et al.* (1992)]. The atomic positions in the unit cell are given in a, b and c units.

Powder neutron measurements could identify the ordering wave-vector in the Pd-compound but failed to reveal any evidence of magnetic order in the Ni-compound [Krimmel *et al.* (1992)]. The moment size found in the Pd-compound ($0.85\mu_B$) is of conventional size, which is remarkable for a magnetic superconductor. The moment estimated from the powder measurement in the Ni-compound ($<0.1\mu_B$), is modest but

nevertheless large when compared with UPt_3 or URu_2Si_2 . In this section, we present several experiments performed on single crystals to further investigate the magnetic structure and phases of both compounds.

3.2.1) UPd_2Al_3

A) Spin orientation in the basal plane

Neutron diffraction measurements below 14K show that UPd_2Al_3 has an antiferromagnetic phase [Krimmel *et al.* (1992)]. The superlattice reflections (i.e. (0 0 1/2)) observed below this temperature indicate that the magnetic order is ferromagnetic within the basal plane and antiferromagnetic along the c-axis. The wave-vector, however, does not give any information about the orientation of the spins in the structure. To find the spin direction, other measurements are required.

Anisotropy between the c-axis and the basal-plane magnetizations by Grauel *et al.* (1992) implied that the spins preferably lay in the hexagonal basal plane. Some additional evidence from resistivity measurements [de Visser *et al.* (1994)] and neutron scattering studies [Kita *et al.* (1994) and Paolasini *et al.* (1994)] suggests that the spins would point along the a-axis [Fig. 3-7].

Using the magnetic term (1st harmonic) of the resonant X-ray cross-section, we performed an experiment at the NSLS X-14 beamline to determine the basal plane orientation of the spins in UPd_2Al_3 . The annealed polycrystal sample (for 3 days under ultrahigh vacuum) had crystallites extending over a few photon penetration depths below the surface. It was believed that such crystallites could give single crystal properties.

Characterization on another sample coming from the same boule gave a residual resistivity of $\rho_0=2.2\mu\Omega\text{-cm}$. It was superconducting below $T_c=2.0\text{K}$ and the transition had a transition width of 0.04K , which suggests a superconducting sample of high quality.

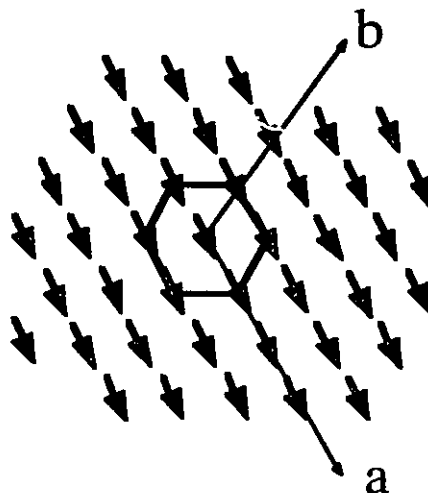


Figure 3-7: Magnetic order in the basal-plane of UPd_2Al_3 with the spins pointing along the a-axis. The c-axis is perpendicular to the page.

The single-crystallite chosen for the experiment had its c-axis perpendicular to the surface and this allowed us the freedom to rotate the crystallite in the plane perpendicular to the scattering wave-vector Q , a configuration known as a four-circle Ψ -rotation [see Fig 3-8].

To avoid any change in absorption as Ψ is varied, the displac was mounted with a Be-dome offering a constant thickness to the incoming and scattered beams. All the measurements were performed at the displac base temperature $\approx 10\text{K}$ with an incident energy corresponding to the uranium M_{IV} -edge to enhance the magnetic intensity.

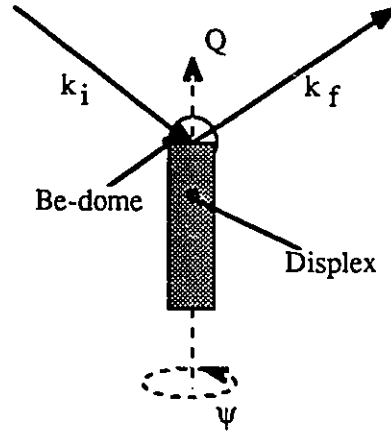


Figure 3-8: Ψ -rotation in a four-circle spectrometer. The Ψ -rotation axis is the scattering wave-vector Q .

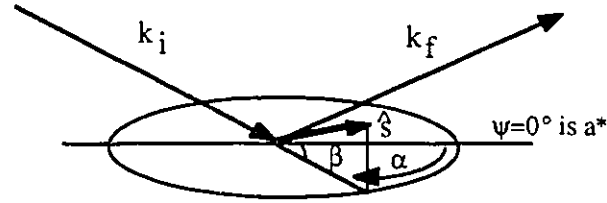


Figure 3-9: Definition of the angles α and β describing the spin orientation (\hat{s}) during the Ψ -rotation.

It is important to stress that the ferromagnetic basal-plane spin arrangement in UPd_2Al_3 , shown in Fig. 3-7, gives three equivalent domain directions each pointing at 120° from each other. In the case where the three domains are equally populated, the sum of the three domain intensities would give no Ψ -dependence. However, the single-crystallites at the surface of the polycrystalline boule could favor the growth of one domain compared to the others. In the following, we assume the single crystallite under investigation to be a single domain.

For $h=0$ or $(0\ 0\ 1)$ -reflections, the absorption of the sample does not change as a function Ψ since the surface of the crystallite is perpendicular to the c -axis. However, that is not the case for $(0\ h\ 1)$ -reflections because of the tilted basal plane (angle σ). In the latter case, the asymmetric absorption correction already presented in Eq. (2.3) is modified using the angles defined in Fig. 3-10:

$$\tan \delta = \frac{h}{l} \qquad \tan \delta' = \frac{h}{L} \qquad \cos \Psi = \frac{l}{L}$$

therefore,

$$\cos \Psi \tan \delta = \tan \delta', \quad \delta'(\Psi) = \arctan(\cos(\Psi) \tan(\delta))$$

and,

$$I_{\text{obs}} = \frac{I_0}{\frac{1}{2} \left(1 + \frac{\sin(\theta + \delta'(\Psi))}{\sin(\theta - \delta'(\Psi))} \right)}$$

The small size of the crystallite makes the alignment of the sample a constant preoccupation. It is difficult to be sure, for example, that the sample is constantly exposed to the incident beam during the rotation. To monitor the effect of such misalignments, a Ψ -rotation was performed at the $(0\ 0\ 2)$ charge reflection where no Ψ dependence is expected. The intensity of the reflection was estimated by integrating the Ω -rocks (sample rotation) taken at each Ψ position. As shown in Fig. 3-11 a), the λ -channel intensity has some Ψ -dependence which matches the variation in the λ/N -channel intensity. The similarity between the two channels suggests that the sample is not exactly at the center of rotation of the goniometer. When renormalized in Fig. 3-11 b), the $\lambda/(\lambda/N)$ ratio shows that the λ/N -channel gives a good account of the incident flux impinging on the sample.

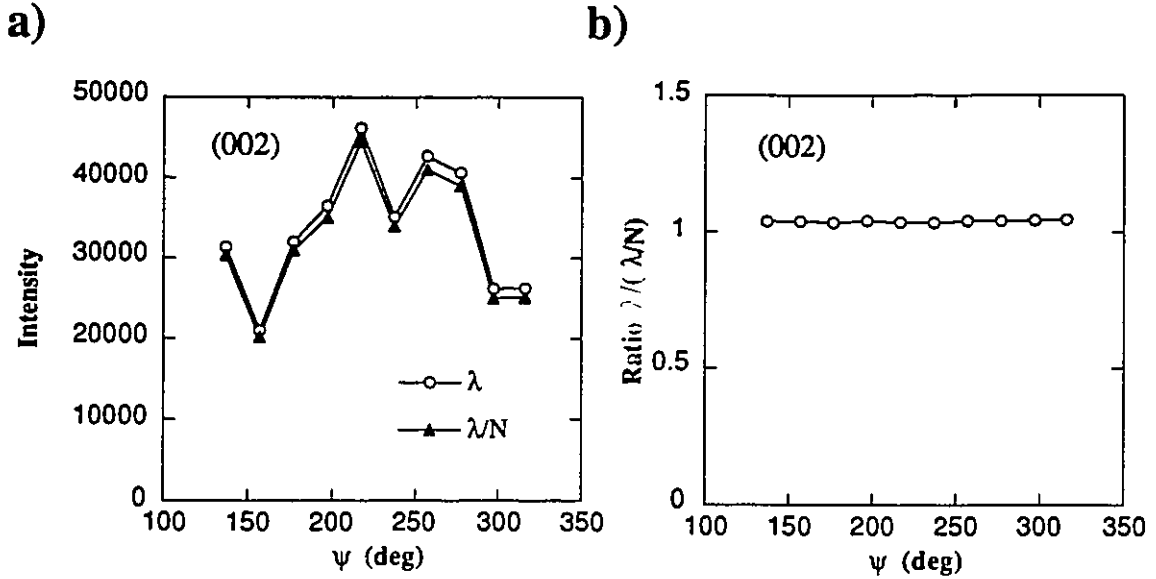


Figure 3-11: Ψ -rock at (002) charge reflection: a) the raw data, and b) the $\lambda/(\lambda/N)$ ratio. The λ/N channel is used as an *ad hoc* monitor renormalization.

The same flux normalization procedure was applied at the magnetic reflections. Two approaches were used to find the spin direction (angle α) in the basal plane. The first method, using the data collected at (0 0 3/2), consists in taking the difference between the low and high temperature data set (below and above T_N) to isolate the magnetic part [Fig. 3-12]. The data at (0 1 3/2) [Fig. 3-13] was analysed using only a correction for asymmetric absorption [see Fig. 3-10].

Measurements at both wave-vectors give a fit value for $\beta < 3^\circ$ which suggests that the spins are indeed in the basal plane. The values of $\alpha = 80 \pm 4^\circ$ at (0 0 3/2) and $\alpha = 161 \pm 5^\circ$ at (0 1 3/2) obtained from this fit are better understood if we make reference with the equivalent directions within the hexagonal basal-plane [Fig. 3-14]. Keeping in mind that $\Psi = 0^\circ$ is along a^* [see Fig. 3-9], both experiments suggest that the spins are not pointing along the a^* direction.

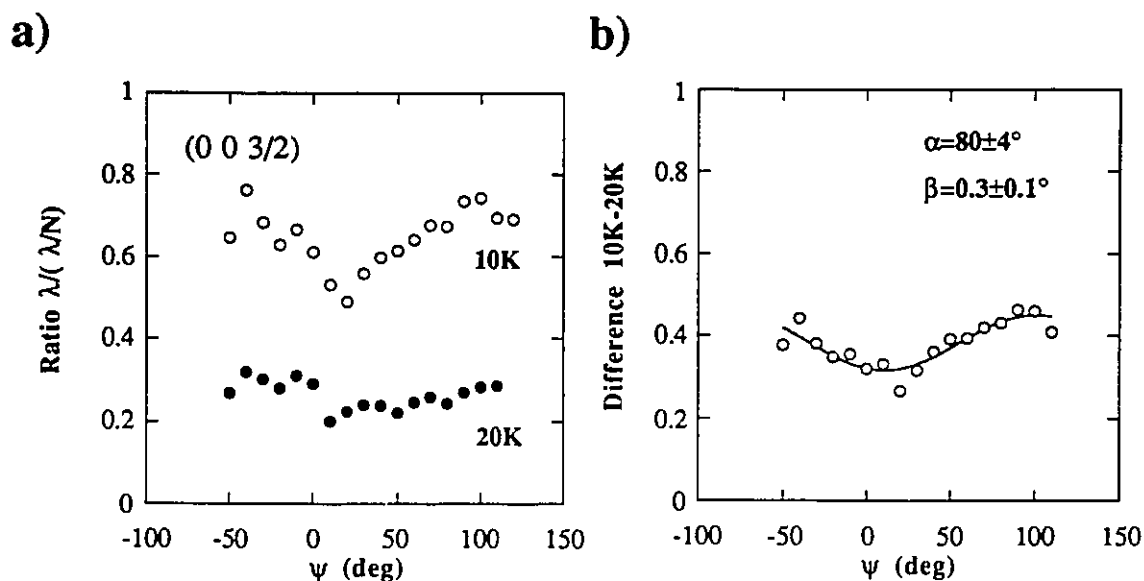


Figure 3-12: Ψ -rock at $(003/2)$. a) shows the Ψ -rocks at 10K and 20K and b) shows the difference between the 2 scans. The continuous line is a fit using the expression for $\hat{k}_f \cdot \hat{s}$ described in the text.

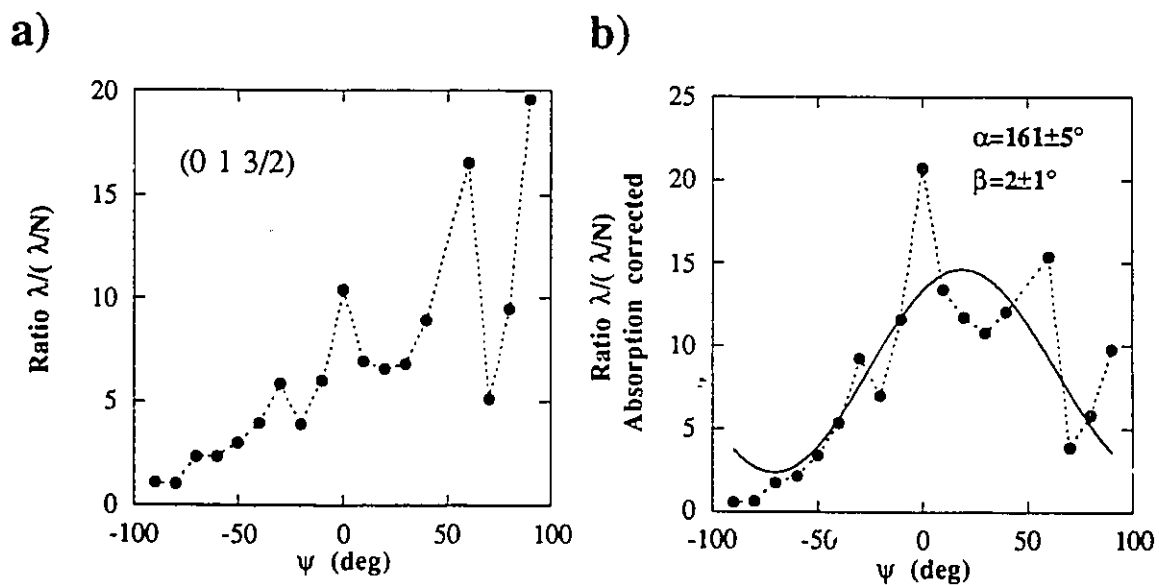


Figure 3-13: Ψ -rock at $(013/2)$. a) shows the $\lambda/(\lambda/N)$ ratio of the raw data while b) is the same data set corrected for asymmetric absorption. The continuous line is the result of the fit using the expression for $\hat{k}_f \cdot \hat{s}$ described in the text.

When compared to the a -axis direction, both experiments give very similar offsets: $\Delta = 10 \pm 4^\circ$ at $(003/2)$ and $\Delta = 11 \pm 5^\circ$ at $(013/2)$ [Fig. 3-14]. However, the accuracy of our measurement makes it difficult to establish whether the spins point preferentially along the a -axis or along the mid-direction between the a -axis and the a^* -axis ($\Delta = 15^\circ$). It is worth mentioning that the temperature of the measurement ($\approx 10\text{K}$) is just below an anomaly observed at $\approx 12\text{K}$ with this sample (see next section). The observed spin direction may therefore be different from the low temperature phase.

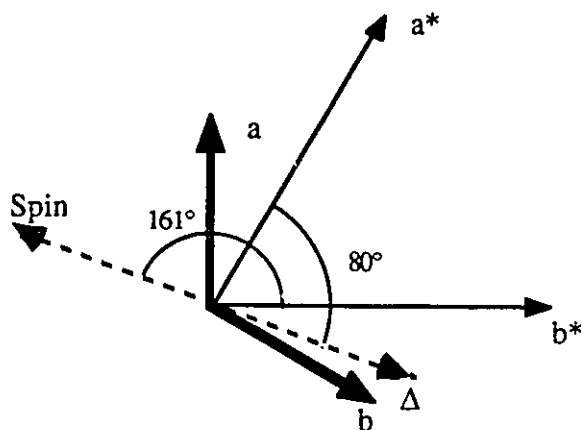


Figure 3-14: Spin orientation in the hexagonal basal plane of UPd_2Al_3 from the Ψ -rotation experiment at 10K . The angle Δ is the offset from the basal-plane axis of the unit cell (both a and b -axes are equivalent). The measurements performed at $(0\ 0\ 3/2)$ and $(0\ 1\ 3/2)$ give the same overall direction $\Delta \approx 10^\circ$.

B) Magnetic Phases and Order Parameter [Gaulin *et al.* (1994)]

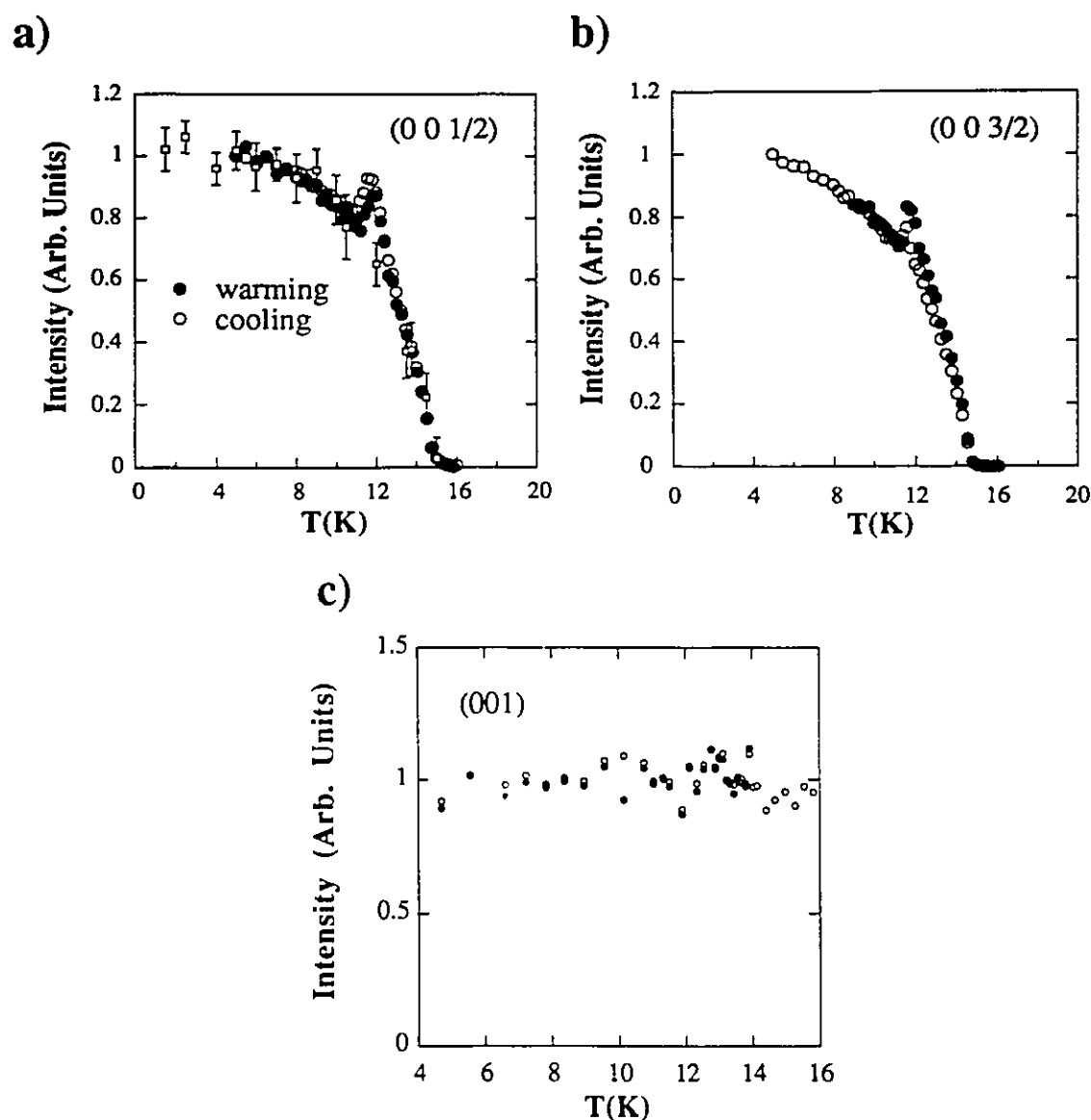


Figure 3-15: Order parameters at the a) $(0\ 0\ 1/2)$ and b) $(0\ 0\ 3/2)$ magnetic reflections of UPd_2Al_3 . The white squares in a) are the results of a neutron powder experiment performed on a sample coming from the same boule as the polycrystal. In c) the intensity of the $(0\ 0\ 1)$ charge reflection is plotted vs. temperature.

The temperature dependence of the magnetic intensity at both $(0\ 0\ 1/2)$ and $(0\ 0\ 3/2)$ magnetic wavevectors was obtained on the same UPd_2Al_3 polycrystal sample (not necessarily the same crystallite) previously described. The resonant X-ray experiment was carried out at the NSLS X22c beamline using a two stage dispex that could reach a minimum temperature of $\approx 4\text{K}$ (above $T_c=2\text{K}$). The incident energy was set at the uranium M_{IV} -edge to enhance the magnetic signal.

At low temperature the width of radial scans at the magnetic peaks was found to be resolution limited indicating that the magnetic order is truly long range in contrast with UPt_3 or URu_2Si_2 [Gaulin *et al.* (1994)].

The intensity of each magnetic reflection as a function of temperature (on warming and cooling) is plotted in Fig. 3-15 a) and b). The magnetic order parameters²² were obtained with a relatively large slit setting on the scattered side to get a maximum intensity in the Ω -rocks performed at each temperature. The critical exponent extracted from both curves gives $\beta = 0.31 \pm 0.05$ (reduced temperature $t > 10^{-3}$ and $T_N = 14.8 \pm 0.2\text{K}$), a value in good agreement with the one reported by Paolasini *et al.* (1994): $\beta = 0.33 \pm 0.02$. This β -value falls into the range of typical 3-dimensional critical behaviour [Collins (1989)].

The remarkable feature in the order parameters at $(0\ 0\ 1/2)$ and at $(0\ 0\ 3/2)$ is the presence of a large anomaly near 12K [Fig. 3-15 a) and b)]. As a comparison, Ω -rocks at the (001) charge reflection gave a relatively flat dependence upon changing the temperature [Fig. 3-15 c)].

²²Intensity of the magnetic reflection vs. temperature. Generally, the intensity is proportional to the magnetization squared (or staggered magnetization in an antiferromagnet). In resonant magnetic X-ray scattering, the connection to the magnetization is not straightforward.

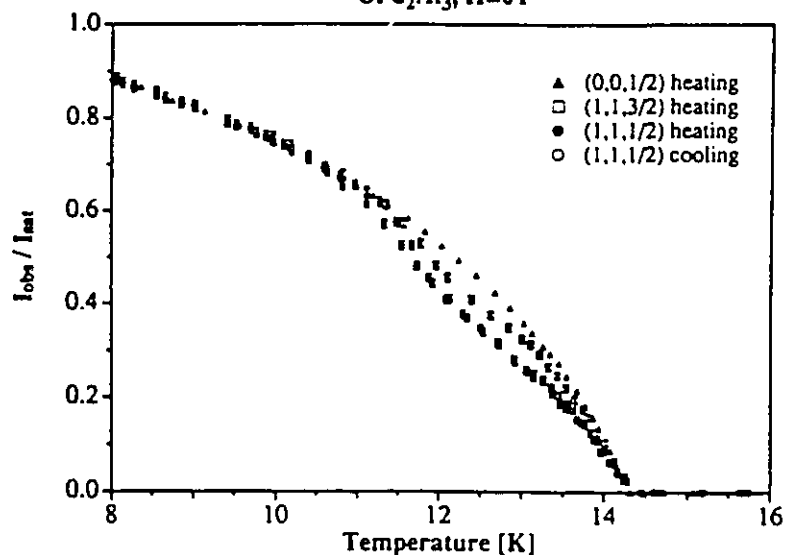


Figure 3-16: 12K-anomaly found by neutron scattering in 0 Tesla [from Kita *et al.* (1994)].

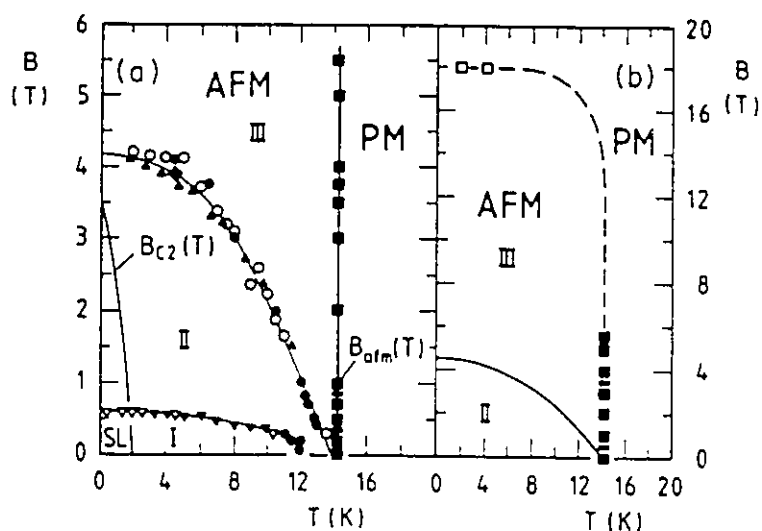


Figure 3-17: Magnetization and phase diagram of UPd₂Al₃ [Grauel *et al.* (1992)].

This 12K-anomaly was also observed in a neutron scattering study published by Kita *et al.* (1994) [Fig. 3-16]. In this measurement, an intensity decrease was observed at several wave-vectors except at (0 0 1/2) which indicates that the anomaly could be associated with a spin rotation within the basal plane²³. This explanation is qualitatively compatible

²³The neutron scattering cross-section is not sensitive to a variation of the spin component *within* the plane perpendicular to Q .

with the anomaly in the X-ray results [Fig. 3-15] but since the basal plane orientation of the X-ray sample was unknown, a more quantitative evaluation is not possible.

The magnetic phase diagram of UPd_2Al_3 already contained some indications about the presence of an anomaly near 12K. Grauel *et al.* (1992) identified three magnetic phases in UPd_2Al_3 labeled I, II and III [Fig. 3-17] where the 12K-anomaly corresponds to the crossing of the I-II phase boundary in zero-field. It seems likely, from Kita *et al.* (1994) and our X-ray result, that the transition giving rise to this 12K-anomaly in zero field corresponds to a spin rotation in the basal plane. Its origin and characteristics however remain unknown. In a recent neutron scattering study, Paolasini *et al.* (1994) argued, using a magnetic field applied along different directions of the basal plane, that the 12K-anomaly is due to domain reorganization and not to a new magnetic phase in UPd_2Al_3 .

3.2.2) UNi₂Al₃

A) Magnetic Order in Zero Field [Schröder *et al.* (1993)]

Although there were strong indications from specific heat and magnetization measurements that UNi₂Al₃ underwent a magnetic phase transition at $T_N=4.6\text{K}$ [Geibel *et al.* (1991)], its magnetic order could not be found by neutron powder experiments [Krimmel *et al.* (1992)]. The lack of sensitivity of neutron powder diffraction experiments can be understood by the small magnetic moment in UNi₂Al₃ ($\approx 0.1\mu_B$) and the presence of a large incoherent background due to the Ni. A neutron powder experiment performed at the C2 Dualspec spectrometer at AECL Laboratories (Chalk River) reached the same conclusion. The pumpable ⁴He cryostat used in this experiment could cool the sample to 2K, which is below the magnetic transition ($T_N=4.6\text{K}$) but above the superconducting phase ($T_c\approx 1\text{K}$). The powder pattern obtained [Fig. 3-18] did not reveal any temperature dependent signal that could be interpreted as a signature of magnetism.

To observe the long range magnetic order, a systematic search in reciprocal space using a single crystal is necessary. The single crystal was grown by a tri-arc Czochralski technique and special care was taken to assure a single growth by creating successive "necks" over nearly 2 cm before expanding the crystal horizontally. No initial seeds were used (except the tungsten tip) and the startup melt was made according to the stoichiometric fractions of each element. The final cylindrical sample, of about 1cm³ in volume, was annealed at 900°C for a week under Ar-gas. This procedure could have

minimized Al evaporation²⁴. At the spectrometer, the single crystal was found to be made of three large grains each of them having a mosaic spread of $\approx 1^\circ$. The nuclear intensities were found to agree well with the proposed crystal structure [Fig. 3-19].

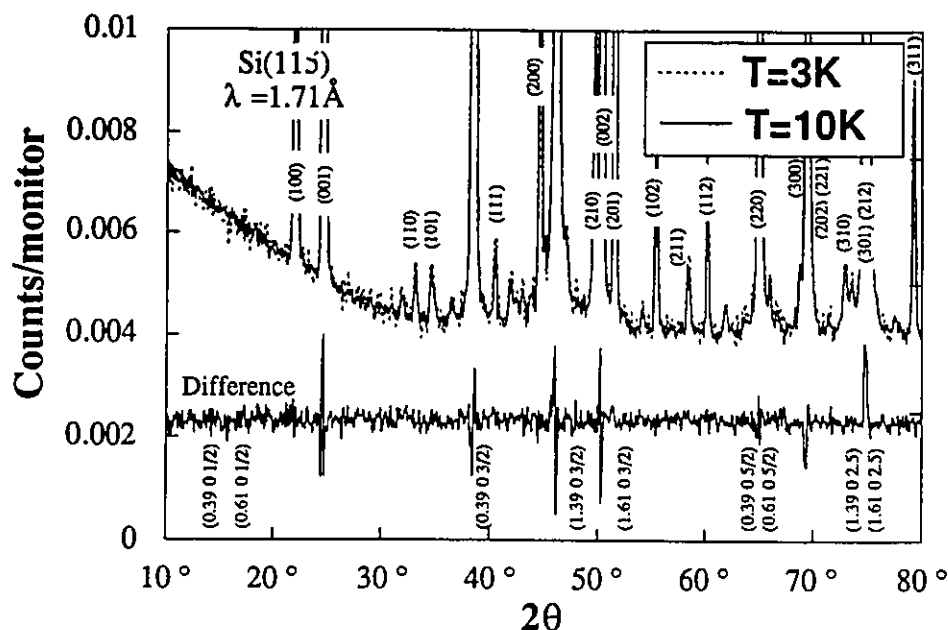


Figure 3-18: Powder pattern of UNi_2Al_3 obtained by neutron scattering. None of the later found magnetic Bragg peaks (indicated on the figure) appear in the difference because of the large incoherent background from Ni and the small ordered moment.

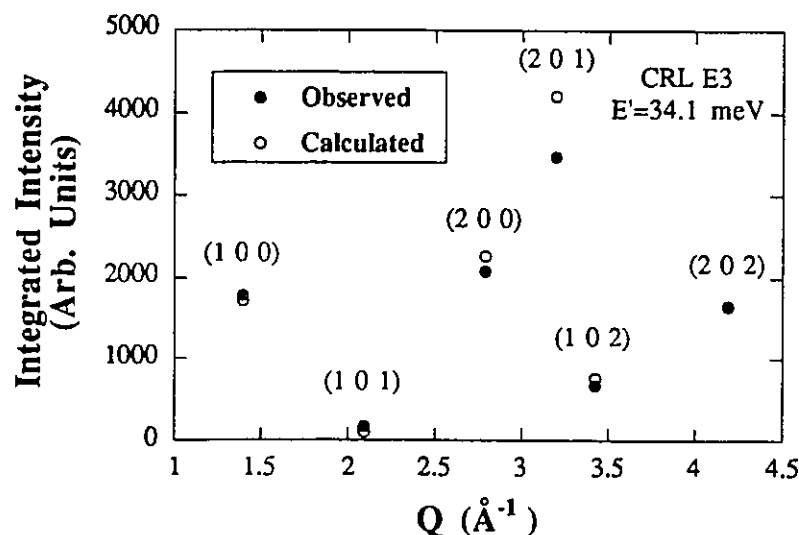


Figure 3-19: Observed nuclear Bragg peak intensities from the UNi_2Al_3 single crystal sample. The calculation was performed using the proposed structure in Fig. 3-6.

²⁴The final Al concentration is important with this class of material.

Using a neutron wavelength that matched the second graphite filter window (1.55Å), initial scans along high symmetry directions in the (h h l) and in the (h k 0) scattering planes did not reveal any temperature dependent signal. This particular choice of wavelength was used to limit the contribution of high energy neutrons and to give a coarse resolution.

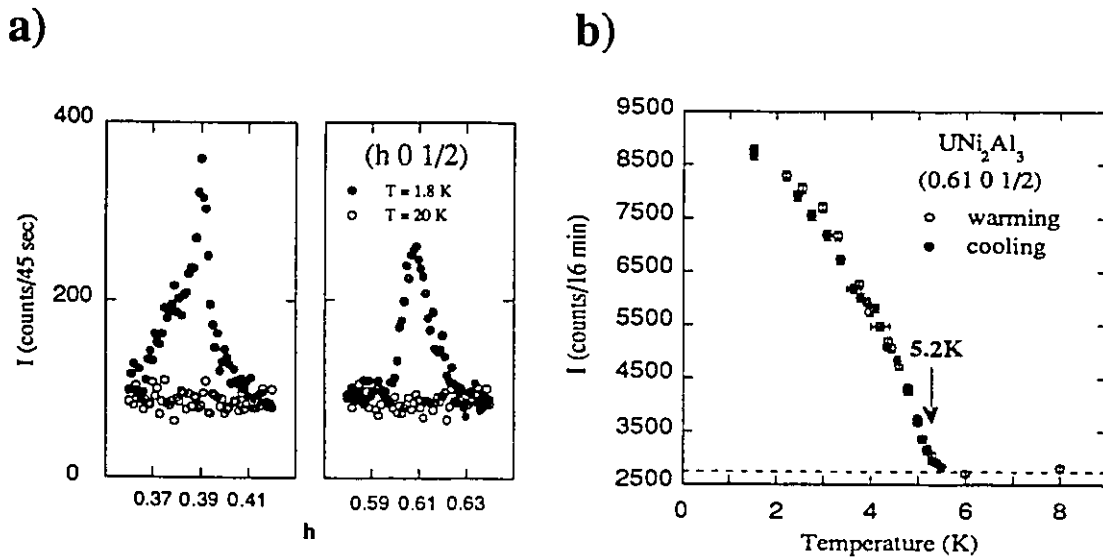


Figure 3-20: a) Observation of magnetic order in UNi_2Al_3 after comparison of low and high temperature data. The asymmetric shape of $(0.39 \ 0 \ 1/2)$ satellite is due to mosaic. b) Magnetic order parameter made from peak heights vs. temperature at $(0.61 \ 0 \ 1/2)$ [from Schröder *et al.* (1993)].

Magnetic Bragg peaks appeared in the $(h \ 0 \ l)$ -plane at $(1/2 \pm \tau \ 0 \ 1/2)$ with $\tau = 0.110 \pm 0.003$, as shown in Fig. 3-20 a). The magnetic satellites, observed near the $(1/2 \ 0 \ 1/2)$ position, are the signature of incommensurate magnetic order with a period of about 18 atoms in the basal plane. Along the c -axis, the basal plane pattern is rotated by 180° from one plane to the next.

Radial scans performed at low temperature show the magnetic order to be of long range in contrast with the limited correlation lengths found in UPt_3 and URu_2Si_2 [see Fig. 3-1 and 3-2]. The temperature dependence of the order parameter squared, described by the function $\approx (T-T_N)^{0.6}$ in Fig. 3-20 b), also differs from linear temperature dependence found in these two compounds. The sample had a $T_N \approx 5.2\text{K}^{25}$ and an estimate of the critical exponent gives $\beta = 0.33 \pm 0.06$ which is in the range of typical 3D models [Collins (1989)].

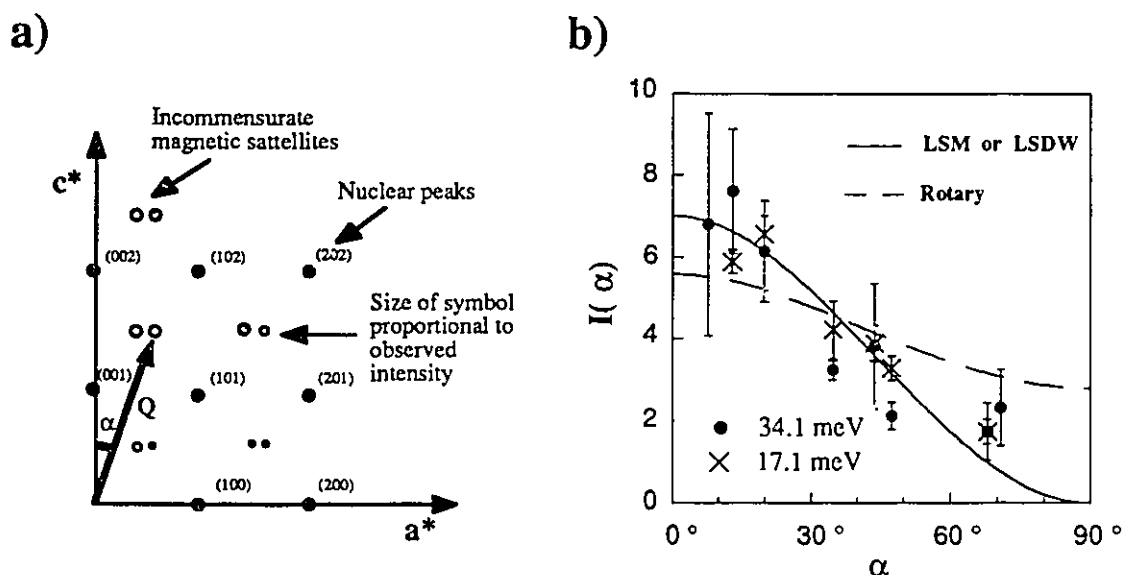


Figure 3-21: Intensity pattern in the $(h0l)$ -plane of UNi_2Al_3 . In a), intensity of several incommensurate magnetic satellites. In b), the intensities are plotted as a function of the angle α defined in a). The continuous and dashed lines, in b), are the α -dependence of models further explained in the text.

A survey of magnetic satellites in the $(h\ 0\ l)$ -plane gave further information about the ordering. The high intensity obtained for the Bragg peaks close to the c^* -direction, in Fig. 3-21 a), suggests that the spins are lying mostly within the basal plane. As explained before, this comes from the fact that neutron cross-section is sensitive to the spin

²⁵The calibration for this experiment may have been defective. Other measurements give $T_N=4.6\text{K}$ for this sample.

component perpendicular to Q . Fig. 3-21 b) shows the intensities of the magnetic satellites (after correction for the form factor and the Lorentz factor), $I(\alpha)$, as function of the angle α (the orientation of the scattering vector Q in the $(h0l)$ plane) [see Fig. 3-21 a)]. In Fig. 3-21 b), data using two different energies have been used: at 8.23 THz (34.1 meV) the intensities were obtained from the integration of radial scans while at 4.12 THz (17.1 meV) peak heights were taken. The continuous and dashed lines in Fig. 3-21 b) correspond to two simple models used to compare the observed intensities. These two models are shown in Fig. 3-22 a) and b). Full characterization of the magnetic structure in UNi_2Al_3 requires group-theoretical methods.

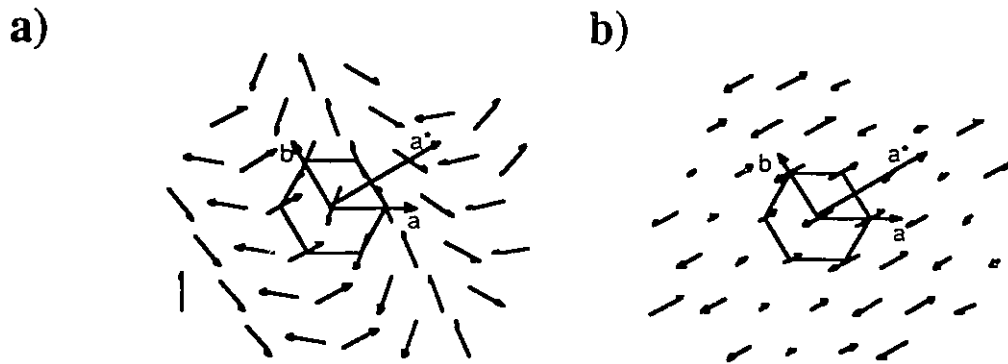


Figure 3-22: Two possible spin structures in the hexagonal basal plane of UNi_2Al_3 used to generate the curves in Fig. 3-21 b). a) is the Rotating Spin model (Rotary) and b) is the Longitudinal Spin Modulated model (LSM). The latter model is shown with an a^* polarization. Both pictures show only one of the possible three domains.

The origin of the α -dependence for each model can be understood if the spins (confined to rotate in the basal plane) and the wave-vector Q (confined to rotate in the $(h\ 0\ l)$ -plane) are defined as (in cartesian coordinates):

$$\hat{s} = (\cos \delta, \sin \delta, 0) \quad \hat{Q} = (\sin \alpha, 0, \cos \alpha) \quad (3.6)$$

The neutron scattering amplitude therefore becomes :

$$\hat{Q} \times (\hat{s} \times \hat{Q}) = \hat{x}(\cos^2 \alpha \cos \delta) + \hat{y}(\sin \delta) + \hat{z}(\sin \alpha \cos \alpha \cos \delta) \quad (3.7)$$

In the rotating spin model (rotary), the spins are rigidly rotated (no change in length) by $\Delta\delta \approx 140^\circ$ from one site to the next. After the magnetic atoms are summed in phase within the unit cell, the average over δ can be taken to 1 and the intensity is written as:

$$I_{\text{Rotary}} \propto (\cos^2 \alpha)^2 + (1)^2 + (\sin \alpha \cos \alpha)^2 \quad (3.8)$$

The curve in Fig. 3-21 b) shows that this model, once scaled, does not offer a good description of the anisotropy seen in the experimental data.

In the spin modulated (SM) model the spins are fixed in a given direction δ_0 but are modulated in size from one site to the next. This is equivalent to a reduction of the Rotary model to only one of its sine or cosine component. The α -dependence that reproduces best the Fig. 3-21 b) data is obtained when $\delta_0=0^\circ$ (along a^*). This structure where the modulation is along the propagation vector is called Longitudinal Spin Modulation (LSM):

$$I_{\text{LSM}} \propto (\cos^2 \alpha \cos \delta_0)^2 + (\sin \delta_0)^2 + (\sin \alpha \cos \alpha \cos \delta_0)^2 \xrightarrow{\delta_0=0^\circ} (\cos^2 \alpha)^2 + (\sin \alpha \cos \alpha)^2 \quad (3.9)$$

From this set of arguments, the magnetic order in UNi_2Al_3 is found to be best represented by the LSM model with an a^* -polarization ($\delta_0=0^\circ$). This model gives a maximum ordered moment of $0.24\mu_B \pm 0.1$ [Schröder *et al.* (1993)] or $0.16\mu_B/\text{U-at}$ on average

assuming that only one of the three equally populated single-q domains contributes to the intensity²⁶.

Multiple-q structures are also possible in UNi_2Al_3 . The distinction between single-q and multiple-q structures can be made by measuring all the domain directions simultaneously while an external force (a magnetic field or pressure) acts on the sample [Rossat-Mignod *et al.* (1987)]. The spectrometer used in our experiment did not have this feature and we have to relay on indirect methods, such as lattice distortions, to distinguish between the two possibilities.

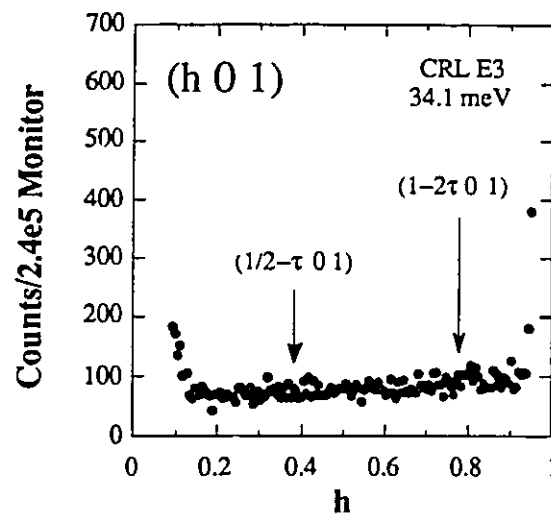


Figure 3-23: Part of a long scan between (001) and (101) in UNi_2Al_3 at 2K used in the initial search for magnetic reflections. The scan has a low counting statistics.

Landau theory calculations²⁷ on UNi_2Al_3 predict that single-q and triple-q structures would give supplementary reflections at $(1-2\tau, 0, 0)$, while triple-q alone would give extra reflections at $(1/2-\tau, 0, 0)$. Fig. 3-23 shows a scan near the (101) Bragg peak where none

²⁶The three domains come from the three equivalent directions in the hexagonal basal plane: a^* , b^* and (a^*-b^*) .

²⁷M. Walker private communication.

of the expected extra peaks were observed. The sensitivity of the measurement was, however, relatively poor because of the large background. The signature of a double-q structure, known as broadening of symmetry, would push the magnetic peaks off the high symmetry axis. This was not found to occur in UNi_2Al_3 .

It is also important to discuss some important consequences associated with the stability of SM structures at low temperature. Elliott (1961) has shown that SM structures are not thermodynamically stable and eventually take on a square wave profile as $T \rightarrow 0$ (the magnetic moments become equal in size). A good example for this behaviour is observed in the longitudinal SM phase of Er [Lin *et al.* (1992), McMorrow *et al.* (1992)]. As the temperature is lowered from the longitudinal phase, the incommensurate wave-vector migrates towards several commensurate structures ("lock-in") which indicate the formation of Equal Moment (EM) structures [Lin *et al.* (1992)]. Such squaring-up process eventually gives extra Fourier components (at $3Q$ and at $5Q$ for example) much weaker in intensity than the fundamental. In UNi_2Al_3 , the observation of these extra Fourier components requires special care because of the small moment size and the large incoherent background from the Ni. Nevertheless, as shown by a precise X-ray measurement in Fig. 3-35, the ordering wave-vector in UNi_2Al_3 seems to remain incommensurate to the lowest temperatures which suggest the presence of a mechanism stabilizing the structure.

The simplest model leading to a pure SM incommensurate structure is associated with the formation of a spin density wave (SDW). As observed in Cr, the incommensurate wave-vector is not "connected" to the lattice and can change as a function of temperature without reaching a commensurate "lock-in" [Fawcett (1988), Gibbs, Mohanty *et al.* (1988)]. This concept, however, mostly applies to itinerant magnets (non-local spins). In

HF materials (and the same is true for rare earth alloys), since there is evidence for local moments in the ordered phase as well as in the paramagnetic region, another mechanism has to be invoked. We shall come back to this discussion after the results in a high magnetic field are presented in the next section.

B) Magnetic Order in High Magnetic Field

Several experiments were performed at the N5 spectrometer at NRU Reactor (Chalk River Laboratories) to investigate the effects of high magnetic fields on the magnetic order in UNi_2Al_3 . The ^4He vertical field cryostat, M3, could reach temperatures down to $\approx 2\text{K}$ and generate vertical fields up to 8 Tesla. All the experiments presented in this section were carried out at a neutron energy of 14.5 meV with a graphite filter inserted on the scattered side to remove higher energy neutrons. Collimation on the incident and on the scattered side were 0.55° and 0.6° respectively. The sample was mounted in the $(h0l)$ scattering plane and the vertical magnetic field was therefore oriented along one of the hexagonal axes of the unit cell (b-axis) [see diagram in Fig. 3-24].

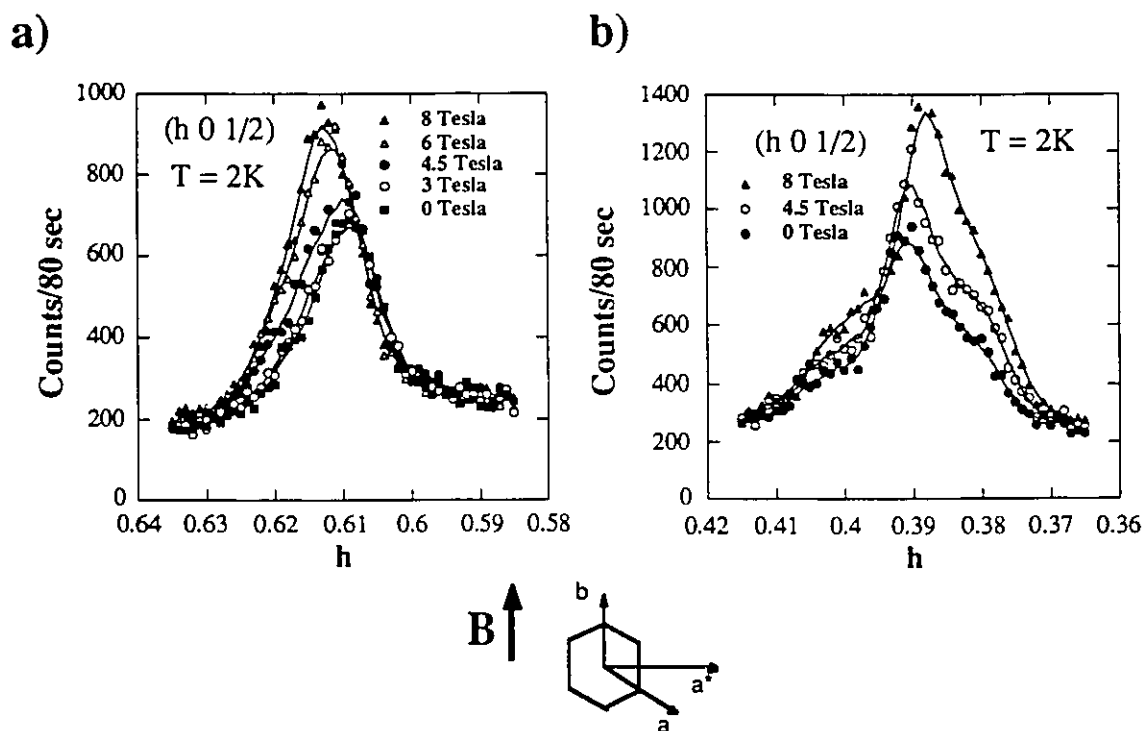


Figure 3-24: a) and b) a^* -scan through the two magnetic satellites $(1/2 \pm \tau \ 0 \ 1/2)$ of UNi_2Al_3 for different magnetic fields at a temperature of 2K. The continuous lines are guides to the eye. The magnetic field orientation for this experiment is shown in the diagram at the bottom (the c^* -axis points out of the page).

The magnetic field modified both the position and the intensity of the magnetic satellites. Fig. 3-24 a) and b) shows that both magnetic satellites drift away from $(1/2 \ 0 \ 1/2)$ position and increase in intensity for increasing fields. Fig. 3-25 gives a more detailed view of the effect at the $(1/2+\tau \ 0 \ 1/2)$ satellite after a gaussian fit is made through the Fig. 3-24 a) data set. After being relatively constant for field values less than ≈ 3 Tesla, the intensity of the satellite smoothly increases until an apparent new stable value is achieved at ≈ 6 Tesla (≈ 1.5 the zero-field intensity). After integration of the peaks shown in Fig. 3-24 b), the same saturation intensity is observed at the $(1/2-\tau \ 0 \ 1/2)$ satellite (≈ 1.527 the zero-field intensity). The evolution between two apparent stable states is also seen in the slight variations of the incommensurate wave-vector in Fig. 3-25 b). Within error bars in Fig. 3-25, no hysteresis was observed when the field was brought back to zero field.

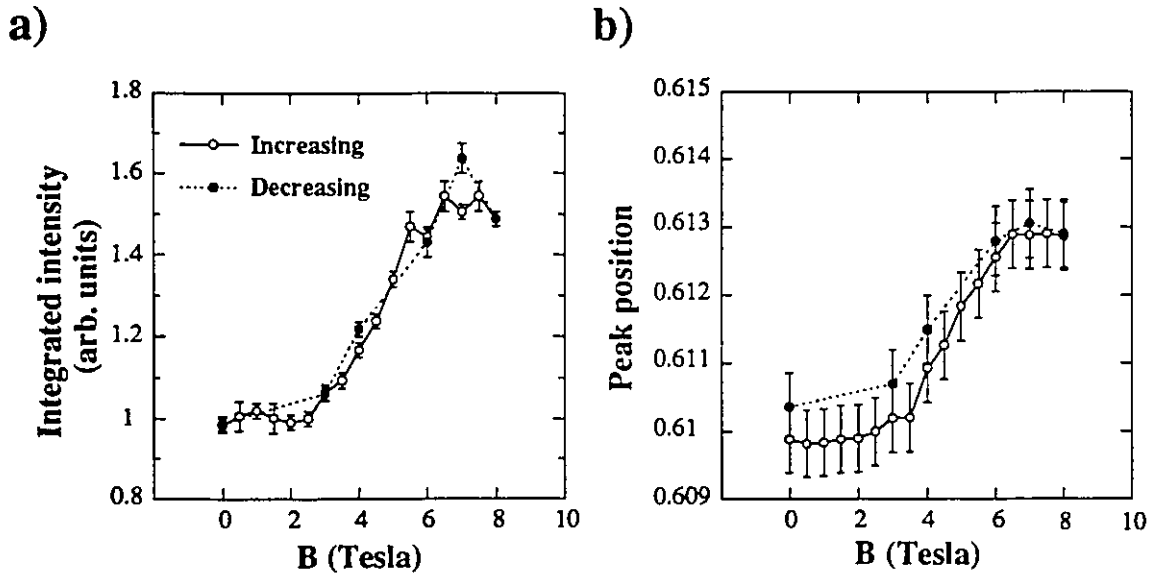


Figure 3-25: Magnetic field dependence of the a) Integrated intensity and b) position $(1/2+\tau \ 0 \ 1/2)$ magnetic satellite of UNi_2Al_3 obtained from a gaussian fit through the Fig. 3-24 a) dataset. The measurement was made at the cryostat base temperature of 2K.

Bulk measurements on UNi_2Al_3 provide evidence of a magnetic transition near $\approx 3.5\text{T}$ at 2K [Fig. 3-26]. Steglich *et al.* (1991) interpreted the B_D phase boundary in this diagram as being due to some domain effects. The evolution of domains in our experimental configuration, however, is difficult to predict since the vertical magnetic field was not oriented along a domain direction (the b -axis is not along the b^* domain direction in hexagonal structures). Nevertheless, if all three single- q domains were to merge into one, the magnetic intensity of each satellite would have to increase by a factor 3 at full saturation (or decrease to zero). Fig. 3-25 a) clearly shows that it is not the case since the intensity was found to increase by only 50% at saturation. Until a simultaneous measurement is performed at the 3 different domain directions, we can only speculate about the origin of the intensity change. We cannot rule out the possibility, for example, that all the domains were not equally populated in zero field or that the saturation is not complete at 8 Tesla. Domain effects, however, cannot account for the change in peak position observed in Fig. 3-25 b).

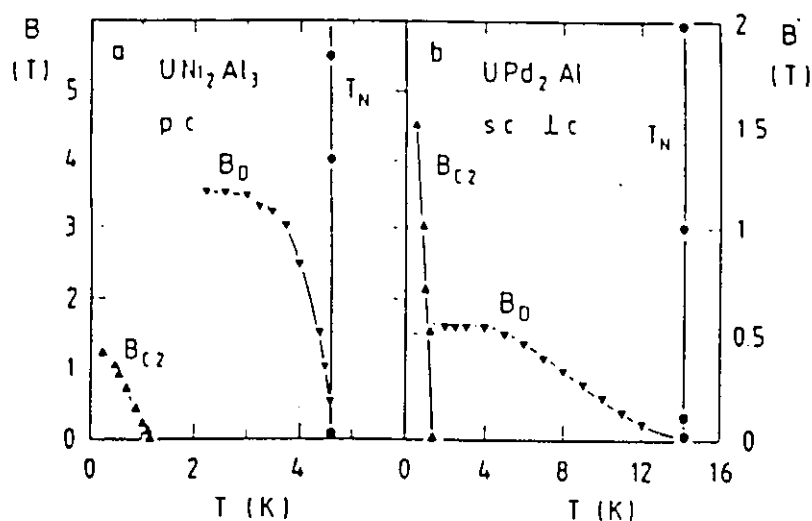


Figure 3-26: Magnetic phase diagram of UNi_2Al_3 polycrystal from Steglich *et al.* (1991).

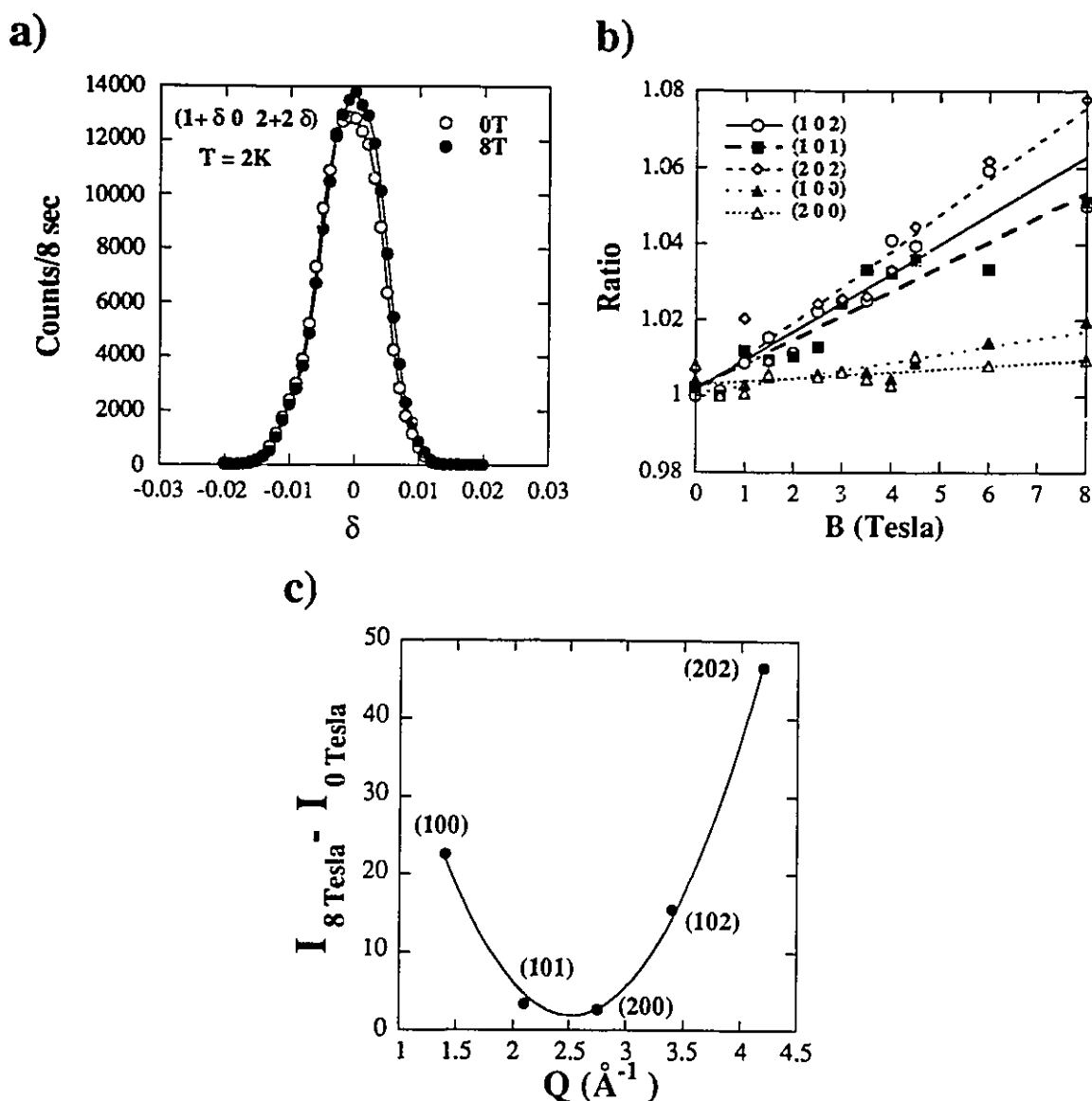


Figure 3-27: Nuclear peak intensity of UNi_2Al_3 upon variation of the external magnetic field. a) Shows the increase seen at (102) through a radial scan. In b) the intensity ratios obtained from radial scans are shown for several nuclear reflections. Straight lines are least square fit. In c), the intensity difference between the nuclear peaks at 8T and at 0T are plotted vs. Q . The solid line is an arbitrary quadratic fit through the points.

The nuclear peaks were also found to be affected by the magnetic field. Radial scans performed at 0T and 8T in Fig. 3-27 a) give a good account of the size of the effect at the (102) nuclear Bragg peak. The lattice parameters were not modified by the field. The

width of the peaks had no detectable field dependence and when the field was brought back to its initial value (0T), no hysteresis was found. In a field, the nuclear peak intensities were not modified when the temperature was set above the T_N . When the intensity ratio is plotted for several nuclear reflections, a trend in data is clearly visible [Fig. 3-27 b)]. Errors bars in this figure are at most 2%.

It would be tempting to associate the modifications at the nuclear and at the magnetic peaks to a change in the magnetic structure caused by the external magnetic field. As the field of this experiment is perpendicular to the spin direction (the field direction in this experiment is perpendicular to the a^* -axis), the intensity increase at the nuclear peaks could qualitatively be associated with a ferromagnetic component coming from a tilt of the spins in the direction of the field. However, this is difficult to establish since the intensity difference, $(I_{8\text{Tesla}} - I_{0\text{Tesla}})$, does not follow the Q -dependence due to a form factor, $f(Q)^2$ [Fig. 3-27 c)]. This Q -dependence also does not seem to be associated with a magneto-elastic effect²⁸. To investigate if a change in the magnetic structure occurs in high magnetic fields, the magnetic peak intensities (incommensurate satellites) have been plotted vs. α [Fig. 3-28]. The α -dependence found at 8 Tesla matches the zero-field result (LSM with an a^* polarization) and indicates that there is no evidence for a change in the magnetic structure at high fields.

²⁸ Magneto-elastic effects are the feed through of a phonon mode into the magnetic channel. Such effects would have $I_{\text{obs}} = I_0 f(Q)^2 Q^2$ dependence. [Stirling (1987)]

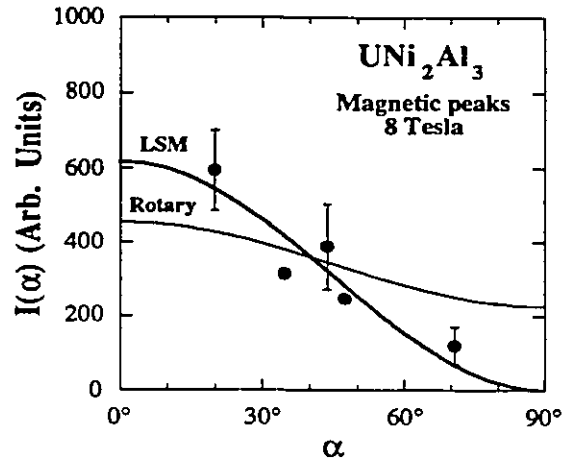


Figure 3-28: Intensity of the $(1/2+\tau \ 0 \ 1/2)$ magnetic satellite vs. α in 8 Tesla fields. The definition of the angle α is the same found in Fig. 3-21 b).

In the discussion so far, we have neglected a possible modification of the magnetic ion ground state through the action of the magnetic field. This effect could change the size of the magnetic moment and explain the intensity increase in Fig. 3-25 a).

In rare earth alloys, the stability of SM structures at low temperature can be explained only if the ground state of the magnetic ion is a *singlet* (or non-magnetic) [Gignoux *et al.* (1991)]. Such singlet ground states can originate from crystal field properties or, as it is the case in HF compounds, it can arise from the many-body interactions leading to the formation of a Kondo ground state [Rossat-Mignod (1987)]. It may appear contradictory that a non-magnetic state is the basis of a magnetic structure. In a lattice, however, competing interactions between the neighbouring magnetic ions generate a periodic molecular field (PF) that mixes the singlet state with some magnetic excited states. A variable moment size between zero and the maximum crystal field value is then, in principle, observable [Barbara *et al.* (1979)]. These ideas have been applied to explain

the stability of the transverse spin modulated (TSM)²⁹ incommensurate order in the magnetic heavy fermion CeAl₂ [Barbara *et al.* (1977)]³⁰.

In an external magnetic field, as observed in magnetization curves, SM structures present a multi-step behaviour associated with metamagnetic processes when the field is oriented along the modulation direction [Gignoux *et al.* (1991)]. When the field is perpendicular to that direction (as in our experiment), it is not clear that such metamagnetic transitions can be observed. Nevertheless, the intensity increase and the slight displacement of the incommensurate wave-vector in Fig. 3-25 a) and b) may suggest that the external magnetic field weakly modifies the competition between the interactions.

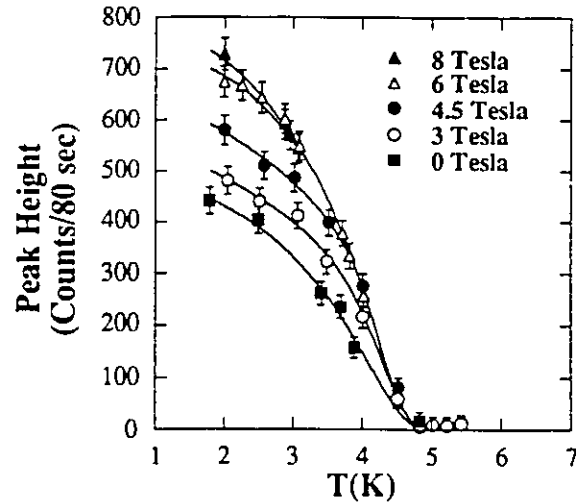


Figure 3-29: Order parameters in a field at the UNi₂Al₃ (1/2+τ 0 1/2) magnetic reflection. The lines are guide to the eye.

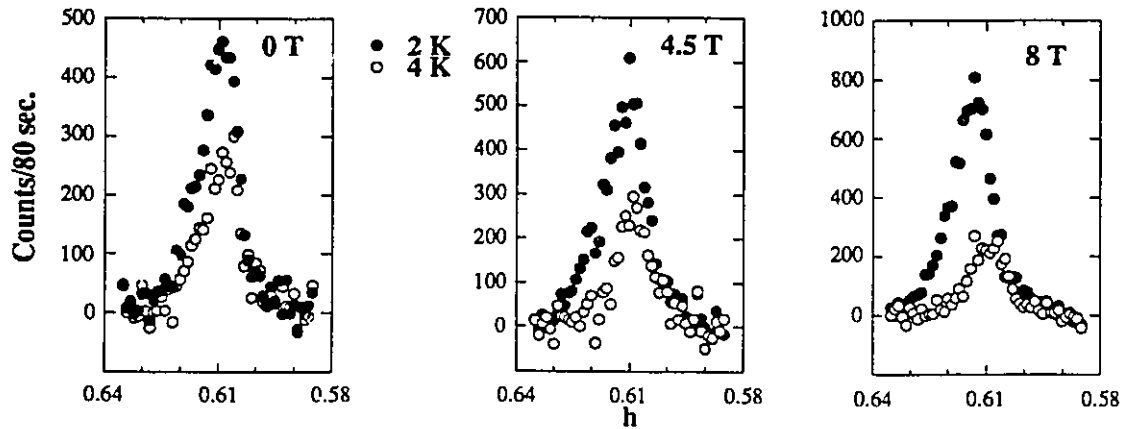
We further investigated the stability of the LSM structure in UNi₂Al₃ by measuring the evolution of the (1/2+τ 0 1/2) incommensurate satellite as function temperature for

²⁹I would like to thank Dr. C. Vettier to have brought this compound to my attention.

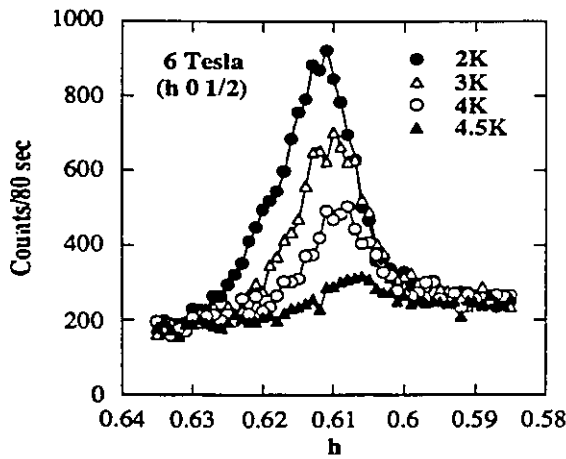
³⁰This view is somewhat challenged today by Forgan (1990) but we will not address this issue in the present thesis.

several magnetic fields. The in-field order parameters, presented in Fig. 3-29, show that the value of T_N as well as the shape of the curves are similar to zero-field data (they only differ by a scaling factor).

a)



b)



c)

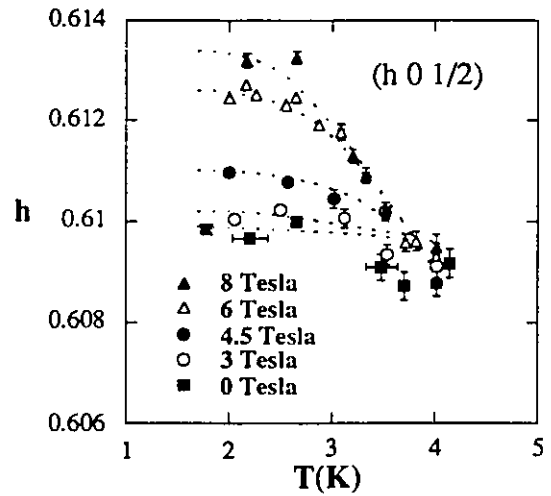


Figure 3-30: a) Comparison at 2K and 4K of the incommensurate wave-vector for a series of magnetic fields in UNi_2Al_3 . The peaks are corrected for a sloping background. b) a^* -scans at $(h \ 0 \ 1/2)$ for several temperatures in a 6 Tesla field. c) Temperature dependence of the incommensurate periodicity τ for several fields. The dotted lines are guides to the eye.

The position of the magnetic satellites shows some temperature dependence. As displayed in Fig. 3-30 a), the magnetic field amplifies the displacement of the magnetic satellite (at 4K) compared to its low temperature position (at 2K). Fig. 3-30 b) shows a more detailed view of the displacement as function of temperature in a 6 Tesla field. In Fig. 3-30 a), although the zero-field neutron data does not clearly show such displacement, a resonant X-ray measurement (which offers better Q-space resolution) in Fig. 3-35 suggests that a weak displacement occurs for temperatures greater than 1K. Below this temperature, the satellite peak seems to remain at the same wave-vector, which suggests that the LSM structure is stable in UNi_2Al_3 .

In the low temperature part of Fig. 3-30 c), all the in-field incommensurate wave-vector positions become independent of temperature. This may indicate that the singlet ground state is unaffected by external magnetic fields less than 8 Tesla, which is compatible with the relatively high Kondo temperature in this compound. However, as the temperature increases, all the in-field incommensurate wave vectors move and eventually merge to the zero-field value at 4K. It is possible that by Zeeman splitting, parts of the magnetic state, initially mixed within the singlet ground state, are lost at low temperatures, but are later recovered by thermal activation at $\approx 4\text{K}$.

There are still many questions open and this high field study only revealed the need for a more detailed knowledge of the magnetic structure of UNi_2Al_3 . For example, it is essential to understand precisely the type of magnetic order (single-q or multiple-q) existing in UNi_2Al_3 . Also, a magnetic field oriented along a^* is necessary to study possible metamagnetic transitions in this compound. Nevertheless, our measurements have shown some evidence that the magnetic properties of UNi_2Al_3 depend strongly on

its Kondo ground state which seems different compared to the ground state of the isostructural UPd_2Al_3 .

3.3) Magnetic Order and Superconductivity in UPd_2Al_3 and UNi_2Al_3

3.3.1) UPd_2Al_3 [Gaulin *et al.* (1994)]

To monitor a change in the magnetic intensity at the superconducting phase transition, a resonant magnetic X-ray experiment was performed on UPd_2Al_3 at the NSLS X-14 spectrometer. The polycrystalline UPd_2Al_3 sample (already described in previous sections) was put in a dilution refrigerator that could reach a temperature of $\sim 250\text{mK}$, well below the superconducting temperature of 2K . To enhance the magnetic intensity, the incident X-ray wavelength was chosen to match the uranium M_{IV} -edge. The measurement was made with a Ne- CO_2 proportional counter detector.

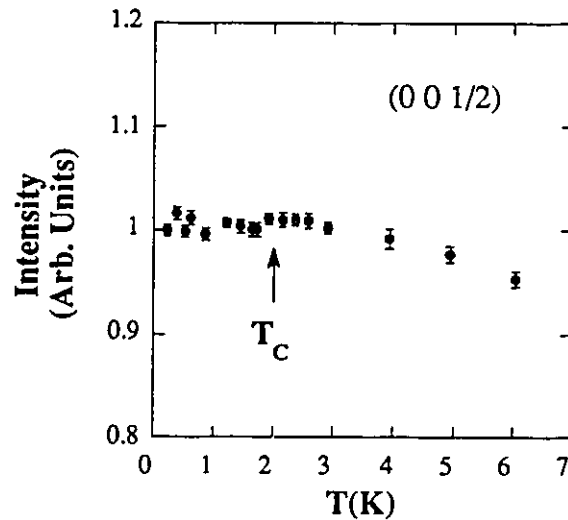


Figure 3-31: Magnetic order parameter of the $(0\ 0\ 1/2)$ magnetic reflection near the superconducting phase of UPd_2Al_3 .

The order parameter at the $(0\ 0\ 1/2)$ magnetic reflection, shown in Fig. 3-31, contrasts with previous findings from Krimmel *et al.* (1993). No change in intensity was observed at or below T_c . In addition to the statistical errors shown on Fig. 3-31, systematic errors, attributed to an orbit drift of the synchrotron, was estimated to be no more than 2%. For comparison purposes, the Krimmel *et al.* (1993) result is shown in Fig. 3-32.

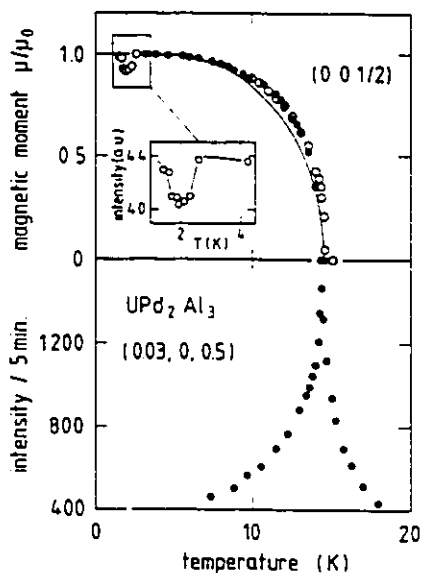


Figure 3-32: Magnetic order parameter at the superconducting phase transition with a 10% decrease at T_c [Krimmel *et al.* (1993)].

3.3.2) UNi₂Al₃

In this X-ray experiment also performed at the NSLS X-14 beamline, constraints on the incident energy and on the tilt of the cryostat limited access to reciprocal space. Because of the geometry of the spectrometer and the necessity to keep the cryostat (dilution refrigerator) in the vertical upright position, some care had to be taken before putting the sample in the beam. This sample, cut from the neutron scattering sample already presented earlier in this chapter, had its surface approximately perpendicular to the (101)-direction. After using a spark cutter, the sample was polished and etched to minimize surface strain. In the final experimental configuration, only one magnetic reflection, $(1/2+\tau \ 0 \ 1/2)$ could be accessed and the whole crystal alignment procedure could only be made using higher order wavelengths. Fig. 3-33 and Table 3-9 give some aspects of the geometry of this experiment.

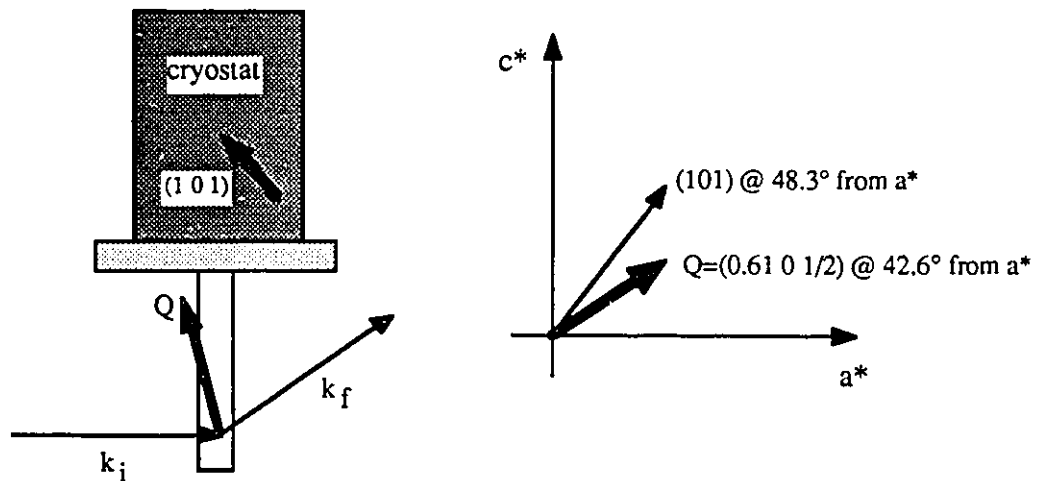


Figure 3-33: Mounting procedure of the UNi₂Al₃ sample for the X-ray experiment at X-14. Angles are not to scale.

	θ	$\angle \mathbf{a}^* \mathbf{k}_f$
(0.39 0 1/2)	14.62°	20.17°
(0.61 0 1/2)	17.82°	29.56°
(0.39 0 3/2)	39.65°	-26.62°
(0.61 0 3/2)	41.39°	-21.48°

Table 3-9: Some of the possible magnetic reflections of UNi_2Al_3 for the X-ray experiment in the superconducting phase. θ is the scattering angle and $\angle \mathbf{a}^* \mathbf{k}_f$ is the angle between the spin direction (along \mathbf{a}^*) and the scattered wave-vector \mathbf{k}_f .

Fig. 3-34 a) shows the integrated intensity obtained from Ω -rocks taken at the $(1/2+\tau \ 0 \ 1/2)$ magnetic reflection for several temperatures. The X-ray order parameter was measured in two different runs (open and closed circles) taken below 2K and rescaled to match in intensity. In this experiment, T_N was estimated at $4.6 \pm 0.2\text{K}$. The dotted line in Fig. 3-34 a) is a smoothed curve through the data points. The superconductivity (T_c) of this sample was characterized by an *in situ* AC-magnetization measurement using two counter rotating coils. T_c was found to be $\approx 1.2\text{K}$.

In Fig. 3-34 b), the neutron and X-ray order parameters have been rescaled to match in intensity at the lowest temperature. In spite of the difference in T_N , the slopes of the two order parameters are found to agree remarkably. It is puzzling to find such a variation in T_N with samples coming from the same boule. It seems, however, that the discrepancy probably comes from the wrong sensor calibration of the neutron experiment and not to sample problems³¹.

³¹Other measurements on the same sample confirmed a T_N near 4.6K [see Fig. 3-29].

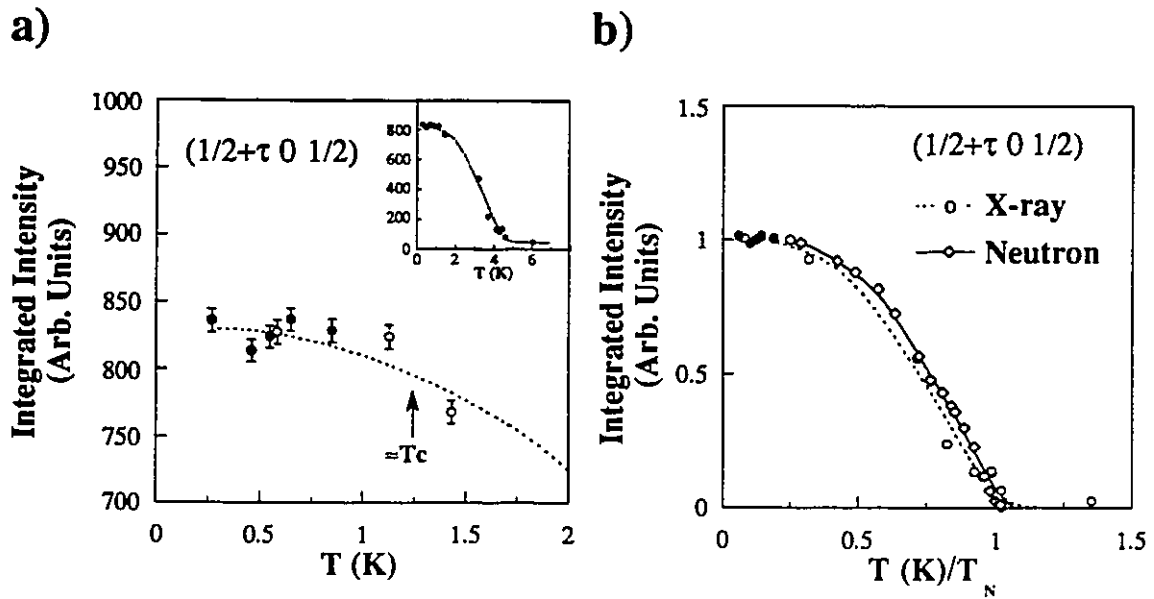


Figure 3-34: a) Magnetic order parameter of UNi_2Al_3 in the superconducting region (below 2K) at $(1/2+\tau \ 0 \ 1/2)$. The inset shows the same order parameter over the whole temperature range. The symbols are explained in the text and the dotted line is a guide to the eye. b) Rescaled X-ray and neutron order parameters plotted vs. T/T_N . ($T_N=4.6K$ for the X-ray curve and $T_N=5.2K$ for the neutron curve). The neutron order parameter is identical to Fig. 3-20 b).

The incommensurate magnetic order in UNi_2Al_3 offers also an interesting way to detect any rearrangement of the Fermi surface at the superconducting transition. To monitor any modification at the incommensurate wave-vector position, a^* -scans were made at $(1/2+\tau \ 0 \ 1/2)$. While Ω -rocks were made with a relatively wide slits setting, a^* -scans were performed with a narrower setting to improve Q-space resolution. As shown in Fig. 3-35, the position of the magnetic peak did not change with temperature (below 1K) and no effects could be associated with the superconducting transition. The constraints associated with this measurement prevented an evaluation of the magnetic correlation length ξ since no charge peaks were accessible.

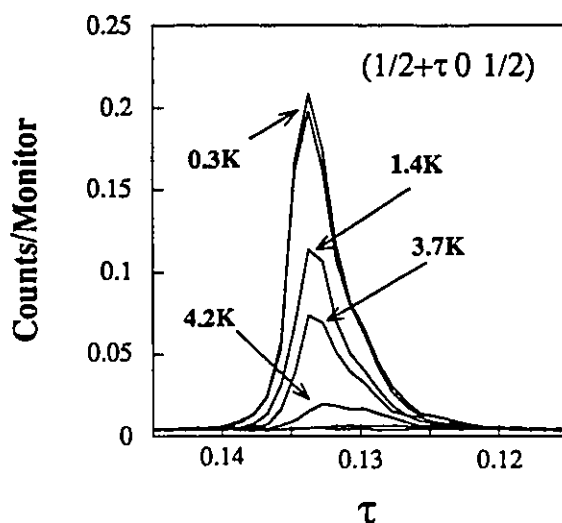


Figure 3-35: Scans along a^* -direction vs. temperature at the $(1/2+\tau \ 0 \ 1/2)$ magnetic position. The irregular shape of the scans comes from the crystal mosaic. The incommensurate wave-vector is temperature independent until $\approx 4\text{K}$.

It is worth ending this section by comparing the several resonant magnetic X-ray intensities obtained from the HFS compounds measured at the same spectrometer (X-14) and approximately in the same conditions (cryostat, slits setting, lowest temperature, etc.). The measured intensities from URu_2Si_2 (8 cps at (003)), the present experiment (450 cps at $(0.61 \ 0 \ 1/2)$) and UPd_2Al_3 (1600 cps at $(0 \ 0 \ 1/2)$) give an intensity ratio of 1:60:200 that nearly scale as the ordered moment squared 1:20:450.

3.3) Uranium Valence State in UNi₂Al₃

The M_{IV}/M_V branching ratio could not be evaluated by earlier X-ray experiments on URu₂Si₂ and UPd₂Al₃ for the simple reason that no intensity was observed at the M_V -edge. Measurements with UNi₂Al₃ offered the first opportunity to observe magnetic intensity at the M_V -edge and represents the first attempt to extract the uranium valence for this series of compounds. The branching ratio is obtained by comparing the amplitudes of the resonance profiles at the M_{IV} -edge and at the M_V -edge. Free-ion calculations for uranium give an expected ratio of 17 for $5f^2$ (U⁴⁺) and 6 for the $5f^3$ (U³⁺) configuration states [Tang *et al.* (1992)].

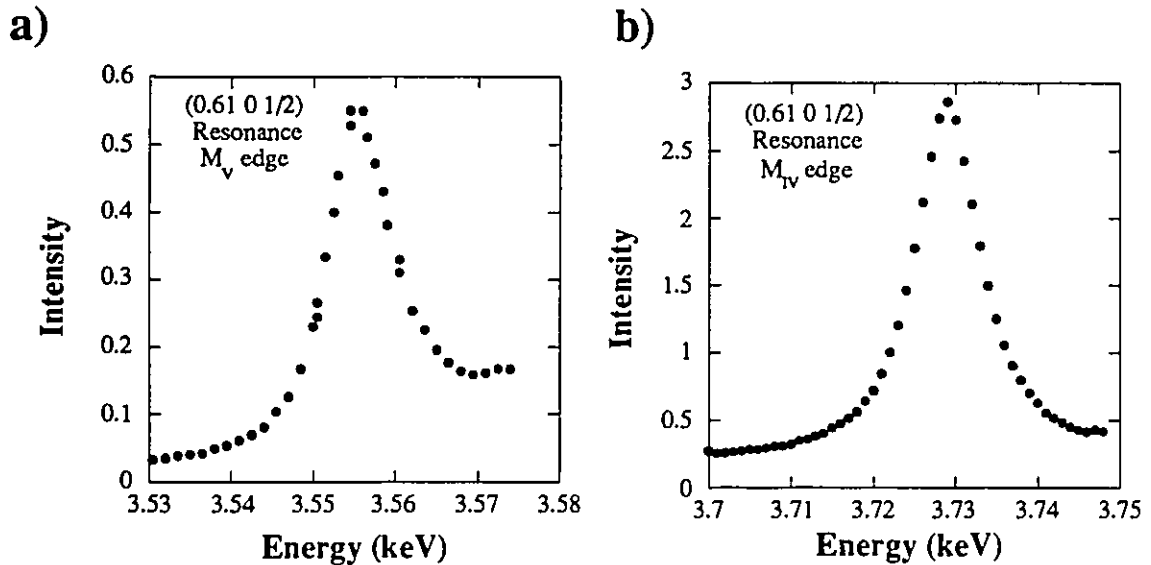


Figure 3-36: Uncorrected resonance profiles of the a) M_V -edge and b) M_{IV} -edge at the UNi₂Al₃ (0.61 0 1/2) magnetic position.

Fig. 3-36 show the uncorrected resonance profiles obtained at both edges in UNi₂Al₃. Each resonance profile was made with the integrated intensity of Ω -rocks at each energy. All these scans were made at a temperature of 0.3K, well into both the magnetic and the

superconducting phases. To estimate the branching ratio, several corrections must be applied to the profiles, the most critical being the correction for absorption and its dependence with energy.

Fig. 3-37 shows the energy dependence of the absorption corrections of Be and Kapton placed on the path of the beam. At NSLS X-14 beamline, there were as many as five 250 μ m Be-windows along the path: 4 from the cans of the cryostat, plus one Be window near the synchrotron source. In addition, as much as three 13 μ m-Kapton windows were also present in the beampath. Empirical relations from Tang *et al.* (1992) were used to estimate the energy variation of Be $\mu_{\text{Be}} = 1067.9 / E^{2.931}$ and Kapton $\mu_{\text{Kapton}} = 4567 / E^{3.3}$.

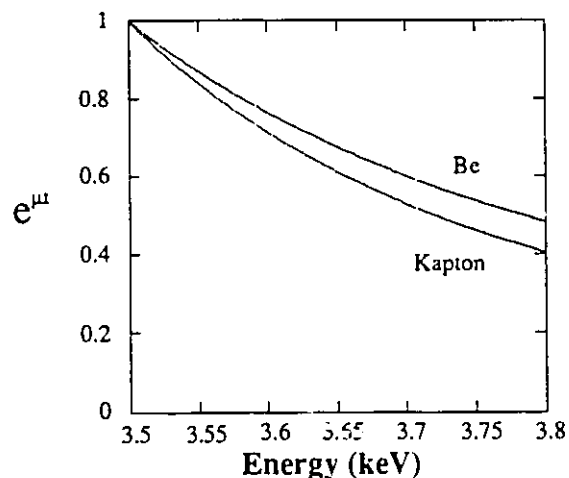


Figure 3-37: Energy dependence of the Be and Kapton absorption coefficients for this experiment. Adapted from Tang *et al.* (1992).

To estimate the absorption of the sample, fluorescence measurements were made at each edge. Fig. 3-38 shows the calibrated absorption coefficient after the correction procedure already described in chapter 2 (section 2.2.2) was applied. At the M_{IV} -edge, the lineshape could be well reproduced by a Lorentzian on a step background but at the M_V -

edge, the curve had a sloping background and was difficult to fit. The slight decrease observed at energies greater than the edge [Fig. 3-38 a)] has some similarities with XAFS, but its real origin is unknown. Some mosaic could have contaminated the measurement of the resonance profile and of the fluorescence curve at this energy. In the final analysis, the sloping background in Fig. 3-36 a) was subtracted and the continuous line in the Fig. 3-38 a) and b) was used instead.

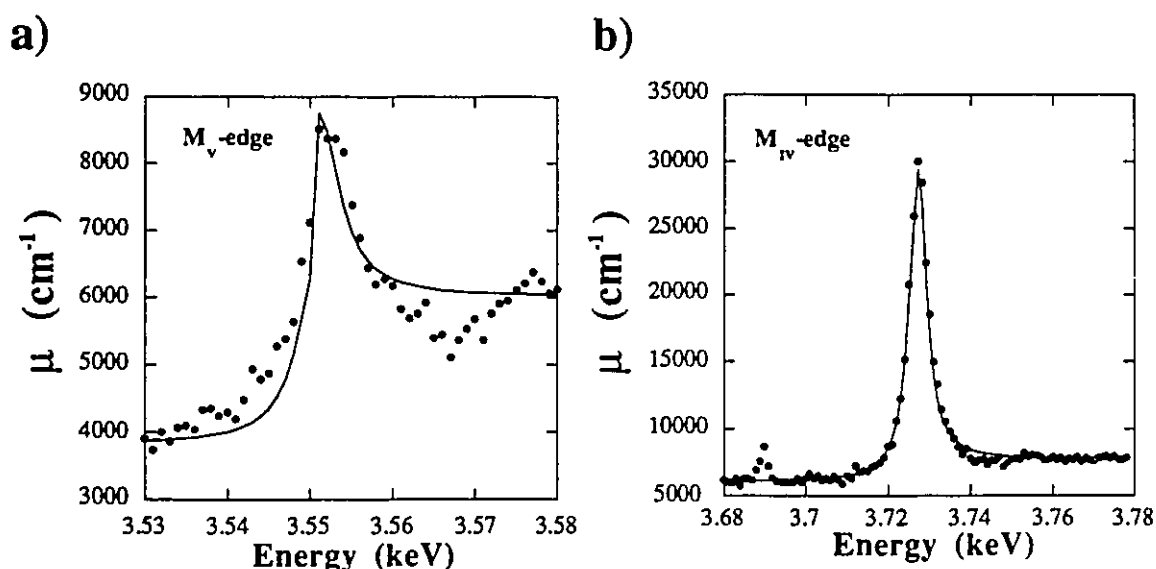


Figure 3-38: Fluorescence curve at the a) M_V^{32} and b) M_{IV} -edge in UNi_2Al_3 . The continuous line is a Lorentzian on a step function background.

Theoretically the energy response at one frequency $F_{LM}(\omega)$ includes a sum over the contributions from all edges. Resonance profiles are relatively well localized around the excitation energy and only the edges close together need to be considered. For M_{IV} and M_V -edges, the intensity lineshape of the magnetic resonance would require [Tang *et al.* (1992)]³³:

³²The absorption coefficient at this edge $\approx 8700 \text{ cm}^{-1}$ differs from the one reported by Langridge *et al.* (1994): 21500 cm^{-1} .

³³There is a difference in sign between this equation and the one published in Tang (1992).

$$I(E) \propto \left| \frac{A_4}{1 + [(E_4 - E)/(\Gamma_4/2)]^2} + \frac{A_5}{1 + [(E_5 - E)/(\Gamma_5/2)]^2} + \dots \right|^2 + \dots$$

$$\dots + \left| \frac{A_4}{1 + [(E_4 - E)/(\Gamma_4/2)]^2} \left[\frac{E_4 - E}{\Gamma_4/2} \right] + \frac{A_5}{1 + [(E_5 - E)/(\Gamma_5/2)]^2} \left[\frac{E_5 - E}{\Gamma_5/2} \right] \right|^2 \quad (3.10)$$

The last term of Eq. (3.10) describes the interference that can occur between edges. This interference term creates an asymmetry at the M_V -edge resonance profile that would decrease the intensity for $E > E_5$. This effect cannot explain the asymmetry of the Fig. 3-36 a) resonance profile. Due to the strength of the M_V -edge and its peculiar lineshape [Fig. 3-38 a)], this interference seems negligible and was not included. The corrected resonance profiles using a simple Lorentzian lineshape appear in Fig. 3-39. The slight distortions in the tails may come from the uncorrected detector efficiency.

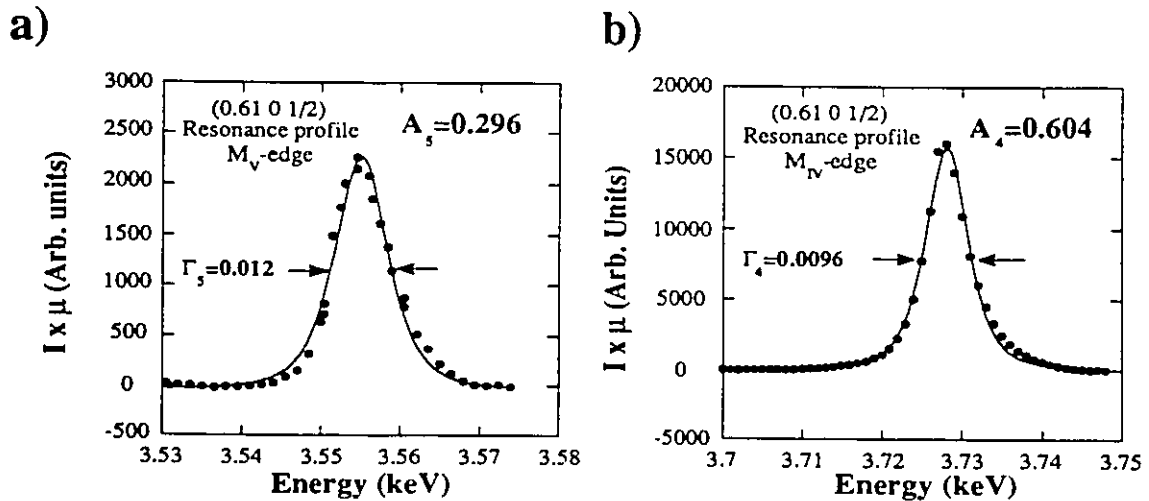


Figure 3-39: Corrected resonance profiles at a) M_V and b) M_{IV} -edge in UNi_2Al_3 with the corresponding amplitudes and widths from the fit results.

The widths of the two resonance profiles are slightly broader than reported by Tang *et al.* (1992) in UO_2 , an insulator. In terms of lifetimes, the resonances in UNi_2Al_3 are shorter

than in UO_2 , as expected in a metal. The experimental branching ratio gives a value of $A_4/A_5 \approx 2$ and the uncorrected intensities give a ratio of $\sqrt{I_4/I_5} \approx 3$. Within experimental accuracy, this experiment would suggest a uranium $5f^3$ (U^{3+}) configuration in UNi_2Al_3 ³⁴. This valence configuration would be different than the tetravalency proposed in the iso-structural UPd_2Al_3 . However, a theoretical calculation for the expected branching ratio in this material would certainly give a better estimate than the free ion calculation. For example, the modification of the $5f^2$ (U^{4+}) branching ratio from 17 to 6 in UO_2 [Tang *et al.* (1992)], is compatible with the crystal field levels found by neutron scattering. Preliminary inelastic neutron scattering results on UNi_2Al_3 did not reveal any sharp crystal field excitations up to ≈ 17 meV nor any spin waves³⁵.

³⁴Based on the discussion in Sec. 3.2.2), only a $5f^2$ configuration would give a singlet ground state based on crystal field properties.

³⁵Spin waves in incommensurate structures can be complicated, see Stirling (1987).

Conclusion

In this thesis we studied the magnetic phase of three of the Heavy Fermion Superconductors (HFS): URu₂Si₂, UNi₂Al₃ and UPd₂Al₃, using neutron and resonant magnetic X-ray diffraction. In doing so, our interest was two-fold. First, we wanted to characterize the magnetic structures and some of the magnetic properties of the UT₂Al₃ (T=Ni, Pd) compounds, and second, we wanted to get a better understanding of the resonant magnetic X-ray cross-section in URu₂Si₂.

Our study of the magnetic state of the new Ni and Pd HFS revealed several interesting results. With UNi₂Al₃, neutron diffraction experiments identified, for the first time in this material, the onset of long range magnetic order. The incommensurate order found at $(1/2 \pm \tau \ 0 \ 1/2)$ with $\tau=0.110 \pm 0.003$ seems well described by a LSM model with an a* polarization in the hexagonal basal plane. This modulated magnetic structure, however, is known to be thermodynamically unstable at low temperature. The essentially non-magnetic ground state in HF materials offers an interesting theoretical concept which could explain why such a structure is stable to the lowest temperature in UNi₂Al₃. Other measurements are needed to answer this question.

It was not possible to clearly establish from our study whether the magnetic structure of UNi₂Al₃ is single-q or multiple-q. This distinction is of importance in the description of the evolution of the magnetic order in a high magnetic field and in the evaluation of the moment size. The intensities of the magnetic satellites were found to smoothly evolve between two apparently stable "incommensurate" values between 3 Tesla and 6 Tesla.

However, the field orientation in our experiment couples many possible phenomena (domain population, spin rotation, change in moment size) and no simple effect could describe the data. The slight change in wave vector induced by the external field suggests a change in the balance between the competing interactions responsible for the LSM structure in UNi_2Al_3 .

In UPd_2Al_3 , the magnetic term (1st harmonic) in the resonant X-ray cross-section was used to find the spin orientation in the basal plane. Results indicate, if only one domain is assumed to contribute to the intensity, that the spins do not point along the a^* -axis but would point along the a -axis or in the mid-direction between the a -axis and the a^* -axis. These findings are compatible with an a -axis orientation found by several bulk measurements. The same polycrystalline sample was also used to measure magnetic order parameters in the normal and in the superconducting phase. In the normal state, we found a large anomaly at 12K. This anomaly was also observed by neutron scattering and corresponds to a phase line in the H-T diagram at 0 Tesla. An analysis based on domain populations suggests that a domain reorganization may be at the origin of the transition.

In the superconducting phase, we found no evidence that the new HFS (UT_2Al_3 with $T=\text{Ni}$ and Pd) show any direct interplay between magnetism and superconductivity even if their ordered moment is rather large. In UPd_2Al_3 , the precision of the order parameter reached the 2% level using resonant X-ray scattering while with UNi_2Al_3 the precision reached $\approx 10\%$. This co-existence is similar to what is found in URu_2Si_2 .

We also wanted to get a better understanding of the resonant magnetic X-ray cross-section with the study of the magnetic Bragg peaks in URu_2Si_2 . The relative intensities

of the magnetic reflections were well described by the 1st harmonic of the electric-dipole cross-section and some experimental corrections. The absence of a magnetic form factor in the analysis, is in direct agreement with the fact that the photon wavelength at the M-edge is larger than the inner shells involved in the transition. The evaluation of the moment size was more problematic. The normalization procedure is relatively straightforward in neutron scattering but in the X-ray case, anomalous corrections, absorption effects, and the necessity of an accurate atomic model give unsatisfactory errors in the evaluation of the moment size. Strictly speaking, resonant magnetic X-ray scattering contains all the information about the magnetic state but the proportionality constant depends on the atom and on the resonant edge chosen (see Appendix A).

Apart from this limitation, resonant magnetic X-ray scattering is an attractive magnetic probe because it can be used to select different atoms in the unit cell and isolate where the magnetism is lying. It can also help identify the magnetic order in small moment systems ($\approx 10^{-2}\mu_B$) and especially in very small crystals.

Epilogue

This thesis has shown that neutron and X-ray scattering can be used effectively to study magnetism in metals and in particular in the U-based HFS. Our research has also shown that resonant X-ray scattering and neutron scattering are complementary magnetic probes and constitute remarkable tools in the study of magnetism in materials science.

Appendix A: The physics at resonance

In the resonant process leading to magnetic X-ray scattering, it is worth commenting on the peculiar physics one can observe when diffraction is performed directly at an absorption edge. Some possible perturbations altering the resonant state are discussed.

A.1) The quasi-elastic fast collision approximation

The lifetime of the excitation can have very important consequences on the interpretation of the magnetic scattering obtained by resonant X-ray scattering. If the core-hole pair live long enough, torques can start to develop and alter the oscillator response [Luo *et al.* (1993)]. If this occurs, the magnetic scattering may not be proportional to the moment size.

For most of the compounds studied in this thesis, typical resonance widths are of the order of 10 eV which gives an estimated core-hole lifetime of 10^{-16} sec; the resonance is fast. Luo *et al.* (1993) demonstrated that in the *quasi elastic fast collision approximation* the oscillator responses in Eq. (1.19) can be rewritten, using the Wigner-Eckart theorem, as:

$$f_{\text{E-dipole}}^{\text{res}} = \frac{3}{4} \lambda \tilde{F} \left\{ \tilde{\mathbf{e}}_f^* \cdot \tilde{\mathbf{e}}_i \mathbf{M}^{(0)} - i(\tilde{\mathbf{e}}_f^* \times \tilde{\mathbf{e}}_i) \cdot \hat{\mathbf{z}} \mathbf{M}^{(1)} + (\tilde{\mathbf{e}}_f^* \cdot \hat{\mathbf{z}})(\tilde{\mathbf{e}}_i \cdot \hat{\mathbf{z}}) \mathbf{M}^{(2)} \right\} \quad (\text{A.1})$$

where, \tilde{F} is the overlap integral between the initial and of the final orbital involved in the atomic transition known as the "reduced resonance scattering amplitude", and \mathbf{M} are the

spin-orbital multipole moment operators. The correspondence between the \mathbf{M} and a moment size (s) (at least in the neutron scattering sense of it) is not as obvious as it may seem [see Eq. (16) in Luo *et al.* (1993)]. Experimentally, however, the similarity between the magnetic order parameters in URu₂Si₂ [Isaacs *et al.* (1990)] observed by neutron and by resonant magnetic X-ray scattering suggests that both probes are indeed sensitive to the same magnetic state³⁶.

In the following, we will assume that first harmonic in Eq. (1.21) can be written by isolating a "magnetic moment" (s) from the oscillator response function \mathbf{F}_1 by writing: $\mathbf{F}_1 = \tilde{\mathbf{F}} \mathbf{M}^{(1)} \equiv s \tilde{\mathbf{F}}$, where $\mathbf{M}^{(1)}$ is assumed to be the "magnetic moment" (s). The "reduced resonance scattering amplitude" $\tilde{\mathbf{F}}$ requires an atomic model calculation and strongly depends on the atom and the edge under consideration.

A.2) The Templeton effect

It is difficult not to mention the existence of some complications in the optical properties of a crystal when diffraction is performed directly *at resonance*. Templeton *et al.* (1980) found that when the X-ray absorption fine structure (XAFS) is performed with polarized photons on certain materials, a difference in the absorption spectrum (dichroism) is observed when the polarization is changed. This effect is a manifestation of a change in polarizability of the resonating atom depending on both the symmetry of the final unoccupied orbital and by the geometry of the neighbouring atoms [Templeton *et al.* (1980)]. In diffraction experiments, this effect is known as Anomalous Anisotropic Diffraction (AAD).

³⁶The same correspondence was found in UPt₃. [E.D. Isaacs, private communication].

The most striking effect of AAD is the observation of Forbidden Reflection near Edge Diffraction (FRED). As the resonant frequency is approached, the change in symmetry of the scattering object can modify the "normal" selection rules of a crystal and some additional reflections, usually extinct by the crystal symmetry, may become observable. This effect was found in "naturally" anisotropic materials like CuO, but also in less-anisotropic material like MnF₂, and TiO₂ [Kirfel *et al.* (1991), *et al.* (1992), *et al.* (1993)].

AAD requires the scattering amplitude f be extended into a tensor quantity and can occur in all crystal structures *except cubic*. It can modify the relative intensities of Bragg reflections or in other cases, like in antiferromagnets, it can lead to the existence of a large non-magnetic contribution accompanying the antiferromagnetic Bragg peak. It is worthwhile to add that for this special case, a polarized X-ray experiment, would be essential to separate the two contributions.

Bibliography

G. Aeppli, D. Bishop, C. Broholm, E. Bucher, K. Siemensmeyer, M. Steiner and N. Stüsser, *Phys. Rev. Lett.*, **63**, 6, 676 (1989).

G. Aeppli, C. Broholm, Magnetic Correlations in Heavy Fermion Systems: Neutron Scattering from Single Crystals in Handbook on the Physics and Chemistry of Rare Earths, Vol. 19 (1994) (to be published).

D.T. Attwood et al, X-ray Data Booklet, Douglas Vaughan Ed., Lawrence Berkeley Laboratory (1986).

B. Barbara, J.X. Boucherle, J.L. Buevoz, M.F. Rossignol and J. Schweizer, *Sol. State Comm.*, **24**, 481 (1977).

B. Barbara, J.X. Boucherle, J. Schweizer and J.L. Buevoz, *J. Appl. Phys.*, **50** (3), 2300, (1979).

P.R. Bevington, Data Reduction and Error Analysis for the Physical Sciences, McGraw-Hill Ed. (1969).

M. Blume, *J. Appl. Phys.*, **57**, 3615 (1985).

M. Blume and D. Gibbs, *Phys. Rev. B*, **37**, 4, 1779 (1988).

C. Broholm, H. Lin, P.T. Matthews, T.E. Mason, W.J.L. Buyers, M.F. Collins, A.A. Menovsky, J.A. Mydosh, J.K. Kjems, *Phys. Rev. B*, **43**, 12809 (1991).

F.C. Brown, Inner-shell Threshold Spectra in Synchrotron Radiation Research, Winick and Doniach Ed., Plenum Press (1980).

Y. Cauchois and N. F. Mott, *Philos. Mag.*, **40**, 1260 (1949).

S.-K. Chan, D.J. Lam, Crystal Field Theory in The Actinides: Electronic Structure and Related Properties, A.J. Freeman and J.B. Darby Ed., Materials Science Series Vol. 1, Academic Press, Chap.1 (1974).

N.J. Chesser and J.D. Axe, *Acta Cryst.* **A29**, 593 (1973).

M.F. Collins, Magnetic Critical Scattering, Oxford Series in Neutron Scattering in Condensed Matter (1989).

M.J. Cooper and R. Nathans, *Acta Cryst.*, **23**, 357 (1967).

D.T. Cromer and D. Liberman, *J. Chem. Phys.*, **53**, 1891 (1970).

F. DeBergevin, M. Brunel, *Phys. Lett.*, **39A**, 2, 141 (1972).

- F. DeBergevin, M. Brunel, *Acta Cryst.*, **A37**, 314 (1981).
- F. DeBergevin, M. Brunel, R.M. Galéra, C. Vettier, *Phys. Rev. B*, **46**, 10772 (1992).
- J.P. Desclaux and A.J. Freeman, Atomic properties of the actinides in Handbook on the Physics and Chemistry of the Actinides, A.J. Freeman and G.H. Lander Ed., Chap.1 (1984).
- R.J. Elliott, *Phys. Rev.* **124**, 346 (1961).
- E. Fawcett, *Rev. Mod. Phys.*, **60**, 209 (1988).
- Z. Fisk, H.R. Ott, T.M. Rice and J.L. Smith, *Nature*, **320**, 124 (1986) and Z. Fisk, D.W. Hess, C.J. Pethick, D. Pines, J.L. Smith, J.D. Thompson, J.O. Willis, *Science*, **239**, 33 (1988).
- E.M. Forgan, B.D. Rainford, S.L. Lee, J. S. Abell and Y. Bi, *J. Phys. Condens. Matter*, **2**, 10211 (1990).
- A.J. Freeman, J.P. Desclaux, G.H. Lander and J. Faber Jr., *Phys. Rev. B*, **13**, 3, 1168 (1976).
- P. Fulde, J. Keller, G. Zwicknagl, *Sol. State Phys.*, **41**, 1 (1988).
- B.D. Gaulin, D. Gibbs, E.D. Isaacs, J.-G. Lussier, J.N. Reimers, A. Schröder, L. Taillefer, P. Zschack, *Phys. Rev. Lett.*, **73**, 6, 890 (1994).
- C. Geibel, S. Thies, D. Kaczorowski, A. Mehner, A. Grauel, B. Seidel, U. Ahlheim, R. Helfrich, K. Petersen, C. D. Bredl, and F. Steglich, *Z. Phys. B*, **83**, 305 (1991).
- C. Geibel, C. Schanck, S. Thies, H. Kitazawa, C.D. Bredl, A. Böhm, M. Rau, A. Grauel, R. Casparay, R. Helfrich, U. Ahlheim, G. Weber, and F. Steglich, *Z. Phys.*, **84**, 1, (1991).
- D. Gibbs, X-ray magnetic scattering, *Synch. Rad. News*, Vol. 5, No. 5, p.18 (1992).
- D. Gibbs, G. Grübel, D.R. Harshman, E.D. Isaacs, D.B. McWhan, D. Mills, C. Vettier, *Phys. Rev. B*, **43**, 7, 5663 (1991).
- D. Gibbs, D.R. Harshman, E.D. Isaacs, D.B. McWhan, D. Mills, C. Vettier, *Phys. Rev. Lett.*, **61**, 10, 1241 (1988).
- D. Gibbs, K.M. Mohanty and J. Bohr, *Phys. Rev. B*, **37**, 562 (1988).
- D. Gignoux and D. Schmitt, *J. Magn. Magn. Mater.*, **100**, 99 (1991).
- A.I. Goldman, G. Shirane, G. Aeppli, B. Batlogg, E. Bucher, *Phys. Rev. B*, **34**, 9, 6564 (1986).
- A. Grauel, A. Böhm, H. Fischer, C. Geibel, R. Köhler, R. Modler, C. Schank, F. Steglich, G. Weber, T. Komatsubara and N. Sato, *Phys. Rev. B*, **46**, 9, 5818 (1992).

N. Grewe and F. Steglich, Heavy Fermions in Handbook on the Physics and Chemistry of Rare Earths, K. A. Gschneidner and L. Eyring Ed., Chap. 97 (1991).

A. Habenschuss, G.E. Ice, C.J. Sparks, R.A. Neiser, NIM, **A266**, 215 (1988).

J.P. Hannon, G.T. Trammell, M.Blume and D. Gibbs, Phys. Rev. Lett., **61**, 10, 1245 (1988); **62**, 2644 (E) (1989).

S.M. Hayden, L. Taillefer, C. Vettier and J. Flouquet, Phys. Rev. B, **46**, 13, 8675 (1992).

S. Heald, X-Ray Absorption, Principles, Applications and Techniques of EXAFS, SEXAFS, and XANES, Konigberger and Prins Ed., John Wiley, Chap.3 and 4 (1988).

E.D. Isaacs, D.B. McWhan, C. Peters, G.E. Ice, D.P. Siddons, J.B. Hastings, C. Vettier, O. Vogt, Phys. Rev. Lett., **62**, 14, 1671 (1989).

E.D. Isaacs, D.B. McWhan, R. N. Kleiman, D.J. Bishop, G.E. Ice, P. Zschack, B.D. Gaulin, T.E. Mason, J.D. Garrett, W.J.L. Buyers, Phys. Rev. Lett., **65**, 3185 (1990).

J.D. Jackson, Classical Electrodynamics, Second Edition, John Wiley (1975).

R.W. James, The Optical Principles of the Diffraction of X-rays, Bell and Sons (1962).

A. Kirfel et al, Acta Cryst., **A47**, 180 (1991); Acta Cryst., **A48**, 247 (1992); Acta Cryst., **A47**, 35 (1993).

H. Kita, A. Dönni, Y. Endoh, K. Kakurai, N. Sato and T. Komatsubara, J. Phys. Soc. Japan, **63**, 726 (1994).

R.N. Kleiman, D.J. Bishop, H.R. Ott, Z. Fisk, J.L. Smith, Phys. Rev. Lett., **64**, 16, 1975 (1990).

A. Krimmel, P. Fischer, B. Roessli, H. Maletta, C. Geibel, C. Schank, A. Grauel, A. Loidl, and F. Steglich, Z. Phys. B, **86**, 161 (1992).

A. Krimmel, A. Loidl, P. Fischer, B. Roessli, A. Dönni, H. Kita, N. Sato, Y. Endoh, T. Komatsubara, C. Geibel and F. Steglich, Solid State Comm., **87**, 9, 829 (1993).

G.H. Lander and G. Aeppli, J. Magn. Magn. Mater., **100**, 151 (1991).

D.J. Lam and A.T. Aldred, Magnetic Properties of Actinides Compounds in The Actinides: Electronic Structure and Related Properties, A.J. Freeman and J.B. Darby Ed., Materials Science Series Vol. 1, Academic Press, Chap.3 (1974).

S. Langridge, W. G. Stirling, G.H. Lander and J. Rebizant, Phys. Rev. B, **49**, 17, 12010 (1994) and Phys. Rev. B, **49**, 17, 12022 (1994).

B. Lebech and M. Nielsen, New Methods and Techniques in Neutron Diffraction. Report RCN-234, p. 466-486. Petten: Reactor Centrum Nederland (1975).

H. Lin, M.F. Collins, T.M. Holden and W. Wei, Phys. Rev.B, **45**, 22, 12873 (1992).

M. Loewenhaupt and K.H. Fischer, Valence-fluctuation and heavy-fermion 4f systems in Handbook on the Physics and Chemistry of Rare Earths, K. A. Gschneidner and L. Eyring Ed., Chap. **105** (1993).

S.W. Lovesey, Theory of Neutron Scattering from Condensed Matter, Vol. 1 and 2, Oxford Science Publications (1987).

P. Luger, Modern X-Ray Analysis on Single Crystals, Walter de Gruyter Ed. (1980).

J. Luo, G.T. Trammell and J.P. Hannon, Phys. Rev. Lett., **71**, 287 (1993).

T.E. Mason, B.D. Gaulin, J.D. Garrett, Z. Tun, W.J.L Buyers and E.D. Isaacs, Phys. Rev. Lett., **65**, 3189 (1990).

G. Materlik and V. Kostroun, Rev. Sci. Instrum., **51**, 86 (1980).

D.F. McMorrow, D.A. Jehan, R.A. Cowley, R.S. Eccleston and G.J. McIntyre, J. Phys. Condens. Matter, **4**, 8599 (1992).

D.B. McWhan, C. Vettier, E.D. Isaacs, G.E. Ice, D.P. Siddons, J.B. Hastings, C. Peters, O.Vogt, Phys. Rev. B, **42**, 10, 6007 (1990).

NSLS User's manual , National Synchrotron Light Source (Brookhaven Laboratory), X-17 documentation (1991).

L. Paolasini, J. A. Paixão, G. H. Lander, P. Burlet, N. Sato, and T. Komatsubara, Phys. Rev. B, **49**, 10, 7072 (1994).

J.C. Phillips and K.O. Hodgson, Single-crystal X-ray Diffraction in Synchrotron Radiation Research, Winick and Doniach Ed., Plenum Press (1980).

P.M. Platzman and N. Tzoar, Phys. Rev. B2, 3536 (1970).

L. Price and K. Sköld, Introduction to Neutron Scattering in Methods of Experimental Physics, K. Sköld and D.L.Price Ed., Academic Press, Vol. **23**, Part C (1986).

J. Rossat-Mignod, Magnetic Structures in Methods of Experimental Physics, K. Sköld and D.L.Price Ed., Academic Press, Vol. **23**, Part C (1987).

J. Röhler, J. Magn. Magn. Mat., **47&48**, 175 (1985).

A. Schröder, J.-G. Lussier, B.D. Gaulin, J.D. Garrett, W.J.L. Buyers, L. Rebelsky, S.M. Shapiro, Phys. Rev. Lett., **72**, 1, 136 (1993).

V.F. Sears, Neutron Scattering Lengths and Cross Sections in Methods of Experimental Physics, K. Sköld and D.L.Price Ed., Academic Press, Vol. **23**, Part A (1986).

F. Steglich, U. Ahlheim, A. Böhm, C.D. Bredl, R. Caspary, C. Geibel, A. Grauel, R. Helfrich, R. Köhler, M. Lang, A. Mehner, R. Modler, C. Schank, C. Wassilew, G. Weber, W. Assmus, N. Sato, and T. Komatsubara, *Z. Phys. C* 195, 379 (1991).

F. Steglich *et al.*, *Phys. Rev. Lett.*, **43**, 25, 1982 (1979).

J. Sticht and J. Kübler, *Z. Phys. B*, **87**, 299 (1992).

C.J. Sparks Jr., X-Ray Fluorescence Microprobe for Chemical Analysis in Synchrotron Radiation Research, Winick and Doniach Ed., Plenum Press (1980).

W.G. Stirling and K.A. McEwen, Magnetic Excitations in Methods of Experimental Physics, K. Sköld and D.L.Price Ed., Academic Press, Vol. 23, Part C (1987).

C.C. Tang, W.G. Stirling, G.H. Lander, D. Gibbs, W. Herzog, P. Carra, B.T. Thole, K. Matterberger, O. Vogt, *Phys. Rev. B*, **46**, 9, 5287 (1992).

D.H. Templeton and L.K. Templeton, *Acta Cryst.*, **A36**, 237 (1980).

L. Tröger, D. Arvanitis, K. Basberschke, H. Michaelis, U. Grimm, E. Zschech, *Phys. Rev. B*, **46**, 6, 3283 (1992).

C. Vettier, *J. Magn. Magn. Mater.*, **129**, 59 (1994).

B.E. Warren, X-ray Diffraction, Dover Publications (1990).

Y. Wasedo, Novel applications of Anomalous (Resonance) X-Ray Scattering for structural Characterization of Disordered Materials, Chap.5, Springer Verlag (1984).

C.G. Windsor, Experimental techniques in Methods of Experimental Physics, K. Sköld and D.L.Price Ed., Academic Press, Vol. 23, Part A (1986).

H. Winick, Properties of Synchrotron Radiation and Synchrotron Radiation Sources, Research Facilities, and Instrumentation in Synchrotron Radiation Research, Winick and Doniach Ed., Plenum Press (1980).

W.H. Zachariasen, Theory of X-ray Diffraction of X-rays, G. Bell and Sons, London, Inc., New York (1945).

Published work

Related material to this thesis has been published in two articles:

A. Schröder, J.-G. Lussier, B.D. Gaulin, J.D. Garrett, W.J.L. Buyers, L. Rebelsky, S.M. Shapiro, Phys. Rev. Lett., **72**, 1, 136 (1993).

B.D. Gaulin, D. Gibbs, E.D. Isaacs, J.-G. Lussier, J.N. Reimers, A. Schröder, L. Taillefer, P. Zschack, Phys. Rev. Lett., **73**, 6, 890 (1994).

others are in preparation.

Incommensurate Magnetic Order in the Heavy Fermion Superconductor UNi₂Al₃A. Schröder,¹ J. G. Lussier,¹ B. D. Gaulin,¹ J. D. Garrett,¹ W. J. L. Buyers,² L. Rebersky,³ and S. M. Shapiro³¹Department of Physics and Astronomy, McMaster University, Hamilton, Ontario, Canada L8S 4M1²AECL Research, Chalk River Laboratories, Chalk River, Ontario, Canada K0J 1J0³Physics Department, Brookhaven National Laboratory, Upton, New York 11973

(Received 12 July 1993)

Neutron scattering measurements show UNi₂Al₃ to be unique among heavy fermion superconductors in that below $T_N \sim 5.2$ K it displays long range magnetic order which is incommensurate with its chemical lattice. The ordering wave vector is $(\frac{1}{3} \pm \delta, 0, \frac{1}{3})$ where $\delta = 0.110 \pm 0.003$. The measured superlattice intensities are well described by the presence of a longitudinal spin density wave within the hexagonal basal plane, polarized along a^* . The magnitude of the maximum ordered moment is found to be very small: $\mu_{\text{ord}} = (0.24 \pm 0.10) \mu_B$.

PACS numbers: 74.70.Tx, 61.12.Ex, 75.25.+z, 75.30.Mb

The interplay between magnetism and superconductivity is a central feature in the description of several classes of strongly correlated electron systems. The heavy fermion metals, a subset of which exhibits the apparent microscopic coexistence of f -electron magnetism and superconductivity at sufficiently low temperatures, form such a class of materials [1,2].

At present, there exist four such uranium-based compounds which display antiferromagnetic order characterized by small ordered moments. UPt₃ [3] forms a hexagonal-close-packed structure and orders magnetically below $T_N \sim 6$ K. It undergoes at least one and likely two superconducting transitions at $T_C \sim 0.5$ K [4]. URu₂Si₂ forms a body-centered-tetragonal crystal structure and undergoes magnetic and superconducting transitions at 17 and ~ 1.2 K, respectively [5]. A remarkable feature of the magnetism in these two compounds is that the magnitude of the ordered moment is extremely small ($\mu_{\text{ord}} \sim 0.02 \mu_B$ for UPt₃ [3], and $\mu_{\text{ord}} \sim 0.04 \mu_B$ for URu₂Si₂ [6]) leading to speculation that these materials in fact display nontrivial ordering phenomena [7] distinct from simple antiferromagnetic ordering of the local magnetic dipoles.

Recently, two new heavy fermion metals which display coexistence of superconductivity and antiferromagnetic order have been discovered. These are the simple hexagonal ternary metals UPd₂Al₃ [8] and UNi₂Al₃ [9] which undergo magnetic phase transitions at $T_N \sim 15$ and ~ 5 K, and superconducting transitions at $T_C \sim 2$ and ~ 1 K, respectively. Considerably less is known about these new compounds, compared with the extensive literature which exists on UPt₃ and URu₂Si₂. Neutron powder diffraction measurements indicate that UPd₂Al₃ [10] orders into a simple, $Q = (0, 0, \frac{1}{3})$, antiferromagnetic structure in which the moments lie ferromagnetically aligned within the basal plane, and the moment direction rotates by π from one basal plane to the next. Recent measurements [11,12] suggest a more complicated magnetic phase diagram. However, all measurements are consistent with an ordered magnetic moment of almost conventional size.

 $\mu_{\text{ord}} \sim 0.85 \mu_B$.

In this Letter we report on the first observation of magnetic neutron scattering from UNi₂Al₃ and determine the magnetic structure below T_N . As we will discuss, the magnetic order is characterized by a very weak ordered moment and an incommensurate ordering wave vector. This combination made these experiments very difficult. They required detailed, systematic searches through reciprocal space, as well as the sensitivity that is made possible by the use of diffraction from single crystal samples. Earlier neutron diffraction measurements [10] performed on powder samples of UNi₂Al₃ detected no evidence of magnetic order and placed an upper limit on the size of a possible magnetic moment of $0.2 \mu_B$. Previous muon spin rotation (μ SR) [13] experiments on UNi₂Al₃ provided evidence for antiferromagnetism with an ordered magnetic moment of the order of $0.1 \mu_B$. More recently [14] it has been noted that the zero field μ SR signal from the organic, spin density wave system (TMTSF)₂PF₆ is similar to that from UNi₂Al₃, suggesting the possibility of an incommensurate spin arrangement in UNi₂Al₃. These new measurements [14] were performed on a crystal cut from the same boule as the crystal which is the subject of the present work.

The UNi₂Al₃ single crystal used in the experiments described here was grown by the Czochralski technique in a tri-arc furnace. The starting materials were of high purity: the same ultrahigh purity uranium used in previous studies of URu₂Si₂ [15], 99.9999% aluminum, and 99.999% nickel. Other details of the growth were similar to those reported previously for uranium intermetallic crystal growth [15]. The crystal was subsequently annealed under argon at 900°C for one week. Part of this melt was crushed in order to produce a powder for neutron diffraction and susceptibility characterization, while a cylindrical sample of approximate dimensions 6 mm diameter by 25 mm long was extracted and used for the single crystal neutron measurements. The UNi₂Al₃ crystal, belonging to the hexagonal space group $P6/mmm$, displayed lattice parameters at 4.2 K of $a = 5.204$ Å and

$c=4.018$ Å, similar to those reported previously [9]. It was comprised of three closely aligned grains, characterized by a mosaic spread of $\sim 1^\circ$.

The powder neutron diffraction measurements were carried out on the C2 High Resolution Powder Diffractometer at Chalk River Laboratories. The powder was set in a vanadium can in the presence of a helium exchange gas and mounted in a pumped ^4He cryostat. Measurements taken at temperatures as low as 1.5 K showed no indication of the development of any scattering which could not be assigned a temperature-independent nuclear origin. There was no evidence of additional impurity phases found in this powder sample. Susceptibility measurements made on the powder sample showed behavior very similar to that reported previously [9]; a broad peak near ~ 90 K, a sharp peak near ~ 5 K, with a broad minimum between them at ~ 35 K.

More sensitive single crystal neutron measurements were carried out on the E3 triple axis spectrometer at the Chalk River Laboratories. This sample was mounted in a pumped ^4He cryostat with a helium exchange gas present. Its temperature could be varied from room temperature to ~ 1.5 K. The integrated intensities of several weak nuclear Bragg peaks were determined in order to compare to calculated intensities for pure UNi_2Al_3 as a measure of the quality of the single crystal. This comparison is good, and all indications are that the quality of this UNi_2Al_3 sample is very good.

The search for magnetic Bragg scattering as well as measurements of nuclear Bragg peaks for the purpose of magnetic intensity calibration were done with a variety of spectrometer configurations. All measurements were performed with the triple axis spectrometer set for elastic scattering, with a Si(111) monochromator and a pyrolytic graphite (002) analyzer. Data were collected at neutron energies of 8.23 and 3.52 THz with a pyrolytic graphite filter in the scattered beam, and at 4.12 THz without filters. We investigated three high symmetry planes in the single crystal: (h, h, l) , $(h, k, 0)$, and $(h, 0, l)$.

Our observations of magnetic neutron scattering from UNi_2Al_3 are shown in Fig. 1. Figure 1(a) shows portions of a scan along the $(h, 0, \frac{1}{2})$ direction at 20 K (open circles), and then at low temperature, 1.8 K (solid circles), both performed with 3.52 THz neutrons. These panels show clear magnetic Bragg peaks arising at $h=0.39$ and $h=0.61$ at low temperature. The intensity of these magnetic Bragg peaks is very low, down by 3 orders of magnitude from the intensity of a typical nuclear Bragg peak such as $(1, 0, 0)$. The width of the magnetic Bragg peaks is that determined by the resolution of the instrument, and the asymmetric shape of some of the peaks is due to the mosaic of our crystal. The magnetic order displayed by UNi_2Al_3 appears to be true long range order, with correlation lengths exceeding 400 Å, in contrast to that reported in both UPt_3 [3] and URu_2Si_2 [15].

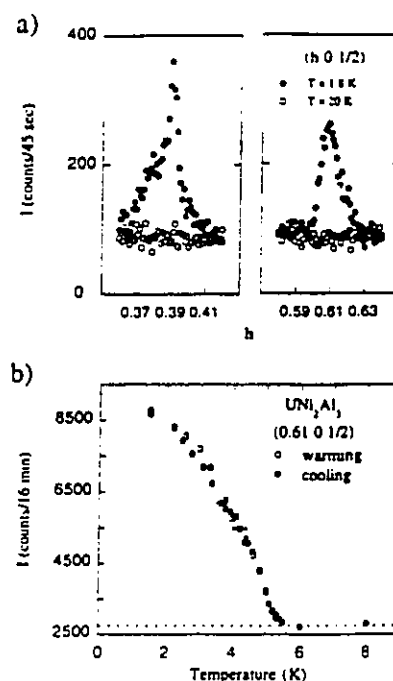


FIG. 1. (a) Sections of an $(h, 0, \frac{1}{2})$ scan performed with 3.52 THz neutrons at temperatures above (○) and below (●) $T_N \sim 5.2$ K are shown. The asymmetry in the line shape is due to sample mosaic. (b) The intensity of the $Q = (0.61, 0, \frac{1}{2})$ magnetic Bragg peak is shown as a function of temperature. The dashed line indicates the background scattering level.

The wave vector characterizing this magnetic structure is $Q = (\frac{1}{2} \pm \delta, 0, \frac{1}{2})$, with $\delta = 0.110 \pm 0.003$. The component of this wave vector within the basal plane is incommensurate, $q_{1C} = \frac{1}{2} \pm \delta$. It can be approximated as $q_{1C} = \frac{1}{2} \pm \frac{1}{4}$, but there is certainly no simple relationship between it and the periodicity of the nuclear lattice. The magnetic structure along the c direction corresponds to a simple antiferromagnetic stacking of the basal plane structure, as in UPd_2Al_3 . No additional superlattice Bragg peaks appeared at low temperature in any of the three scattering planes we examined. These planes were carefully examined with both two-dimensional, grid scans, and finer line scans along special high symmetry directions.

Longitudinal scans of the superlattice Bragg peak position $(0.61, 0, \frac{1}{2})$ were performed for several temperatures in the range from 2.5 to 6 K. These scans are reasonably described by Gaussian line shapes with temperature-independent peak position and widths. Additional transverse scans of the position of the maxima confirm that the incommensurability is temperature independent to within the tolerance of the measurement, $\Delta\delta = 0.003$. The intensity at this position, and also at $Q = (0.61, 0, \frac{1}{2})$, was

monitored in both warming and cooling runs, over the range $\sim 1.5 \text{ K} < T < 12 \text{ K}$, for the purpose of extracting the intensity of the superlattice Bragg peak as a function of temperature. This is shown in Fig. 1(b) for the $(0.61, 0, \frac{1}{2})$ peak. The temperature dependence of the $Q = (0.61, 0, \frac{1}{2})$ superlattice intensity was identical with that at $Q = (0.61, 0, \frac{1}{2})$ to within the precision of the measurement. The onset of the superlattice peak intensity is at $\sim 5 \text{ K}$, which corresponds well to the position of bulk anomalies associated with the magnetic phase transition in this compound [9]. As will be discussed, the wave-vector dependence of the intensity of equivalent superlattice peaks is consistent with that expected from magnetic ordering.

The magnetic superlattice intensity decreases monotonically with increasing temperature. However, it does not display the simple linear temperature dependence seen in UPt_3 [3] and URu_2Si_2 [15]. The intensity, shown in Fig. 1(b), can be described by $I \sim (T_N - T)^{0.6}$ down to 2 K , with $T_N = 5.2 \text{ K}$. To within the sensitivity of these measurements, there is no hysteresis near T_N , consistent with a second order phase transition. Also, it can be seen there is no saturation in the intensity for temperatures as low as 1.5 K . Clearly, it is of interest to extend these measurements to lower temperatures, into the superconducting state.

Therefore UNi_2Al_3 is the first heavy fermion superconductor to display incommensurate magnetic order. Examples of incommensurate magnetic ordering and fluctuations are known in other superconducting materials such as the Chevrel-phase superconductors, exemplified by HoMo_6S_8 [16], as well as in the high temperature superconductors [17]. However, there are important differences in each case. The moments in the Chevrel-phase superconductors arise from well-localized $4f$ electrons which interact only weakly with the conduction electrons. Incommensurate fluctuations have been observed in some high temperature superconductors [17], but there is no indication of long range order. The prototypical itinerant, incommensurate spin density wave system is chromium [18]. It is worthwhile to note that, in chromium, both the incommensurability as well as T_N are very sensitive to small levels of impurities. To the extent that this comparison is relevant, we may expect similar sample and impurity dependencies in UNi_2Al_3 .

At low temperature, measurements were made in the $(h, 0, l)$ plane at several magnetic Bragg peak positions as well as at several relatively weak nuclear positions in order to determine the magnetic structure and to estimate the size of the ordered moment. Comparison of the measured intensities of the magnetic peaks (Fig. 2) shows a strong angular dependence within the $(h, 0, l)$ plane that cannot be properly accounted for by a dependence on the form factor, $f(Q)$, alone. Figure 2 displays radial scans through three magnetic Bragg peak positions: $(0.39, 0, \frac{1}{2})$, with $|Q| = 0.95 \text{ \AA}^{-1}$, $(0.39, 0, \frac{1}{2})$, with $|Q| = 2.41$

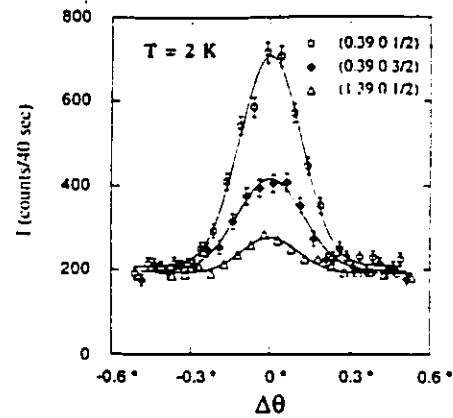


FIG. 2. Radial scans (plotted vs sample angle) of three magnetic Bragg peaks at $T = 2 \text{ K}$ are shown. These are $Q = (0.39, 0, \frac{1}{2})$, $|Q| = 0.95 \text{ \AA}^{-1}$, $\alpha = 34.8^\circ$; $Q = (0.39, 0, \frac{3}{2})$, $|Q| = 2.41 \text{ \AA}^{-1}$, $\alpha = 13.0^\circ$; and $Q = (1.39, 0, \frac{1}{2})$, $|Q| = 2.09 \text{ \AA}^{-1}$, $\alpha = 68.0^\circ$. α refers to the angle between Q and the c^* axis.

\AA^{-1} , and $(1.39, 0, \frac{1}{2})$, with $|Q| = 2.09 \text{ \AA}^{-1}$. As can be seen most clearly by comparing the intensity at the latter two ordering wave vectors, for which $|Q|$ is very similar, the intensity correlates strongly with the angle between Q and the c^* axis, with stronger intensities when Q tends to be along c^* . The neutron scattering cross section is sensitive to the component of moment which lies in a plane perpendicular to the scattering wave vector. It preferentially senses moments along a^* as Q tends towards the c^* direction. These results provide strong evidence, therefore, for the magnetic moment direction being predominantly along a^* .

We have modeled the integrated intensities of the magnetic Bragg peaks according to

$$I(Q) = \frac{F(Q)^2}{\sin(2\theta)} \sin^2(\nu) f^2(Q),$$

where $F(Q)$ is the structure amplitude for the Bragg peak, ν is the angle between Q and the moment direction, and $f^2(Q)$ is the magnetic form factor. Both $F(Q)$ and ν depend on the model for the ordered magnetic structure. The magnetic form factor $f^2(Q)$ was described by a form which had previously been used to account for magnetic properties in several uranium based compounds [19].

The intensities of six magnetic Bragg peaks, corrected for the Lorentz, $[\sin(2\theta)]^{-1}$, factor and magnetic form factor are shown in Fig. 3 as a function of the angle between Q and the c^* direction, α . As previously discussed, all Bragg peaks decrease in intensity with increasing α . We can specifically exclude models in which the moment is predominantly aligned along c^* , as had been previously suggested [13].

Several simple models for the magnetic structure were examined as candidates to describe our results. The one

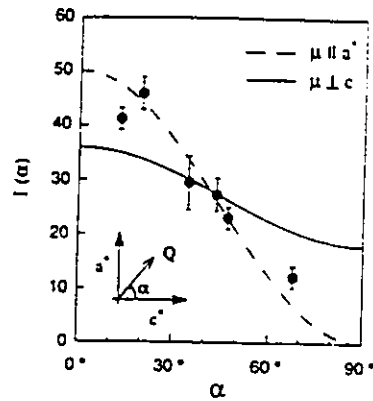


FIG. 3. Corrected (see text) intensity of six magnetic Bragg peaks is plotted vs α , the angle between Q and the c^* axis. The lines are predictions from models for the incommensurate magnetic order with differing polarizations within the basal plane. Shown are predictions for a longitudinal spin density wave structure within the basal plane, in which $\mu \parallel a^*$, and also for a planar modulation of the moments perpendicular to c .

which best describes these measurements is that of a longitudinal spin density wave (LSDW) within the hexagonal basal plane, in which the moments are parallel to a^* . The full, three dimensional magnetic structure is then formed by a simple antiferromagnetic stacking of this basal plane structure along c . The α dependence predicted by this model is shown as the broken line in Fig. 3. This figure compares the observed magnetic intensities corrected for all dependencies other than that on α , with that calculated for two model magnetic structures. A structure in which the moment direction is modulated within the basal plane produces a less-pronounced α dependence, as is shown by the solid line in Fig. 3.

As can be seen in Fig. 3, the LSDW polarized along a^* provides a very good description of our results. Models in which the moments are polarized along a different basal plane direction, and therefore not longitudinally polarized to the incommensurate component of the ordering wave vector, display less pronounced α dependencies. The key to understanding these dependencies is the fact that measurements at a single ordering wave vector probe only a single domain of any such single- q structure. However, assuming that all possible domains of such structures are equally populated, it is very difficult to distinguish such single- q LSDW structures from multiple- q modulated magnetic structures, as is known, for example, to describe the magnetic structure of neodymium [20].

Comparison of the magnetic Bragg peak intensities to those of the weaker nuclear Bragg peaks allows us to estimate the size of the ordered moment. The weak nuclear Bragg peaks are used in this comparison as they are less likely to be affected by extinction. However, as the role

of extinction in these peaks is not completely understood, our estimate of the ordered magnetic moment represents an upper limit. The size of the ordered moment determined from our data depends weakly on the model employed. The model corresponding to a single domain of the LSDW structure with $\mu \parallel a^*$, results in $\mu_{\text{ord}} = 0.14 \mu_B$. If, as is physically much more likely, the three possible domains are equally populated, we obtain $\mu_{\text{ord}} = 0.24 \mu_B$. Taken together with the uncertainty from the direct comparison to the nuclear peaks, these model calculations allow us to estimate the magnitude of the ordered moment at $\mu_{\text{ord}} = (0.24 \pm 0.10) \mu_B$. Within this LSDW structure, this ordered moment represents the maximum magnitude of the moment, which is modulated from site to site.

Three of us (A.S., J.G.L., and B.D.G.) gratefully acknowledge the hospitality of the Chalk River Laboratories and Brookhaven National Laboratory. This work was supported in part by the Natural Sciences and Engineering Research Council of Canada and the Ontario Centre for Materials Research. Work at Brookhaven National Laboratory was supported by the DMS of the U.S. DOE under Contract No. DEACO276CH00016. One of us (B.D.G.) acknowledges the support of the Alfred P. Sloan Foundation.

- [1] N. Grewe and F. Steglich, *Handbook on the Physics and Chemistry of Rare Earths*, Vol. 14, edited by K. A. Gschneider, Jr. and L. Eyring (Elsevier Science Publishers B. V., Amsterdam, 1991), Chap. 97, p. 343.
- [2] A. de Visser and J. J. M. Franse, *J. Magn. Magn. Mater.* **100**, 204 (1991).
- [3] G. Aeppli *et al.*, *Phys. Rev. Lett.* **60**, 615 (1988).
- [4] K. Hasselbach, L. Taillefer, and J. Flouquet, *Phys. Rev. Lett.* **63**, 93 (1989).
- [5] T. T. M. Palstra *et al.*, *Phys. Rev. Lett.* **55**, 2727 (1985).
- [6] C. Broholm *et al.*, *Phys. Rev. Lett.* **58**, 1467 (1987).
- [7] V. Barzykin and L. P. Gor'kov, *Phys. Rev. Lett.* **70**, 2479 (1993).
- [8] C. Geibel *et al.*, *Z. Phys. B* **84**, 1 (1991).
- [9] C. Geibel *et al.*, *Z. Phys. B* **83**, 305 (1991).
- [10] A. Krimmel *et al.*, *Z. Phys. B* **86**, 161 (1992).
- [11] A. Grauel *et al.*, *Phys. Rev. B* **46**, 5818 (1992).
- [12] B. D. Gaulin *et al.* (to be published).
- [13] A. Amato *et al.*, *Z. Phys. B* **86**, 159 (1992).
- [14] Y. J. Uemura and G. M. Luke, *Physica (Amsterdam)* **186-188B**, 223 (1993).
- [15] E. D. Isaacs *et al.*, *Phys. Rev. Lett.* **65**, 3185 (1990); T. E. Mason *et al.*, *ibid.* **65**, 3189 (1990).
- [16] J. W. Lynn *et al.*, *Phys. Rev. Lett.* **46**, 368 (1981); J. W. Lynn *et al.*, *Phys. Rev. B* **27**, 581 (1983).
- [17] T. E. Mason, G. Aeppli, and H. A. Mook, *Phys. Rev. Lett.* **68**, 1414 (1992).
- [18] E. Fawcett, *Rev. Mod. Phys.* **60**, 209 (1988).
- [19] G. H. Lander *et al.*, *Phys. Rev. B* **13**, 1177 (1976); K. M. Hughes, Ph.D. thesis, McMaster University, 1988.
- [20] P. Bak and B. Lebeck, *Phys. Rev. Lett.* **40**, 800 (1978).

Resonant Magnetic X-Ray Scattering Study of Phase Transitions in UPd_2Al_3 B. D. Gaulin,¹ D. Gibbs,² E. D. Isaacs,³ J. G. Lussier,¹ J. N. Reimers,^{1,*} A. Schröder,¹ L. Taillefer,^{4,†} and P. Zschack⁵¹Department of Physics and Astronomy, McMaster University, Hamilton, Ontario L8S 4M1, Canada²Physics Department, Brookhaven National Laboratory, Upton, New York 11973³AT&T Bell Laboratories, Murray Hill, New Jersey 07973⁴Laboratoire Louis-Neél, Centre Nationale de la Recherche Scientifique, Grenoble, France⁵Oak Ridge Institute for Science and Education, Brookhaven National Laboratory, Upton, New York 11973

(Received 22 November 1993; revised manuscript received 20 May 1994)

Resonant magnetic x-ray scattering measurements were performed on a single microcrystallite at the surface of a polycrystalline boule of the antiferromagnetic, heavy fermion superconductor UPd_2Al_3 . These measurements show a strong anomaly in the order parameter at 11.8 K, below $T_N \sim 14.5$ K, indicating at least two antiferromagnetically ordered phases which share a common periodicity. Measurements performed near and below $T_c = 2.0$ K show the antiferromagnetic order parameter to be unaffected on passing into the superconducting phase, to $\pm 2\%$.

PACS numbers: 74.70.Tx, 74.25.Ha

The fascinating low temperature transport, thermal, and magnetic properties displayed by heavy fermion materials have kept them at the forefront of metals physics research for more than a decade [1]. The interesting physics in the problem is believed to arise from the interplay between the relatively localized f electrons of these predominantly uranium and cerium based materials, and their metallic band states. Many properties can be described by the presence of a very large density of quasi-particle states at the Fermi level, hence large effective electron masses and their name; however, a full understanding remains elusive.

The electronic ground state of these materials is varied. The magnetic phenomena which they display ranges from long-range antiferromagnetic order with static moments of differing sizes to fluctuating short-range magnetic correlations. The most interesting phenomena which a subset of these materials display is the apparent microscopic coexistence of antiferromagnetic order and superconductivity at low temperatures. There are now four known compounds which display this extremely interesting ground state: UPt_3 [2], URu_2Si_2 [3], UPd_2Al_3 [4], and UNi_2Al_3 [5]. Of these UPd_2Al_3 and UNi_2Al_3 were discovered only recently, and their magnetic properties are not well established. However, the antiferromagnetism exhibited by UPt_3 [6] and URu_2Si_2 [7,8] is known to be highly unusual. The ordered moments present at saturation are extremely small ($\sim 0.02\mu_B$ for UPt_3 and $\sim 0.04\mu_B$ for URu_2Si_2), while the temperature dependence of the magnetic Bragg peak intensity is linear, consistent with mean field behavior, over an anomalously wide temperature regime. Also, in the UPt_3 and URu_2Si_2 crystals studied to date, the magnetic Bragg peaks are not resolution limited [6,8], indicating finite, antiferromagnetically ordered regions below T_N .

The magnetic properties of the two new heavy fermion superconductors (HFS) are currently the subject of intense study. Both of these new materials exhibit simple hexagonal crystal structures. Preliminary neutron mea-

surements on UPd_2Al_3 [9] indicated that it orders in an incommensurate magnetic structure below ~ 21 K, and then transforms to a simple antiferromagnetic structure below ~ 15 K with a low temperature ordered moment of $\sim 0.05\mu_B$, which is huge by the standards of the other superconducting heavy fermions. It is superconducting below ~ 2 K, which is the highest T_c displayed by this group of HFS. Very recently, a neutron scattering study using single crystals has reported [10] a remarkable 10% dip in the integrated intensity of the $(0,0,\frac{1}{2})$ superlattice Bragg peak near $T_c \sim 2$ K. This anomalous behavior is reported to be accompanied by an increase in the width of the Bragg peak. If correct, these results [10] would indicate an extremely strong coupling between the antiferromagnetic and superconducting order parameters in UPd_2Al_3 , much more pronounced than any such possible effects in either UPt_3 [6,11] or URu_2Si_2 [12].

More recent susceptibility, resistivity, and magnetostriiction measurements [13] show indications that the magnetic behavior of this compound is complicated. Anisotropy between basal-plane and c -axis susceptibility indicates that the magnetic moments in this compound lie within the basal plane. This study showed three magnetically ordered states present on application of a basal-plane magnetic field, while only one is present on application of a field along the c direction. No evidence of the incommensurate phase above ~ 15 K is reported. In addition, a new study has reported evidence of substantial magnetic anisotropy within the basal plane [14].

We have carried out a resonant magnetic x-ray scattering study of a single crystal sample of UPd_2Al_3 . This technique [15] involves tuning the energy of the incident x-ray beam through an appropriate absorption edge of the magnetic atom. In this case, the M_{IV} edge of uranium. For elastic scattering, a core electron is promoted to a partially filled magnetic level, where it exists briefly in an excitonlike state, before falling back to its original level, with the emission of a photon of the same energy. The M_{IV} edge corresponds to a $3d_{5/2}$ to $5f_{5/2}$ transition.

Both the excitation of the core electron and its subsequent decay occur via strong electron-dipole transitions. The process [16] is sensitive to the local magnetization by virtue of the Pauli principle and polarization selection rules. Very large enhancements [17] of the magnetic scattering cross section have previously been observed in a growing list [18] of lanthanide and actinide based magnets. This process must occur coherently over the resolution volume, and thus the scattering satisfies the Bragg condition for the antiferromagnetic state under study.

A remarkable feature of the present work is that it was actually carried out on a polycrystalline ingot sample. This ingot was roughly cylindrical in shape, with a length of ~ 20 mm, and a diameter of ~ 5 mm. However, several single crystal grains of area ~ 1 mm² were clearly visible on its surface. The faces of these grains were found to be perpendicular to the *c* axis. They did not propagate very far into the ingot, as they could not be identified optically on examination of a broken surface. We estimate that the grains were well below 1 mm in thickness, and likely not thicker than a few microns. These single crystal measurements were therefore performed on a sample which was too small for single crystal neutron diffraction work, by a factor of between 2 and 4 orders of magnitude in volume.

The sample was prepared at the Laboratoire Louis-Néel (CNRS) in Grenoble, France. High-purity starting materials, U, Pd, and Al, were melted together in stoichiometric amounts, using RF induction and a water-cooled crucible in an ultrahigh vacuum. The boule was quenched shortly after being homogeneously molten in order to minimize evaporation. The resulting polycrystalline ingot was annealed for 3 d at 900°C in ultrahigh vacuum. A small piece of the annealed ingot was used for characterization, yielding a residual resistivity $\rho_0 = 2.2$ $\mu\Omega$ cm, and a superconducting transition temperature at $T_c = 2.0$ K with a width of 0.04 K. X-ray powder diffraction measurements show no phase other than the PrNi₂Al₃ structure. The residual resistivity, the superconducting T_c , as well as the width in T_c are often taken as figures of merit to describe the crystalline quality of HFS materials. The results from the sample under study here show this material to be of very high quality. In particular, the residual resistivity of this sample is lower than that displayed by other HFS samples, with the exception of the best UPt₃ samples [19].

Our x-ray measurements were performed on beam lines X22C and X14 at the National Synchrotron Light Source of Brookhaven National Laboratory. We first discuss the measurements at X22C. The sample was mounted inside a beryllium can with a helium exchange gas present. This sample can was then attached to the cold finger of a two-stage closed cycle refrigerator which allowed us to change the sample temperature continuously from 4 to 300 K. The temperature was stable to 0.01 K over the temperature range of interest in this Letter ($T \leq 30$ K).

The energy dependence of the integrated intensity due

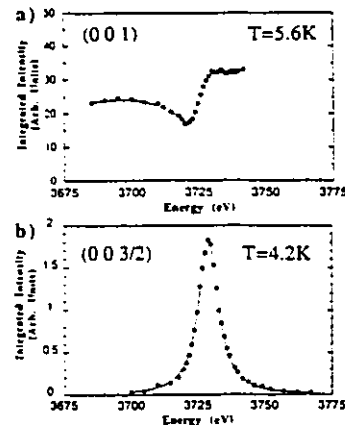


FIG. 1. The energy dependence of the (0,0,1) Bragg peak due to charge scattering in UPd₂Al₃ is shown in panel (a) at 5.6 K. Panel (b) shows the energy dependence of the (0,0, $\frac{3}{2}$) Bragg peak at 4.2 K. This scattering is clearly distinct from that shown in panel (a) and is identified as being magnetic in origin. Solid lines are drawn only to guide the eye.

to charge scattering at (0,0,1) and of that due to magnetic scattering at (0,0, $\frac{3}{2}$) are shown in Fig. 1 for temperatures well below $T_N \sim 14.5$ K. The scattering at (0,0, $\frac{3}{2}$) is well described by a Lorentzian centered at the M_{IV} edge energy, 3.728 keV, and is clearly distinct from the line shape of the (0,0,1) charge Bragg peak, which is typical of anomalous charge scattering near an absorption edge [20]. This energy dependence identifies the (0,0, $\frac{3}{2}$) Bragg peak as being magnetic in origin [18]. A similar energy dependence is observed at (0,0, $\frac{1}{2}$).

Figure 2 shows the wave-vector dependence of magnetic scattering at (0,0, $\frac{3}{2}$), as well as that for the charge scattering at (0,0,1). These data were taken at several temperatures below $T_N \sim 14.5$ K. The results of longitudinal scans are shown. Transverse scans were also performed at these wave vectors, but are not displayed. The full width of the scattering in the transverse direction (θ) at the (0,0, $\frac{3}{2}$) position was $\sim 0.1^\circ$, demonstrating the single crystal nature of the grain under study. The inset of this figure shows the longitudinal scans at (0,0,1) and (0,0, $\frac{3}{2}$), scaled so that their peak intensities coincide. Clearly the magnetic peak at (0,0, $\frac{3}{2}$) is comparable in width to the charge scattering peak at (0,0,1). This measurement demonstrates the long magnetic correlation length within the antiferromagnetic state. Resolution considerations show that this is ~ 1500 Å. Very interestingly, this result contrasts a similar comparison of x-ray magnetic to charge scattering from URu₂Si₂ [8], in which a magnetic Bragg peak at larger wave vector was seen to be broader than a corresponding charge peak. In the case of URu₂Si₂ [8], this indicated finite magnetic domains with a temperature-independent extent of ~ 450 Å along its body-centered tetragonal *c* direction. The new results on UPd₂Al₃ also contrast with neutron scattering measurements on UPt₃ [6], which show that the antifer-

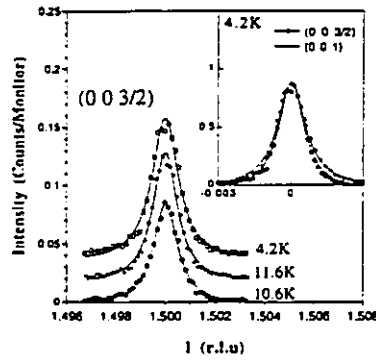


FIG. 2. Longitudinal scans along the (001) direction through $(0,0,\frac{3}{2})$ are shown for UPd_2Al_3 with the incident x-ray energy tuned to the M_{IV} edge (3.728 keV) at different temperatures below $T_N \sim 14.5$ K. The data have been offset in the vertical direction, for clarity. The inset shows the $(0,0,1)$ charge peak and the $(0,0,\frac{3}{2})$ magnetic peak scaled to agree in peak intensity. All the solid lines in the figure are phenomenological fits to the data intended as guides to the eye. The magnetic Bragg peaks in UPd_2Al_3 show no anomalous width in wave vector, in contrast to other antiferromagnetic heavy fermion superconductors.

romagnetic ordered state, which it enters below ~ 5 K, is characterized by a temperature independent correlation length of ~ 250 Å.

The temperature dependence of the $(0,0,\frac{1}{2})$ and $(0,0,\frac{3}{2})$ magnetic Bragg peaks is shown for both warming and cooling in Fig. 3(a). The principal features of these curves reproduce for different sample histories from the same grain. The form of these curves is quite remarkable. The temperature dependence of the Bragg peaks displays a sharp onset at $T_N \sim 14.5$ K. At lower temperatures there is a large anomaly centered near $T_{N1} \sim 11.8$ K. This is evidence for the presence of at least two magnetically ordered phases below T_N , which exhibit a common periodicity as they share the same Bragg reflections. The transition at $T_N \sim 14.5$ K appears continuous as there is no evidence for hysteresis. The large anomaly at T_{N1} displays weak hysteresis, suggesting a discontinuous transition between two magnetically ordered phases.

Several such grains on the surface of the polycrystalline boule were investigated. The c axis of all of these grains were normal to the surface, but the basal-phase orientation was random. In all cases the order parameter turned on sharply with the same $T_N \sim 14.5$ K, and all grains displayed the same c -axis lattice parameter, to within the resolution of the instrument. However, the relative magnitude of the strong anomaly at T_{N1} , compared with the low temperature Bragg intensity, was variable.

The form of the amplitude for coherent elastic x-ray scattering within the dipole approximation [16] produces a magnetic polarization sensitivity very different from that obtained in magnetic neutron scattering [21], in which one is sensitive to the components of moment in

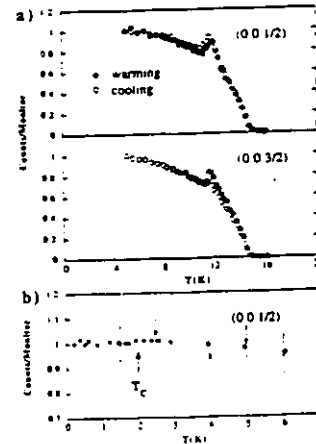


FIG. 3. (a) The temperature dependence of the resonant magnetic x-ray scattering at the $(0,0,\frac{3}{2})$ and the $(0,0,\frac{1}{2})$ Bragg peak positions in UPd_2Al_3 are shown for both warming and cooling runs. A large anomaly is present in these order parameter curves at $T_{N1} \sim 11.8$ K. (b) The temperature dependence of the resonant magnetic x-ray scattering (solid squares) at relatively low temperatures for the $(0,0,\frac{1}{2})$ Bragg peak in UPd_2Al_3 is shown, along with the same quantity measured by powder neutron diffraction (open squares). The intensity of the neutron data have been scaled to agree with the x-ray measurement at low temperature.

a plane perpendicular to Q . For the conditions relevant to the present measurements, the magnetic x-ray scattering cross section is proportional to the projection of the moment onto the scattered x-ray wave vector. Consequently, the strong anomaly at T_{N1} observed in the resonant x-ray measurement is consistent with at least one phase transition characterized by a spin reorientation within the basal plane.

We also carried out a set of resonant magnetic x-ray measurements on the X14 beam line with the same UPd_2Al_3 sample in a dilution refrigerator which allowed us to access temperatures as low as 225 mK, well below the superconducting phase transition near 2 K. These measurements were carried out under conditions similar to those described for X22C. The sample was mounted in Cu-impregnated low temperature grease and sat on the cold finger in vacuum. The surface of the ingot sat just above the grease allowing restricted access to the $(0,0,\frac{1}{2})$ magnetic Bragg peak only.

The temperature dependence of the magnetic scattering at $(0,0,\frac{1}{2})$ as measured at X14 at low temperatures is shown in Fig. 3(b). As in the measurement at X22C described above, the intensity has an onset near 15 K. The measurements extend down to 225 mK and we can see that the resonant magnetic scattering intensity is temperature independent on passing through the superconducting transition near 2 K, at least to the accuracy of

the measurement, $\pm 2\%$. This clearly contradicts the recent report of a strong coupling between the antiferromagnetic and superconducting order parameters near T_c [10]. Also, recent heat capacity measurements have observed evidence of an additional phase transition at 600 mK in a sample of $\text{UPd}_2\text{Al}_{3.03}$ [22]. We see no evidence for such a transition in our measurements, to within the accuracy quoted above.

Powder neutron diffraction measurements were performed on a sample taken from the same boule as that used in the x-ray study. These data were collected on the E3 triple axis spectrometer at the Chalk River Laboratories. The intensities of the $(0, 0, \frac{1}{2})$ and $(1, 0, \frac{1}{2})$ reflections were studied as a function of temperature. The position of the $(0, 0, \frac{3}{2})$ reflection closely coincided with a reflection of nuclear origin, and was thus obscured. The powder neutron scattering results were qualitatively similar at these two wave vectors, and the temperature dependence of the neutron scattering from the powder at $(0, 0, \frac{1}{2})$ is also displayed in Fig. 3(b). It is clear from Fig. 3(b) that the qualitative behavior of the powder neutron scattering at low temperatures is very similar to the resonant x-ray scattering at $(0, 0, \frac{1}{2})$. The powder neutron scattering at $(0, 0, \frac{1}{2})$ shows no anomaly near $T_{N1} \sim 11.5$ K, consistent with previous results [9,10].

A systematic search for additional magnetic Bragg scattering along the $(0, 0, l)$ direction was carried out, with particular emphasis on the temperatures between 14 and 21 K. The purpose of these scans was to check for possible incommensurate magnetic structures above T_N , as previously suggested [9]. No such scattering was observed in either the resonant magnetic x-ray or powder neutron studies.

The present magnetic x-ray results show evidence for multiple antiferromagnetically ordered phases present in zero applied field. This is a different conclusion than that reached by a previous bulk study [13] in which three phases were only identified in the presence of a sizable (~ 0.4 T) magnetic field applied within the a - b plane. Our measurements imply that the magnitude of the anomalies in the bulk properties associated with these transitions become unmeasurably small in small applied fields or for fields applied along the c direction. In addition, this Letter demonstrates that magnetic single crystal diffraction measurements can be made on extremely small single crystal grains. These grains form from the melt very quickly at the surface of polycrystalline boules. Large single crystal growth often involves maintaining the constituents at least partially within the melt for long periods of time. Problems in stoichiometry may arise for such large crystals, as one constituent may evaporate preferentially. This is known to occur in several HFS materials: Si in URu_2Si_2 , and Al in both UNi_2Al_3 and UPd_2Al_3 . Consequently, studies of systems which are sensitive to low concentration of structural imperfections may well require small, high-purity samples of the type studied in this Letter.

We would like to thank Dr. Z. Tun for assistance during the powder neutron measurements and Dr. N. Sato for helpful discussions. This work was supported in part by the Natural Sciences and Engineering Research Council of Canada and by the Ontario Centre for Materials Research. Work at Brookhaven National Laboratory is supported by the U.S. DOE under Contract No. DE-AC02-76CH00016. Work at the Oak Ridge National Laboratory PRT beam line X14 at the NSLS was supported by the U.S. DOE under Contract No. DE-AC05-84OR21400 with Martin Marietta Energy Systems Inc. Two of us (B.D.G. and L.T.) acknowledge the support of the Alfred P. Sloan Foundation, while one of us (L.T.) acknowledges the support of the Canadian Institute for Advanced Research.

* Present address: Moli Energy (1990) Ltd., Maple Ridge, BC, Canada V2X 9E7.

† Present address: Physics Department, McGill University, Montreal, QC, Canada H3A 2T8.

- [1] For reviews of heavy fermion metals see A. de Visser and J. J. M. Franse, *J. Magn. Magn. Mater.* **100**, 204 (1991); N. Grewe and F. Steglich, in *Handbook on the Physics and Chemistry of Rare Earths*, edited by K. A. Gschneidner, Jr. and L. Eyring (Elsevier Science, New York, 1991), Vol. 14, Chap. 97, p. 343.
- [2] G. R. Stewart *et al.*, *Phys. Rev. Lett.* **52**, 679 (1984); K. Hasselbach, L. Taillefer, and J. Flouquet, *Phys. Rev. Lett.* **63**, 93 (1989).
- [3] T. T. M. Palstra *et al.*, *Phys. Rev. Lett.* **55**, 2727 (1985).
- [4] C. Geibel *et al.*, *Z. Phys. B* **84**, 1 (1991).
- [5] C. Geibel *et al.*, *Z. Phys. B* **83**, 305 (1991); A. Schröder *et al.*, *Phys. Rev. Lett.* **72**, 136 (1994).
- [6] G. Aeppli *et al.*, *Phys. Rev. Lett.* **60**, 615 (1988).
- [7] C. Broholm *et al.*, *Phys. Rev. Lett.* **58**, 1467 (1987); T. E. Mason *et al.*, *Phys. Rev. Lett.* **65**, 3189 (1990).
- [8] E. D. Isaacs *et al.*, *Phys. Rev. Lett.* **65**, 3185 (1990).
- [9] A. Krimmel *et al.*, *Z. Phys. B* **86**, 161 (1992).
- [10] A. Krimmel *et al.*, *Solid State Commun.* **87**, 829 (1993).
- [11] G. Aeppli *et al.*, *Phys. Rev. Lett.* **63**, 676 (1989).
- [12] W. Wei *et al.*, *J. Magn. Magn. Mater.* **108**, 77 (1992).
- [13] A. Grauel *et al.*, *Phys. Rev. B* **46**, 5818 (1992).
- [14] A. de Visser *et al.* (to be published).
- [15] D. Gibbs *et al.*, *Phys. Rev. Lett.* **61**, 1241 (1988); D. Gibbs *et al.*, *Phys. Rev. B* **43**, 5663 (1991).
- [16] J. P. Hannon *et al.*, *Phys. Rev. Lett.* **61**, 1245 (1988).
- [17] E. D. Isaacs *et al.*, *Phys. Rev. Lett.* **62**, 1671 (1989).
- [18] W. G. Stirling and G. H. Lander, *Synchr. Rad. News* **5**, No. 4, 17 (1992); D. Gibbs *ibid.* **5**, No. 5, 18 (1992).
- [19] L. Taillefer, F. Piquemal, and J. Flouquet, *Physica (Amsterdam)* **153-155C**, 451 (1988).
- [20] *X-Ray Resonant (Anomalous) Scattering*, edited by G. Materlik, C. Sparks, and K. Fischer (Elsevier, Amsterdam, 1994).
- [21] S. W. Lovesey, *Theory of Neutron Scattering from Condensed Matter* (Clarendon Press, Oxford, 1984), Vol. 2.
- [22] T. Sakon *et al.*, *Physica (Amsterdam)* **186-188B**, 297 (1993).